

Designing Ferroalloys for Niobium and Titanium Additions to Steel

by

Syed Jawad Ali Shah

A thesis submitted in partial fulfillment of the requirements for the degree of

Doctor of Philosophy

in

Materials Engineering

Department of Chemical and Materials Engineering  
University of Alberta

© Syed Jawad Ali Shah, 2015

## Abstract

The use of microalloyed steels have accelerated exponentially in the past few decades due to their better mechanical properties as compared to traditional carbon steel. One of the main factor that contribute to their high strength and toughness values is the presence of uniformly dispersed fine carbide, nitrides and/or carbonitride precipitates. Titanium, niobium and/or vanadium are usually added in form of their respective ferroalloys to form such precipitates. However, if the size of these precipitates is coarser then they adversely effects the mechanical properties. Presence of such coarse niobium- and/or titanium-rich particles have been reported extensively in literature. Very limited understanding is available on the source of these coarse particles in microalloyed steels. Two different school of thoughts exists: one contributing the existence of such particles to undissolved phases from their respective ferroalloys while other to precipitation at high temperatures as a result of segregation.

In order to understand and compare both ideologies, a need of extensive study of ferroalloys was required. In this thesis both ferroniobium and ferrotitanium are characterized in details in order to identify their phases, especially high melting temperature phases as compared to steelmaking temperature. Differential scanning calorimeter (DSC) is used to study different phase transformations during the course of solidification of ferroniobium alloy in order to better understand its phase evolution mechanism. For first school of thoughts: once the nature of high melting temperature phase(s) of ferroniobium is determined, different steel samples are studied and characterized to relate coarse niobium-rich particles to high melting temperature phase(s). For second school of thought: thermodynamic study of steel system is done both under equilibrium

and using Scheil solidification models, in order to check for precipitation at high temperature. Although current study supports second school of thought still ternary alloys are made to eliminate the high melting temperature phase(s) of ferroniobium alloy. This is done by addition of aluminum to as-received ferroniobium alloy followed by characterization and phase study. The whole study incorporates the use of different characterization tools including scanning electron microscopy (SEM), transmission electron microscopy (TEM), X-ray diffraction (XRD) and differential scanning calorimetry (DSC).

## Preface

Ferroalloys and steel samples used in carrying out the research were provided by Evraz Inc., along with their compositions. The composition of the ferroalloys was verified by Cambridge Scientific.

Chapter 4 of the thesis has been published as: S. J. Shah, H. Henein and D. G. Ivey. Microstructural characterization of ferrotitanium and ferroniobium. *Materials Characterization*, 2013, 78, 96-107.

It is my original work and I carried out data collection and its analysis. The manuscript was originally written by me and was modified and formatted by H. Henein and D. G. Ivey.

Chapter 5 of the thesis has been published as: S. J. A. Shah, H. Henein and D. G. Ivey. Microstructural evolution and characterization of a ferroniobium alloy. *Emerging Materials Research*, 2013, 2, EMR2, 79-89. It is my original work and I collected and analyzed all data. I wrote the manuscript, which was later modified and formatted by H. Henein and D. G. Ivey.

## **Dedication**

I would like to dedicate my work to:

My parents: Syed Fawad Ali Shah and Bushra Qureshi

My wife: Nuzhat Shaheen Butt

My daughters: Kainaat Ali Shah and Kiran Ali Shah

My brother and his family: Salman Ali Shah and Maha Niazi

My sister and her family: Khadijah Farid, Farid Akhtar, Mariyum, Maham and Mauz

**Lastly most importantly to my late friend: Bilal Saleem (RIP)**

## **Acknowledgements**

This research would not have been possible without the knowledge and guidance of my supervisors Professor Hani Henein and Professor Douglas Ivey. I would like to express my sincerest gratitude and thanks to both of them. It has been an excellent learning and personality grooming experience for me. I am thankful to Evraz Inc. and the University of Engineering and Technology, Lahore, for their financial support.

I would like to thank Dr. J. B. Wiskel and Dr. A. A. Bogno for their fruitful discussions on different scientific and technical aspects of the project. I would also like to thank Martin Kupsta for FIB sample preparation, Sergei Matveev for wave length dispersive spectroscopy, Shihong Xu for the Auger analysis performed and Dr. Arthur Mar's research group for Arc melting furnace facility. I am grateful to all my colleagues and friends for their support and help in all aspects of my PhD work.

I am deeply thankful to my parents, my brother and my sister, my loving daughters (Kainaat and Kiran) and my wife (Nuzhat) for all their prayers, patience and support. Their love and encouragement drove my passion and boosted my confidence in achieving my goal.

Lastly I am thankful to funding from Natural Sciences and Engineering Research Council (NSERC), EVRAZ North America, Alliance Pipelines, TransCanada Pipeline (TCPL), Enbridge and University of Engineering and Technology Lahore.

# Table of Contents

<b>Chapter 1: Introduction</b> .....	1
1.1. Statement of the Problem .....	1
1.2. Objectives and Methodology.....	3
1.3. Outline of Thesis .....	4
<b>Chapter 2: Literature Review</b> .....	6
2.1. Introduction .....	6
2.2. Microalloyed Steels .....	7
2.2.1. Solid Solution Strengthening .....	8
2.2.2. Grain Refinement .....	8
2.2.3. Work Hardening .....	9
2.2.4. Precipitation Strengthening .....	9
2.3. Presence of Coarse Niobium- and Titanium-Rich Particles in Microalloyed Steels (Problem Statement) .....	11
2.4. Ferroalloys .....	16
2.4.1. Production of Ferroniobium .....	17
2.4.2. Production of Ferrotitanium .....	18
2.4.3. Classification of Ferroalloys.....	19

2.4.4. Dissolution of Ferroalloys .....	21
2.4.4.1. Factors Effecting Dissolution Behavior .....	21
2.4.4.2. Temperature Dependence .....	21
2.4.4.3. Dissolution Time .....	22
2.4.4.3.1. Dissolution of Pure Niobium and Ferroniobium Alloy..	24
2.4.4.3. Dissolution Heat .....	26
2.4.5. Iron-Niobium System .....	27
2.4.6. Iron-Titanium System.....	29
2.4.7. Iron-Niobium-Aluminum System.....	32
2.5. Summary.....	34
2.6. References .....	35
<b>Chapter 3: Experimental Procedures .....</b>	<b>42</b>
3.1. Outline of Experimental Procedures.....	42
3.2. Composition Analysis.....	43
3.3. Scanning Electron Microscope (SEM).....	43
3.4. Transmission Electron Microscope (TEM).....	46
3.5. X-ray Diffraction (XRD).....	48
3.6. Differential Scanning Calorimetry (DSC).....	48

3.7. Induction Melting .....	49
3.8. Arc Melting.....	51
3.9. References .....	52
<b>Chapter 4: Microstructural Characterization of Ferrotitanium and Ferroniobium....</b>	<b>53</b>
4.1. Introduction .....	53
4.2. Experimental Section.....	54
4.3. Results and Discussion .....	55
4.3.1. Ferrotitanium (Iron-Titanium).....	56
4.3.2. Ferroniobium (Iron-Niobium) .....	68
4.4. Conclusions .....	79
4.5. References .....	80
<b>Chapter 5: Microstructural Evolution of a Commercial Grade Ferroniobium Alloy ..</b>	<b>84</b>
5.1. Introduction .....	84
5.2. Experimental Methods.....	85
5.3. Results .....	86
5.4. Discussion.....	94
5.5. Conclusions .....	106
5.6 References .....	107

<b>Chapter 6: Analysis of Coarse Niobium-Rich Particles in the Steel</b> .....	111
6.1. Introduction .....	111
6.2. Experimental Methods.....	112
6.3. Results and Discussion .....	114
6.3.1. Ferroniobium Addition to Steel A.....	114
6.3.2. Characterization of Steel B for Coarse Niobium-Rich Particle.....	118
6.3.3. Thermodynamic Calculations for Steel B .....	124
6.4. Conclusions .....	130
6.5. References .....	132
<b>Chapter 7: Ternary Alloys (Niobium-Aluminum-Iron)</b> .....	134
7.1. Introduction .....	134
7.2. Experimental Methods.....	135
7.3. Results and Discussion .....	136
7.3.1. Ternary Alloys (Induction Melting) .....	137
7.3.2. Ternary Alloys (Arc Melting).....	147
7.3.3. Effect of Aluminum Addition on the Liquidus Temperature .....	151
7.4. Conclusions .....	158
7.5. References .....	160

<b>Chapter 8: Conclusions and Future Recommendations</b> .....	162
8.1. Conclusions .....	162
8.2. Future Recommendations .....	163

## List of Tables

Table 4.1: Chemical analysis of ferrotitanium and ferroniobium .....	55
Table 4.2: EDX analysis of chemical composition (wt.%) of the regions labeled in Figure 4.3 .....	59
Table 4.3: Volume fractions for the regions identified in Figure 4.3 .....	60
Table 4.4: Crystallographic data for ferrotitanium phases .....	68
Table 4.5: Chemical composition of each region (wt.%) labeled in Fig. 4.10 .....	70
Table 4.6: Volume fractions of the regions labeled in Figure 4.10 .....	71
Table 4.7: Crystallographic data for ferroniobium phases .....	77
Table 5.1: Volume fractions of the regions labeled in Figure 5.1b - mean fraction (standard deviation) .....	87
Table 5.2: Onset temperatures of DSC peaks for ferroniobium alloy at different heating and cooling rates .....	91
Table 5.3: Volume fraction of eutectic microstructure at different temperatures .....	105
Table 6.1: Composition range of steels studied (provided by Evraz) .....	113
Table 6.2: Calculation of amount of carbon and niobium in liquid determined from Figure 6.13 .....	129

Table 7.1: Chemistry of various aluminum added ferroniobium samples prepared by induction melting.....	138
Table 7.2: Chemistry (wt.%) of various regions of ferroniobium samples with different amounts of aluminum (compositions determined through SEM-EDX analysis) .....	145
Table 7.3: Nature and volume fraction of different phases identified in table 7.2.....	146
Table 7.4: Solidification start temperature for niobium-iron-aluminum alloys with different aluminum compositions and different cooling rates.....	153

## List of Figures

Figure 2.1: Formation of loops by a dislocation around a hard and non-deformable precipitate. [Gla97] .....	11
Figure 2.2: Effect of niobium carbide on yield strength for various sizes of niobium carbide particles. [Dav01] .....	13
Figure 2.3: a) Niobium-rich phase in the exposed fracture surface of a hook crack; b) Niobium-rich phase on an exposed fractured tensile specimen; c) Titanium-rich phase in exposed fracture surface of a hook crack; d) Titanium-rich phase in the mid-section of product; e) coarse niobium-rich particles on exposed surface of the mid-thickness cracks of a specimen; f) Niobium-/Titanium-rich particles along the mid-thickness of a specimen.. [Abr06(2)].....	14
Figure 2.4: World demand for feroniobium and CBMM's sales and production capacity. [Sou01] .....	18
Figure 2.5: Melting and dissolution behavior of two types of ferroalloys .....	20
Figure 2.6: Predicted dissolution time for a) 65 wt.% ferroniobium; b) pure niobium spheres immersed in liquid steel baths at 1873 K (1600°C). (1: prediction for 100 % convection; 2: combined natural and forced convection and 3: 0.9 ms <sup>-1</sup> steel velocity past the sphere) (redrawn). [Arg82].....	25
Figure 2.7: Iron-Niobium binary phase diagram [Vob11] .....	29
Figure 2.8: Iron-titanium binary phase diagram [Mur81]. .....	30

Figure 2.9: Isothermal cross-section for the iron-aluminum-niobium ternary system at 1273 K (1000°C) [Bej93(2)]. .....	33
Figure 3.1: Steps involved in TEM sample preparation using a FIB: a) sectioned area of interest; b) FIB probe welded to the lamella which is then plucked out; c) sample placed on a copper grid for thinning; d) final prepared sample as imaged in the TEM. ....	46
Figure 3.2: An example of the measurement of R values from an SAD pattern.....	47
Figure 3.3: Schematic diagram showing the experimental setup for induction melting. ....	49
Figure 4.1: Iron-titanium binary phase diagram [Oka96]. The vertical line represents the ferrotitanium alloy composition (iron and titanium only). ....	56
Figure 4.2: XRD pattern for as-received ferrotitanium alloy.....	57
Figure 4.3: a) SEM BSE image of as-received commercial grade ferrotitanium alloy showing the overall microstructure. b) Higher magnification SEM BSE image of the area indicated in (a) showing five different contrast regions labelled 1-5.....	58
Figure 4.4: a) TEM BF image of regions 1 and 2 from Fig. 3b, b) and c) EDX spectra for the low energy range from regions 2 and 1, respectively.....	62
Figure 4.5: a) TEM BF image of regions 1, 2 and 4 from Fig. 3b. b) and c) SAD patterns from region 1, indexed as $Ti(C_xN_{1-x})$ . d) and e) SAD patterns from region 2, indexed as $\alpha$ -titanium.....	63
Figure 4.6: a) TEM BF image showing regions 3 and 4 from Figure 4.3b. b) and c) SAD patterns from regions 3 indexed to $\beta$ -titanium. d) and e) SAD patterns form region 4 indexed	

to titanium-iron-aluminum ternary intermetallic (magnified 1.5 times relative to SAD patterns in (b) and (c)) .....	65
Figure 4.7: a) TEM BF image of region 5 from Figure 4.3b. b) and c) SAD patterns from region 5. The patterns were indexed to FeTi. ....	67
Figure 4.8: Iron-niobium binary phase diagram [Oka93]. The vertical line represents the ferroniobium alloy composition (iron and niobium only). ....	69
Figure 4.9: XRD pattern for as-received ferroniobium alloy. ....	69
Figure 4.10: a) SEM BSE image of as-received commercial grade ferroniobium alloy showing overall microstructure. b) Higher magnification SEM BSE image of ferroniobium showing three different contrast regions labelled 1-3. ....	70
Figure 4.11: a) TEM BF image taken from region 1 of Figure 4.10. b) and c) SAD patterns taken from grains 1 and 2 (both region 1) and indexed to BCC niobium. ....	72
Figure 4.12: a) TEM BF image of region 2 and 3 from Figure 4.10. b) and c) SAD patterns taken from region 2 and 3, respectively and indexed to $\mu$ -Fe <sub>7</sub> Nb <sub>6</sub> . ....	73
Figure 4.13: a) TEM BF image of FIB sample after further thinning, b) Higher magnification TEM BF image of area indicated in (a) showing striation features in the $\mu$ phase when tilted. c) SAD pattern from intermetallic indexed to the $\mu$ phase showing streaking of diffraction spots perpendicular to striation features. ....	74
Figure 4.14: a) and b) TEM BF images showing the three regions in the ferroniobium alloy. The striation features are more prevalent in region 2 than region 3. ....	75

Figure 5.1: a) SEM BSE image of as-received commercial grade ferroniobium alloy showing overall microstructure. b) Higher magnification SEM BSE image of ferroniobium showing three different contrast regions labelled 1-3 .....	86
Figure 5.2: TEM BF image showing the three regions in the ferroniobium alloy. The striation features are more prevalent in region 2 than region 3 .....	88
Figure 5.3: Heating and cooling DSC curves at 10 K/min for the ferroniobium alloy .....	90
Figure 5.4: SEM BSE images of DSC ferroniobium samples after heating and cooling at different rates: a), d) 10 K/min; b), e) 20 K/min; c), f) 50 K/min .....	93
Figure 5.5: Iron-niobium binary phase diagram (redrawn/labeled) [Vob11] .....	94
Figure 5.6: a) Iron-niobium binary phase diagram showing the metastable $Fe_2Nb_3$ phase [Bej93(1)]. b) Magnified view of the niobium-rich eutectic region (compositions are given in wt.% and at.%) .....	97
Figure 5.7: Onset temperature for DSC peaks versus cooling rate. Data is extrapolated to 0 K/min .....	101
Figure 5.8: Proposed niobium-rich eutectic region of iron-niobium binary phase diagram	102
Figure 5.9: Approximate extension of liquidus and solidus (proeutectic intermetallic) lines for Scheil calculations. (The metastable lines and region are omitted for simplicity) .....	104
Figure 6.1: SEM BSE images of Steel A with 1 wt.% niobium added at 1873K (1600°C). a) and b) Ferroniobium dissolution time of 6 minutes; c) and d) dissolution time of 20 minutes; and e) and f) dissolution time of 40 minutes .....	115

Figure 6.2: a) and b) Low and high magnification TEM BF images of steel samples with 1 wt.% niobium addition (dissolution time was 6 minutes). c) – e) SAD patterns from the iron-rich and niobium-rich regions respectively .....	117
Figure 6.3: XRD pattern for Steel A with 1 wt.% niobium added (6 minutes dissolution time).....	118
Figure 6.4: a) and c) Low magnification SEM BSE images of Steel B showing coarse niobium-rich particles. b) and d) Magnified SEM BSE images of the coarse niobium-rich particles (a) and (c), respectively.....	119
Figure 6.5: SEM EDX line scan across coarse niobium-rich particles in Figure 6.4d .....	120
Figure 6.6: SEM EDX line scan across coarse niobium-rich particle in Figure 6.4b .....	120
Figure 6.7: SEM SE image of Steel B showing niobium-rich particles as well as the iron-rich matrix. Composition analysis of the points shown was done through AES.....	121
Figure 6.8: Auger spectrum for point 5 shown in Figure 6.7 .....	122
Figure 6.9: Auger spectrum for point 6 shown in Figure 6.7 .....	122
Figure 6.10: Auger mapping (carbon, nitrogen, iron and niobium) of the region shown in Figure 6.7.....	123
Figure 6.11: Iron-niobium phase diagram with a fixed amount of titanium, carbon and nitrogen (Steel B). The NbC formation curve, as a function of niobium content, is shown .....	125
Figure 6.12: Distribution of carbon, niobium and iron in the liquid steel according to the Scheil solidification model .....	126

Figure 6.13: Dotted lines used for the calculation of carbon, niobium and iron contents in the liquid steel.....	127
Figure 7.1: Representative microstructure of as-received ferroniobium alloy. The white regions are the niobium-rich solid solution phase and the darker regions are Fe <sub>7</sub> Nb <sub>6</sub> intermetallic.....	137
Figure 7.2: a) and b) Low magnification BSE images of ferroniobium ternary alloys with 5 wt.% and 10 wt.% aluminum additions, respectively, fabricated by induction melting. c) and d) Higher magnification BSE images of a) and b), respectively, showing regions labeled 1-4.....	140
Figure 7.3: a) and b) TEM bright field (BF) images of region 1 from Figure 6.2d (83-86 wt.% niobium).....	141
Figure 7.4: a), b) and c) SAD patterns taken from the region shown in Figure 6.3. The pattern in (c) can be indexed to Nb <sub>3</sub> Al; the zone axis is shown.....	142
Figure 7.5: a) and b) Low magnification BSE images of ferroniobium ternary alloys with 15 wt.% and 20 wt.% aluminum, respectively, made by induction melting. c) and d) Higher magnification BSE images of a) and b), respectively, showing three regions labeled 1, 3 and 4.....	143
Figure 7.6: a) and b) Low and high magnification BSE images of iron-niobium-aluminum ternary alloys (5wt.% aluminum) prepared by arc melting.....	148
Figure 7.7: a) and b) Low magnification BSE images of iron-niobium-aluminum ternary alloys (10 wt.% and 15 wt.% aluminum, respectively) made by arc melting. c) and d) Higher	

magnification BSE images of a) and b), respectively, showing three regions labeled 1, 3 and 4 .....	150
Figure 7.8: Solidification start temperature for different cooling rates for niobium-iron-aluminum ternary alloys, with 0 to 10 wt.% aluminum. The data is extrapolated to 0 K/min .....	152
Figure 7.9: Effect of aluminum addition on the liquidus temperature of niobium-iron-aluminum ternary alloys .....	154
Figure 7.10: Isothermal section of the niobium-iron-aluminum phase diagram at 1273 K (1000°C) [Bej93(2)].....	155

## List of Symbols and Abbreviations

A: Melt shell contact area (m)

$C_A$ : Concentration of the solute (mole/m<sup>3</sup>)

$C_m$ : Concentration of M in the melt in equilibrium with the concentration in the solid (kmol/m<sup>3</sup>)

$C_{mb}$ : Concentration in the bulk (kmol/m<sup>3</sup>)

$D_A$ : Diffusion coefficient of solute A (m<sup>2</sup>/s)

$J_{Ax}$ : Flux of atoms of solute A diffusing through a cross-sectional area normal to the x-direction in a unit of time (atoms.m<sup>2</sup>/s)

$K_y$ : Strengthening coefficient (MPa.m<sup>1/2</sup>)

L: Camera length for the TEM (m)

N: Total points on a grid

$N_b$ : Number of points laying on the boundary of two phases

$N_p$ : Number of points laying on the phase

Q: Activation energy (J/mol)

R: Universal gas constant (J/mol.K)

$R'$ : Original radius of the addition (m)

$R''$ : Distance between the central undiffracted spot and a specific diffracted spot measured from the SAD pattern (m)

S: Standard deviation

T: Temperature (K)

$V_v$ : Volume fraction of region/phase

$\bar{V}_v$ : Average of the volume fractions

$X_l$ : Composition of the liquid (wt.%)

$X_o$ : Overall composition of the alloy (wt.%)

$X_s$ : Composition of solid (wt.%)

d: Grain size (m)

$d'$ : d-spacing for the plane of interest (nm)

$f_l$ : Phase fraction of liquid

$f_s$ : Phase fraction of solid

k: Partition coefficient

$k'$ : Mass transfer coefficient (m/s)

r: Radius of alloying addition at any given time (m)

t: Dissolution time from radius  $R'$  to r (s)

x: Direction of the diffusing solute A

## Greek Symbols

$\lambda$ : Wavelength of the electrons (nm)

$\rho_m$ : Number of kmol/m<sup>3</sup> in the alloy addition

$\sigma_y$ : Lower yield strength (MPa)

$\sigma_i$ : Friction stress (MPa)

# Chapter 1: Introduction

## 1.1. Statement of the Problem

The need for development of high strength steels has been recognized as one of the most important tasks for metallurgical engineers over the past several decades. One of the way to increase the strength of steel is by increasing its carbon content. However, increasing the carbon content can mean compromising some other important mechanical properties like toughness and weldability, thus limiting the steel's use in industrial applications. This issue has led to the development of microalloyed steels which have reduced carbon content (*i.e.*, as low as 0.06 wt.% or even lower) and contain titanium, niobium and/or vanadium as alloying elements in small amounts usually less than 0.1 wt.% in total. These alloying elements contribute to increasing strength through grain refinement, solid solution strengthening and precipitation strengthening without compromising toughness and weldability.

These important alloying elements, *i.e.*, niobium, titanium and vanadium, are added in the form of their respective ferroalloys. Generally speaking ferroalloys are usually categorized as Class 1 or Class 2. Class 1 ferroalloys have melting points lower than the steelmaking temperatures and Class 2 ferroalloys have melting points higher than the steelmaking temperatures. Class 2 ferroalloys will not melt when added during steelmaking, but rather dissolve in the molten steel which is a slow and sluggish process. In the past, the focus has been on whether a particular ferroalloy belongs to Class 1 or Class 2 and attention was not paid to the presence of high melting temperature, thermally stable phase(s) within the ferroalloys regardless of class.

As already mentioned, microalloyed steels contain niobium, titanium and/or vanadium and they are added as ferroniobium, ferrotitanium and ferrovanadium, respectively. The elements form precipitates of nitrides, carbides and/or carbonitrides in microalloyed steels. The effectiveness of these precipitates depends on their size and distribution in the matrix; for best results they should be small in size and uniformly distributed. Several studies have reported the presence of coarse niobium-, titanium- and (Nb,Ti)-rich particles in microalloyed steels. It has been suggested that they arise from undissolved phases of as-received ferrotitanium and ferroniobium alloys. These coarse particles have a deleterious effect on mechanical properties by acting as crack initiation sites. In order to prevent the coarse particles from forming in microalloyed steels, high melting point, thermally stable phases in ferroalloys need to be characterized and eliminated.

There are some challenges related to achieving the above goal. Since both types of ferroalloys contain significant amounts of impurities, characterization of the ferroalloys is required, rather than solely relying on binary phase diagrams. This requires understanding of the ferroalloy's solidification behavior, which can be complex particularly in the presence of impurities. Afterwards, a study of the coarse niobium-rich particles in different grades of steel samples is needed to relate them to the undissolved phase(s) in the ferroniobium alloy. Finally, devising a methodology to eliminate the high melting temperature phase(s) in as-received ferroniobium without significantly affecting the overall ladle addition process is another challenge. Whatever route is followed for the above purpose, it should not increase the overall liquidus temperature of the as-received ferroniobium alloy above the steelmaking temperature, *i.e.*, ~ 1600°C.

## 1.2. Objectives and Methodology

In order to resolve the above mentioned issues related to ferroalloy additions to steelmaking, the following objectives are defined:

- 1) Identification of phases present in as-received ferroniobium and ferrotitanium alloys.
- 2) Understanding of the microstructural evolution of as-received ferroniobium alloys.
- 3) Study of coarse niobium- and titanium-rich particles present in different steel grades.
- 4) Explore a method by which we can eliminate the high melting temperature phase(s) in the ferroniobium alloy.

In order to achieve the above objectives the following methods were used:

- 1) Characterization of as-received ferroniobium and ferrotitanium alloys was done using the following tools:
  - a) Scanning electron microscopy (SEM) along with energy dispersive spectrometry (EDX) and wavelength dispersive spectrometry (WDX).
  - b) X-ray diffractron (XRD).
  - c) Transmission electron microscopy (TEM) along with energy dispersive spectrometry (EDX).
- 2) Microstructural evolution of as-received ferroniobium alloy was studied using differential scanning calorimetry (DSC).
- 3) Composition modification of as-received ferroniobium (addition of aluminum) was done in an induction furnace, in the presence of a positive inert argon atmosphere.

- 4) To observe the effect of adding aluminum on the liquidus temperature of ferroniobium alloy, ternary master alloys were prepared. Pure niobium, iron and aluminum were melted in an arc melting unit with a positive inert atmosphere of argon.
- 5) Characterization of the new alloys was done using SEM, TEM, XRD and DSC tools.
- 6) With the aid of characterization tools, a threshold composition (the amount of aluminum) was established that eliminates the high melting temperature phase of the as-received ferroniobium alloy, without significantly increasing the melting range of alloy.

### **1.3. Outline of Thesis**

Chapter 2: A literature review based on the overall problem statement is presented. It includes some examples of the presence of coarse niobium-, titanium- and (Nb,Ti)-rich particles in steels, ferroalloys, manufacturing of ferroniobium and ferrotitanium as well as phase diagrams for the iron-niobium, iron-titanium and iron-niobium-aluminum systems.

Chapter 3: All the experimental procedures used throughout the thesis are presented.

Chapter 4: In order to identify different phases and especially the high melting temperature phases of the ferroalloys, characterization of the as-received ferroniobium and ferrotitanium alloys is done.

Chapter 5: Once the high melting temperature phase(s) of the as-received ferroniobium are identified, microstructural evolution of the as-received ferroniobium alloy is done.

Chapter 6: Coarse niobium-rich particle in different steel samples are characterized. Thermodynamic evaluation of the systems is done to investigate the segregation of carbon,

nitrogen and niobium, resulting in the formation of niobium-rich particles at elevated temperatures.

Chapter 7: The as-received ferroniobium alloy is chemically modified in order to eliminate high melting temperature phase(s). The effect of aluminum additions on the liquidus temperature of the as-received ferroniobium alloy is studied using DSC. Microstructural characterization of new ternary alloys by SEM and TEM is also discussed.

Chapter 8: The work is summarized in the Conclusions and future recommendations are proposed.

## Chapter 2: Literature Review

### 2.1. Introduction

Microalloyed steels have gained significant importance in the last few decades due to their high strength and high toughness. These properties of microalloyed steels are attributed to small alloying additions (usually less than 0.1 wt.%). Titanium, niobium and/or vanadium are added to microalloyed steels for high strength and toughness. These alloying additions are added in form of their respective ferroalloys, *i.e.*, ferrotitanium, ferroniobium and ferrovanadium. The elements increase strength and toughness by different strengthening mechanisms, including solid solution strengthening, grain refinement and precipitation strengthening. The precipitates are usually carbides, nitrides and/or carbonitrides. [Cal07, Gal97]

The effectiveness of the aforementioned precipitates depends on their size and the uniformity with which they are dispersed in the matrix [Dav01]. Finer and uniformly distributed precipitates will provide the maximum contribution in improving strength through precipitation hardening. If the precipitates are coarse in size and non-uniformly distributed, then they can even retard mechanical properties by acting as crack initiation sites. There is extensive literature reporting the adverse effect of coarse titanium- and niobium-rich precipitates in microalloyed steels on mechanical properties [Abr06(1), Abr06(2), Che87, Cra00, Men99, Pot01, Rob84, Tia07, Yua09, Zho96, Zhu07, Zhu08]. Some of the researchers believe that the source of these precipitates is undissolved high melting temperature phases in their respective ferroalloys [Abr06(1), Abr06(2), Men99]. The aim of this project is to identify any high melting point phases in ferrotitanium and ferroniobium alloys and to devise a strategy, as necessary, to eliminate them in the ferroniobium alloy. The

proposed methodology was based on alloying the ferroniobium such that all phases formed have melting points lower than that of the steel. The elimination of high melting temperature phase(s) in ferrotitanium was considered to be beyond the scope of the current study and can be pursued in the future.

In this section, a detailed literature review is presented with the aim of understanding the nature and effect of “coarse precipitates in steel”. This literature review is divided into several parts. First of all microalloyed steels are discussed. Then the problem statement is discussed in detail, elaborating the possible causes for the presence of coarse precipitates in steel. Specifically, two possible sources are discussed, *i.e.*, precipitation during solidification and undissolved phases from ferroalloys. A section on ferroalloys follows, which includes their production route, the different types and their dissolution behavior. Binary systems for iron-niobium and iron-titanium are then discussed in order to predict possible high melting temperature phases in ferroniobium and ferrotitanium. Lastly, possible methods are proposed to modify the chemistry of ferroniobium alloys to eliminate high melting temperature phases in as-received ferroniobium. Aluminum is a promising addition for ferroniobium alloys; as such, the aluminum-iron-niobium phase diagram is covered in the last section of the literature review.

## **2.2. Microalloyed Steels**

The traditional way for increasing the strength of steel is by increasing its carbon and/or manganese content. Unfortunately this increase in its strength comes at the expense of toughness. Alternatively, the development of microalloyed steels, which contain only small amounts of carbon ( $< 0.1$  wt.% C; in some cases  $< 0.06$  wt.% [Dav01]), but have improved strength and

toughness, has ensued. Microalloyed steels are steels with two to three times higher yield strength compared with conventional plain carbon-manganese steels. Microalloyed steels contain small amounts of alloying additions, usually vanadium, titanium and niobium. The amount of these alloying additions is less than 0.1 wt.%. The strengthening effect of these alloying additions depend on thermal and thermo-mechanical treatments.

The yield strength of steels can be increased by various strengthening mechanisms, such as the ones listed below and discussed in the following pages [Gla97].

- a) Solid solution strengthening;
- b) Grain refinement;
- c) Precipitation strengthening;
- d) Work hardening.

### **2.2.1. Solid Solution Strengthening**

Solid solution strengthening, due to solute additions, results from generation of strain fields. These strain fields interact and impede the motion of dislocations resulting in improved strength. This interaction of strain fields with dislocations can be elastic, electrical, chemical and/or geometrical. [Gla97]

### **2.2.2. Grain Refinement**

Refinement of grain size has a direct effect on the yield strength of a material. This is evident from the Hall-Petch equation shown below:

$$\sigma_y = \sigma_i + K_y d^{-0.5} \quad \text{Equation 2.1}$$

where  $\sigma_y$  is the lower yield strength,  $\sigma_i$  is the friction stress,  $K_y$  is the strengthening coefficient and  $d$  is the grain size.

The ease/difficulty with which dislocations move defines strength of a material. Grain boundaries offer resistance to the motion of a dislocation. When a dislocation arrives at a grain boundary it faces the discontinuity of the slip plane and direction due to the different orientation of the adjacent grain. A finer grain size offers more grain boundaries and subsequently higher strength. [Gla97]

### **2.2.3. Work Hardening**

Work hardening, sometimes referred as strain hardening, is the strengthening of a material due to plastic deformation. As stated above, the strength of a material relies on dislocations and their interactions. During work hardening, the number of dislocations increases as a result of the formation of new dislocations and multiplication of dislocations. As the number of dislocations is increased, the average distances between the dislocations decreases. The force between two dislocations is repulsive in nature; therefore, the motion of dislocations is hindered due to their increased number and, consequently, strength is increased. [Cal07]

### **2.2.4. Precipitation Strengthening**

In microalloyed steels, precipitation strengthening is major strengthening mechanism. The fine precipitates, usually carbides/nitrides, are formed during the austenite to ferrite transformation.

There are several ways through which the presence of fine precipitates in microalloyed steels contributes to a substantial increase in strength. Some of these are [Gla97]:

- 1) Coherency strengthening: arises because a coherent precipitates develops coherency strain in the matrix surrounding it.
- 2) Chemical hardening: arises due to dislocations cutting precipitates. The strength is increased a) due to creation of antiphase boundaries for ordered precipitates, b) due to an increase in precipitate/matrix interfacial area and c) because the separation distance of dissociated dislocations is altered because of different stacking fault energies.
- 3) Dispersion hardening: arises due to the fact that precipitates are hard and not deformable. As a result dislocation loops are formed around them. Dislocations experience extensive bowing due to the hard nature of these precipitates, as seen in Figure 2.1.

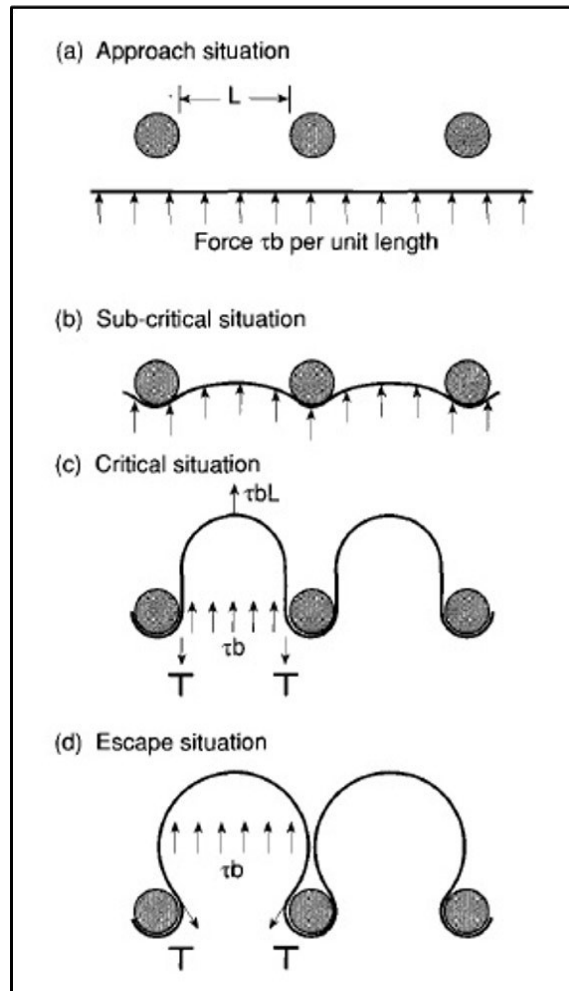


Figure 2.1: Formation of loops by a dislocation around a hard and non-deformable precipitate. [Gla97]

### 2.3. Presence of Coarse Niobium- and Titanium-rich Particles in Microalloyed Steels (Problem Statement)

The two alloying elements under study here are niobium and titanium. Niobium is added to microalloyed steels to produce nitrides and/or carbides, which retard recovery and recrystallization during the hot rolling process. Moreover, niobium also contributes to solid solution strengthening and grain refinement [Gla97]. For every 0.01 wt.% niobium addition, strengthening is expected to

increase by 35 to 40 MPa [Dav01]. Titanium is added to microalloyed steels to improve the toughness of the heat affected zone during high temperature operations, especially welding, by forming stable titanium nitride precipitates. TiN precipitates are stable to high temperatures, so that during the welding operation they help suppress austenite grain growth in the HAZ region. The hard, stable titanium and niobium precipitates result in precipitation hardening as well [Gla97].

The presence of precipitates in steel improves its mechanical properties, but a lot depends on the size and shape of these precipitates. It has been observed that there is a substantial decrease in strengthening contribution when the size of these precipitates decreases [Gla97]. Figure 2.2, shows how the size of niobium carbide particles can affect the lower yield strength of HSLA steels [Dav01]. A decrease in the size of precipitates improves the strength. For example, with a 0.04 wt.% niobium addition the yield strength is increased by approximately 155 MPa for a NbC particle size of 1 nm compared with an increase of only 17 MPa (approximately) for a NbC particle size of 10 nm.

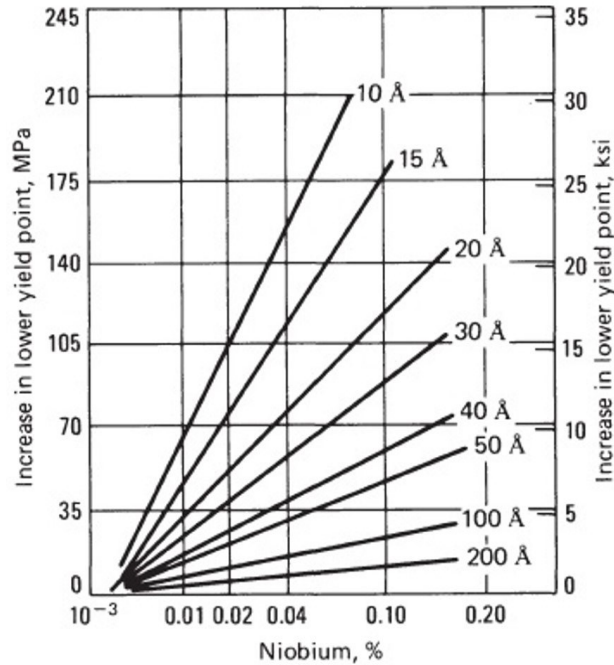


Figure 2.2: Effect of niobium carbide on yield strength for various sizes of niobium carbide particles.

[Dav01]

In fact, coarse precipitates can retard the mechanical properties of steel. The presence of coarse niobium and titanium-rich particles in microalloyed steels has been extensively reported in literature. Figure 2.3 shows some examples of the presence of coarse niobium- and titanium-rich particles in steel [Abr06(2)]. These coarse particles adversely affect the mechanical properties by acting as crack initiation sites. The composition of these particles is not fixed; instead, the composition varies from very simple to complex non-stoichiometric values. [Abr06(1), Abr06(2), Che87, Cra00, Men99, Pot01, Rob84, Tia07, Yua09, Zho96, Zhu07, Zhu08]

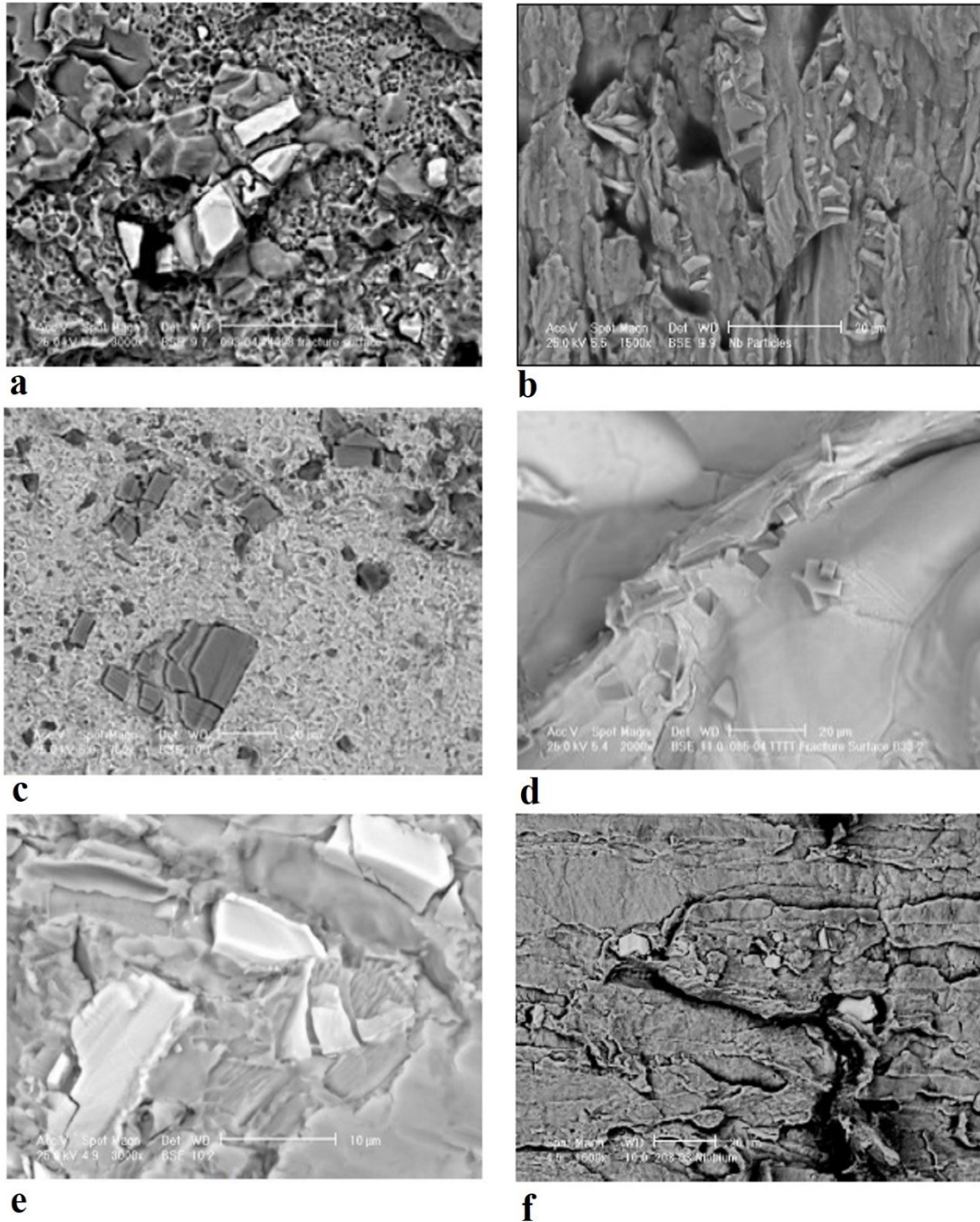


Figure 2.3: a) Niobium-rich phase in the exposed fracture surface of a hook crack; b) Niobium-rich phase on an exposed fractured tensile specimen; c) Titanium-rich phase in exposed fracture surface of a hook crack; d) Titanium-rich phase in the mid-section of product; e) coarse niobium-rich particles on exposed surface of the mid-thickness cracks of a specimen; f) Niobium-/Titanium-rich particles along the mid-thickness of a specimen. [Abr06(2)]

There are two different hypotheses associated with the origin of these particles in microalloyed steels.

- a) Hypothesis 1: According to some researchers, these particles start to precipitate during the continuous casting process in the tundish or mold. The coarsening of these particles is associated with the prolonged casting time in the continuous casting machine. Robert [Rob84] has argued that the formation/precipitation of coarse particles (TiN) may have taken place in the liquid state. Chen et al. [Che87] also present a similar theory that the presence of complex precipitates (Nb,Ti)(C,N) is associated with solidification. According to Chen et al., TiN precipitates (more than 0.5  $\mu\text{m}$  in size) form in liquid steel. These precipitates remove titanium from the austenite phase and as a result reduce any further precipitation. Chen et al. also studied dendritic shape particles (up to 10  $\mu\text{m}$  in size); they were TiN-rich (TiNb)(C,N) in niobium-vanadium-titanium steel and NbC-rich (TiNb)(C,N) in niobium-titanium steel. They attributed presence of these particles to the high concentrations of titanium and nitrogen, along with extensive segregation of niobium in the inter-dendritic liquid. Zhou et al. [Zho96] attributed the formation of coarse precipitates like TiN to segregation. Yuan et al. [Yua09] have also reported the presence of complex precipitates (Nb,Ti)(C,N) associated with solidification. The authors concluded that the precipitates are initially titanium-rich in nature but as solidification proceeds they become niobium-rich due to the higher concentration of niobium in the austenitic matrix.
- b) Hypothesis 2: Some researchers also believe that the coarse particles are associated with certain high melting temperature phases in ferroalloys added during the steelmaking process [Abr06(1), Abr06(2), Men99]. According to Mendoza et al. [Men99] and Abraham et al. [Abr06(1), Abr06(2)], the presence of coarse particles is related to undissolved ferro-

residues during the steelmaking process. Abraham et al. studied, in detail, ferroalloys and coarse particles present in steel. They supported their findings with the following two main arguments: the phases present in the ferroalloys are believed to be a component of the coarse particles and the ferroalloys have a melting point higher than the steelmaking process temperature. As such, there is the chance that the phases are not completely dissolved when added to molten steel. These undissolved phases of the ferroalloys react with carbon and nitrogen present in steel and form their respective carbides, nitrides or carbonitrides.

Whether these coarse particles should be designated as inclusions or precipitates is still under debate. By convention, particles which are present in liquid steel are inclusions and particles which come out in the solid state are called precipitates. [Abr06(1)]

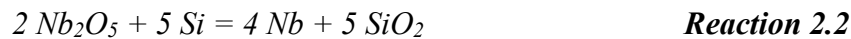
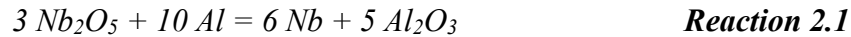
## **2.4. Ferroalloys**

Ferroalloys are alloys with one or more than one alloying element with iron. They are used to add certain elements to the molten liquid. The bulk of ferroalloys (85 to 90 %) produced are used in the steel industry, while a small amount is utilized in non-ferrous industry as well. Initially, the production of ferroalloys was started in the blast furnace. However, this method has two limitations, *i.e.*, the process cannot produce ferroalloys with 1) low carbon content and 2) the ferroalloys have a high affinity for oxygen. Therefore, in the beginning of 20th century electric furnaces replaced blast furnaces for the production of ferroalloys. Currently, submerged arc furnaces are used for the production of ferroalloys. [Gas13]

### 2.4.1. Production of Ferroniobium

Niobium finds its utility in steel due to its strong tendency to form finely dispersed carbides and nitrides. Small niobium additions are also known to improve the corrosion resistance of iron alloys. Niobium ore with 0.15 % to 0.2 %  $Nb_2O_5$  is considered to be enriched enough for extraction [Gas13]. The largest reserves of niobium in the form of pyrochlore ore are present in Araxa, Brazil. The niobium reserves in Araxa are being exploited by CBMM, which has emerged as the largest producer of ferroniobium. The following section will show in detail the production route of ferroniobium alloys by CBMM. [Sou01]

Niobium pentaoxide can be reduced with aluminum, silicon and carbon by the following reactions:



Ferroniobium is usually not manufactured by carbothermic reduction due to formation of NbC, which could add carbon to the ferroniobium alloy. Lower and stable niobium oxides are produced as a result of reduction of niobium with silicon, due to its incomplete reaction. Aluminothermic reduction process is the most suitable method for ferroniobium production. The amount of energy released in Reaction 1 is not enough to keep the bath in the molten state. Therefore, the extra energy needed is provided by Reaction 2.5.



Since the year 2000, CBMM has used an additional pyrometallurgical process for refining concentrates. This process removes sulphur, lead and phosphorus by sintering and subsequent smelting in an electric arc furnace. Figure 2.4 shows the CBMM's production capacity, their sales and the world's ferroniobium demand.

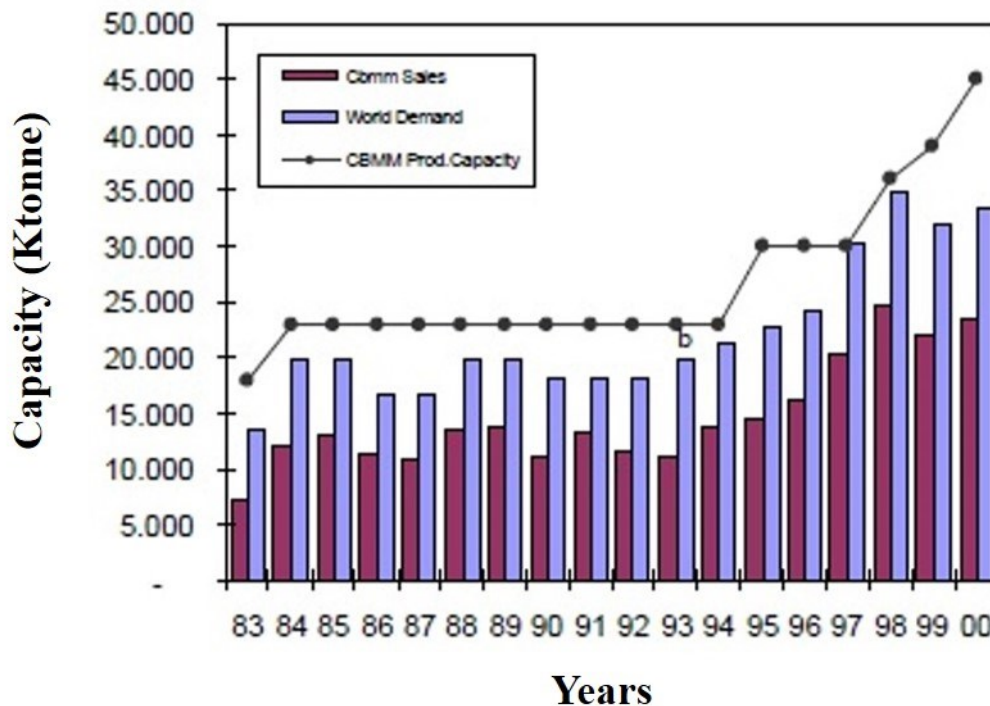


Figure 2.4: World demand for ferroniobium and CBMM's sales and production capacity. [Sou01]

### 2.4.2. Production of Ferrotitanium

Several titanium minerals are known to exist in nature. These are rutile, ilmenite, perovskite, pyrochlore and sphene. Ilmenite ( $\text{FeO} \cdot \text{TiO}_2$ ) is the most important of these titanium minerals. Usually 96 % to 98 % ilmenite (equal to 50 wt.% to 65 wt.%  $\text{TiO}_2$ ) is present in ilmenite concentrates. However, these concentrates also contain 0.2 wt.% to 0.25 wt.% phosphorus. This phosphorus can be eliminated by roasting the concentrates in a rotary kiln between 873 K and 1073

K (600°C and 800°C). This also results in oxidation of FeO and formation of Fe<sub>2</sub>O<sub>3</sub>. For reduction purposes there are again three elements that can be used, *i.e.*, carbon, silicon and aluminum. The aluminothermic method is the most common method. Both ilmenite and rutile concentrates are reduced using the aluminothermic process. The reduction process initially forms an intermediate monoxide, which can form titanium aluminate because of its basic nature. The formation of titanium aluminate, however, decreases the TiO activity. In order to avoid this aluminate formation, lime (CaO) is introduced. This CaO forms CaO·Al<sub>2</sub>O<sub>3</sub>, thus replacing TiO. Excessive lime additions should be avoided as they can have a negative effect on the overall reaction due to the formation of perovskite (CaO·TiO<sub>2</sub>). This technique for production of ferrotitanium has seen great improvements in last few years. A couple of these improvements are preheating of the charge and the use of an iron-thermal mixture (exothermic). [Gas13]

### **2.4.3. Classification of Ferroalloys**

On the basis of the dissolution behavior of alloying additions into the steel melt, ferroalloys can be classified into two categories. [Eng92]

Type 1: Alloying additions with melting points lower than that of the steelmaking process: these generally melt and are dispersed in the bulk liquid.

Type 2: Alloying additions with melting points above that of the steelmaking process: these are difficult to dissolve and usually require more time.

When type 1 ferroalloys are added during the steelmaking process, a solid shell of the frozen bath material will form around them. The ferroalloy surrounded by the solid shell will continue heating and its temperature will start rising. Since the melting point of ferroalloy is lower than the

steelmaking temperature, the ferroalloy generally melts inside the steel shell. For ferroalloys with melting points higher than the steelmaking temperature (type 2), the frozen steel shell will dissolve first followed by dissolution of the solid ferroalloy which is mass transfer controlled. Thus, the time for dissolution of ferroalloys with melting points higher than the steelmaking process is increased compared with type 1 ferroalloys. [Gou84]

For ferroniobium it is believed that when commercial grade ferroniobium is added during the steelmaking process it does not melt. In fact, such ferroniobium when incorporated in the melt progressively dissolves, which may result in a chemical reaction between the surface of the ferroalloy and the melt [Cos92]. Figure 2.5 shows a comparison of dissolution/melting of the two types of ferroalloys.

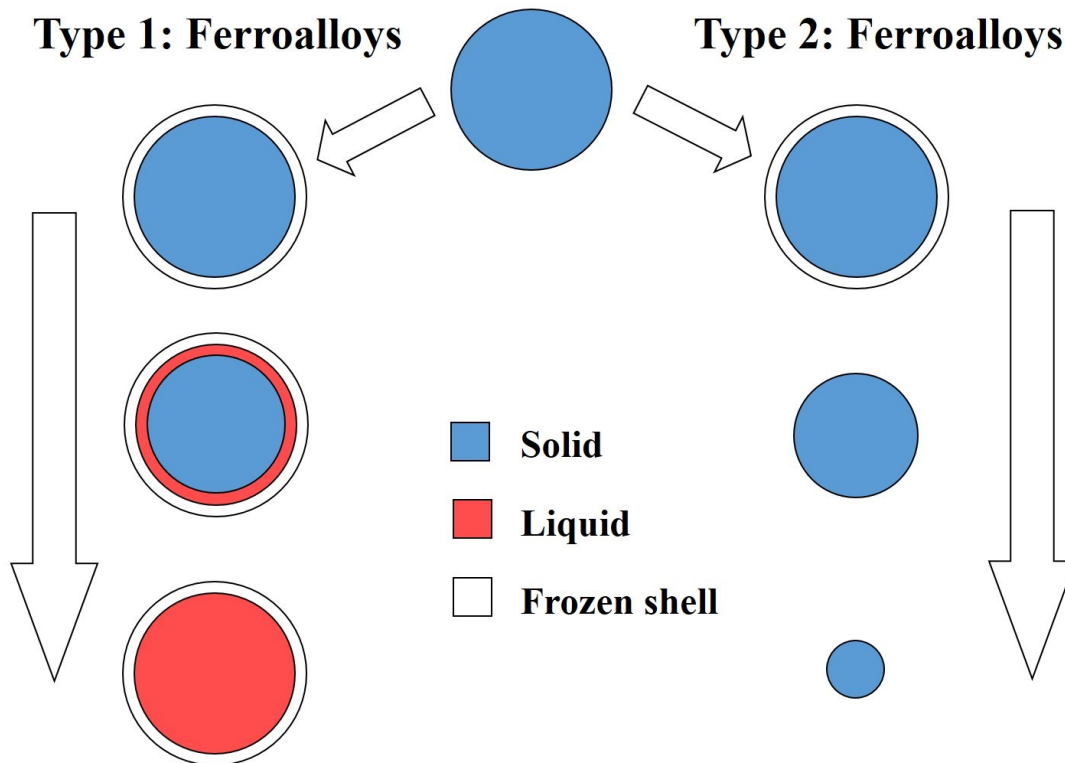


Figure 2.5: Melting and dissolution behavior of two types of ferroalloys.

## **2.4.4. Dissolution of Ferroalloys**

### **2.4.4.1. Factors Effecting Dissolution Behavior**

The dissolution behavior of alloying additions in steel is dependent on many factors: [Abr06(1)]

- 1) Their solubility in the steel;
- 2) Their melting temperatures;
- 3) Their density and particle size;
- 4) The steelmaking temperature;
- 5) Fluidity of melt;
- 6) Stirring intensity;
- 7) Chemical free energy gradient.

In addition to these factors, surface tension, drag force and the buoyancy force also play a role in the dissolution of ferroalloys in steel [Loz07]. According to some researchers, the main driving force for dissolution of ferroalloys in steel is the concentration gradient (obeying Fick's First Law). However, according to Darken, the chemical free energy gradient is also responsible for the dissolution mechanism along with the concentration gradient. [Abr06(1)]

### **2.4.4.2. Temperature Dependence**

The rate of dissolution of a solute "A" depends on temperature number of variable described in this section. Considering Fick's first law of diffusion which is given by equation 2.2 [Por92]:

$$J_{Ax} = (-D_A) \left( \frac{\partial C_A}{\partial x} \right) \quad \text{Equation 2.2}$$

where  $J_{Ax}$  (atoms.m<sup>2</sup>/s) is flux of atoms of solute A diffusing through a cross-sectional area normal to the x-direction in a unit of time and  $D_A$  (m<sup>2</sup>/s) is the diffusion coefficient of solute A,  $C_A$  is the concentration of the solute (moles/m<sup>3</sup>), and x is the direction of the diffusing solute A.

The dependence of the diffusion coefficient on temperature can be expressed by the Arrhenius equation:

$$D_A \propto \exp \left( -\frac{Q}{RT} \right) \quad \text{Equation 2.3}$$

where Q is the activation energy, R is universal gas constant and T is temperature.

By combining the two equations it can be seen that the rate of dissolution of a solute into the bulk depends on the diffusion coefficient of that solute, its concentration gradient in the bulk and the temperature of the system. If we have a high concentration gradient but the diffusion coefficient value is low (due for example to a lower temperature), then dissolution will be negatively affected and will be slow.

#### **2.4.4.3. Dissolution Time**

The dissolution time for ferroalloys which have a melting temperature higher than that of the melt appears to be dependent on temperature. Such alloys dissolve by mass transfer in the melt boundary layer. Convection and diffusion in the melt boundary layer proceeds more rapidly as compared with solid state diffusion. This means that when the initially formed solid shell is melted, dissolution is determined by the mass transfer coefficient  $k'$ . It is assumed that when the solid

surface is heated to the bath temperature (after melting of the solid shell), its composition remains unchanged. Secondly, it is assumed that dissolution takes place at a well-defined planar front (dissolution sometimes does not proceed in a planar manner) [Eng92].

The number of moles of M (metal) removed per unit time from the alloy addition is equal to the flow of moles of M transferred through the diffusion boundary layer in the melt, *i.e.*:

$$\left(\frac{dr}{dt}\right)(A \rho_m) = (k'/A)(C_m - C_{mb}) \quad \text{Equation 2.4}$$

where  $(dr A)/dt$  is the volume of the alloy removed per unit time,  $k'$  is the mass transfer coefficient,  $A$  is the melt shell contact area,  $r$  is the radius,  $\rho_m$  is the number of  $\text{kmol}/\text{m}^3$  in the alloy addition,  $C_m$  is the concentration of M in the melt in equilibrium with the concentration in the solid in the units of  $\text{kmol}/\text{m}^3$  and  $C_{mb}$  is the concentration in the bulk.

Equation 2.4 indicates that  $C_m - C_{mb}$  is the driving force for diffusion through the melt boundary layer. Integrating the above equation (disregarding the dependence of  $k'$  on  $r$ ) gives:

$$t = \frac{(\rho_m)(R' - r)}{(k')(C_m - C_{mb})} \quad \text{Equation 2.5}$$

Here  $R'$  is the original radius of the addition and  $t$  is the dissolution time from radius  $R'$  to  $r$ . The total time for complete dissolution can be given as:

$$t_d = \frac{(\rho_m)(R')}{(k')(C_m - C_{mb})} \quad \text{Equation 2.6}$$

Recall that for the final total time one must add the shell time  $t_s$  (melting time for the initially frozen metal shell which is formed at the surface) to the  $t_d$  value. The mass transfer coefficient  $k'$  is directly proportional to the diffusion coefficient and from Equation 2.3 it is clear that the

diffusion coefficient is dependent on temperature. Thus, the time for dissolution of ferroalloys in a molten bath depends upon the temperature of the bath as well.

#### **2.4.4.3.1. Dissolution of Pure Niobium and Ferroniobium Alloy**

Argyropoulos et al. [Arg82] predicted dissolution behavior of various ferroalloys including ferrosilicon, ferromolybdenum, ferrovandium, ferroniobium, ferrochrome and ferrotungsten. As already mentioned in Section 2.4.4.1. there are several factors that affect dissolution/melting for ferroalloys in a liquid bath. According to the authors [Arg82], in addition to the melting temperature of ferroalloys, the following factors also play a crucial role in their dissolution behavior.

- 1) Lump size;
- 2) Alloy solubility;
- 3) Bath temperature;
- 4) Bath convection.

To which class a ferroalloy belongs (either dissolving or melting) when added to steel bath is the most crucial factor. A simple example is a comparison of an equal size of ferrosilicon and ferrotungsten additions. A 6 cm spherical ferrotungsten addition will require more than 3000 seconds (without stirring of the bath) to dissolve as compared with an equal size of ferrosilicon which will require less than 60 seconds to melt (under the same conditions). Similarly, as the size of the ferroalloy is increased, the time required for its dissolution also increases. It should be noted that Equation 2.6 also emphasizes the importance of size of the original addition in molten steel.

Figure 2.6 shows how the dissolution of pure niobium and ferroniobium (65 wt.% niobium) spheres are affected by their size and by molten bath stirring. The curve labeled 1 in both a) and b) shows dissolution behavior without stirring. It is important to realize the importance of stirring. Without stirring a ferroniobium sphere 6 cm in size can require almost 35 minutes to dissolve. It is also evident from Figure 2.6 that under similar conditions of size, temperature and stirring, pure niobium will take nearly 1.5 times more time to dissolve compared with a ferroniobium alloy.

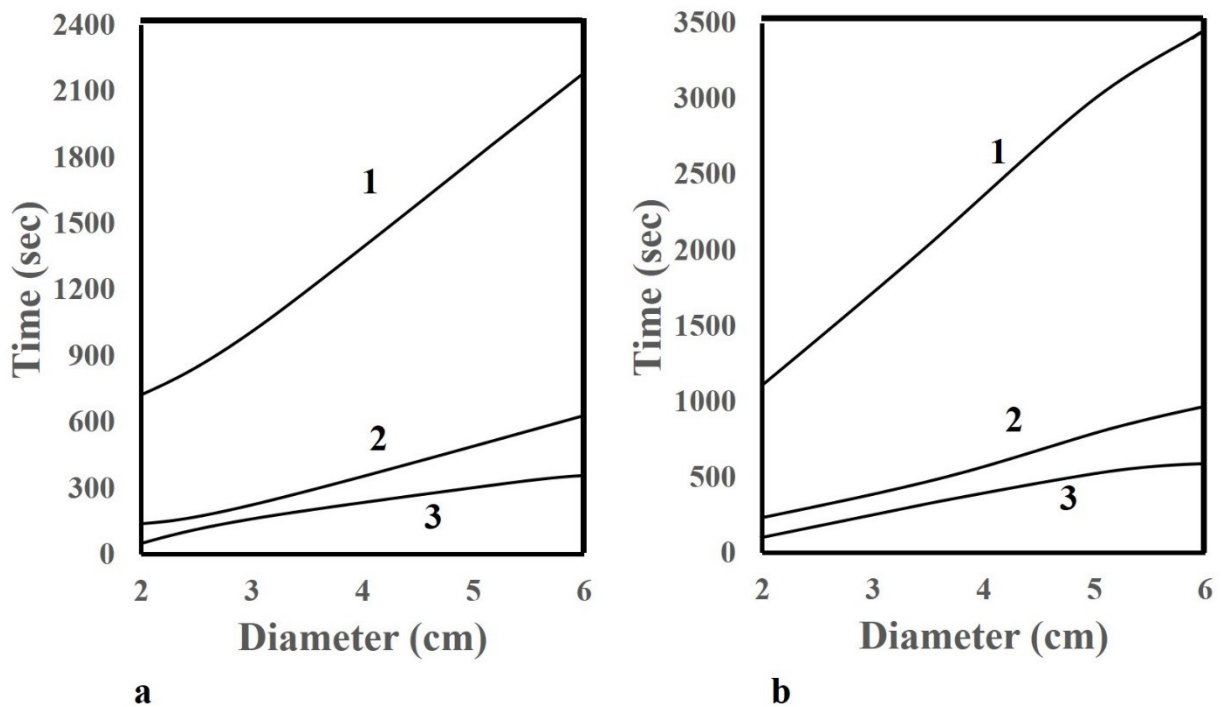


Figure 2.6: Predicted dissolution time for a) 65 wt.% ferroniobium; b) pure niobium spheres immersed in liquid steel baths at 1873 K (1600°C). (1: prediction for 100 % convection; 2: combined natural and forced convection and 3: 0.9 ms<sup>-1</sup> steel velocity past the sphere) (redrawn). [Arg82]

#### **2.4.4.4. Dissolution Heat**

It has been reported that the effect of adding ferroalloys to steel results in release of heat due to an exothermic reaction between the iron and the ferroalloys [Abr06(1)]. If that was the case, then there would be complete dissolution of the ferroalloys in steel. Gourtsoyannis et al. [Gou84], citing ferroniobium and ferromolybdenum as examples, argued that the ferroniobium used commercially has high melting temperature phases, which nullify the effect of any exothermic reaction.

According to Argyropoulos et al. [Arg84], microexothermicity (exothermicity observed in powder alloy compacts) has a beneficial effect on dissolution kinetics by the formation of an intermetallic compound, during the dissolution of the ferroalloy compact in the liquid steel. However, if an intermetallic compound with a high melting point is already present in the ferroalloy, then this effect is diminished. According to the authors, macroexothermicity (exothermicity observed in lump ferroalloys) due to the heat of mixing of liquid steel and lumps of ferroalloy has a positive effect on dissolution kinetics.

According to Abraham et al. [Abr06(1)], dissolution depends upon two steps. The first step is melting of the ferroalloy and the second step is the dispersion of the ferroalloy atoms in the bulk. The second step is exothermic but the first step is endothermic in nature. The melting of ferroalloys like ferrotitanium and ferroniobium is an endothermic process; however, the dissolution of these ferroalloys results in an exothermic reaction (titanium with nitrogen and niobium with carbon). In most ferroalloys, the overall reaction is endothermic.

### 2.4.5. Iron-Niobium System

Considerable study has been done on the binary iron-niobium system by various researchers [Bej91, Bej93(1), Gol57, Ich89, Kri68, Kub82, Lu84, Oka93, Oka95, Oka02, Pau86, Ram66(1), Ram67, Rap94, Sch96, Sri94, Vob11, Wet69]. The first complete iron-niobium binary diagram was proposed by Goldschmidt [Gol57] in 1957 and was considered valid until 1982. Other than the solid solution phases, he reported four intermetallic phases, *i.e.*

- 1) Fe<sub>2</sub>Nb Laves phase;
- 2) Fe<sub>21</sub>Nb<sub>19</sub>;
- 3) Fe<sub>2</sub>Nb<sub>3</sub>;
- 4) Unidentified high temperature phase with almost 94 wt.% iron.

Raman [Ram66(1), Ram67], however, identified only two intermetallic phases: Fe<sub>2</sub>Nb Laves phase and Fe<sub>21</sub>Nb<sub>19</sub>. The Fe<sub>21</sub>Nb<sub>19</sub> phase identified by Raman had a different crystalline structure than that proposed by Goldschmidt. Raman also tried to alloy the binary system with carbon, silicon and aluminum to confirm the existence of Fe<sub>2</sub>Nb<sub>3</sub> phase and concluded that this phase does not exist. Kripyakevitch et al. [Kri68] identified the Fe<sub>2</sub>Nb<sub>3</sub> phase, but attributed its presence to reaction with oxygen. Lu and Jack [Lu85] investigated the binary ferroniobium system, for additional intermetallic phases, and concluded that the Fe<sub>2</sub>Nb<sub>3</sub> may be an oxide (Fe<sub>6</sub>Nb<sub>6</sub>O) or nitride phase (Fe<sub>3</sub>Nb<sub>3</sub>N). Kubaschewski [Kub82] reported the Fe<sub>2</sub>Nb<sub>3</sub> phase with a melting point of 2063K (1790°C). Paul et al. [Pau86] in 1986 assessed the iron-niobium binary phase diagram on the basis of all previous studies and eliminated the possibility of Fe<sub>2</sub>Nb<sub>3</sub> and the unidentified high temperature phase (94 wt.% iron) in the system. Bejarano et al. [Bej91] observed the Fe<sub>2</sub>Nb<sub>3</sub> phase in DTA samples solidified at 5 K/min (5°C/min). He found two thermal events at 1763 K (1490°C) and 1733 K (1460°C) and attributed them to the precipitation and dissolution of this

phase, respectively; thus concluding  $\text{Fe}_2\text{Nb}_3$  to be metastable in nature. However, his experimental phase diagram did not match the work of Paul and Swartzendruber. Bejarano et al. reinvestigated the system in 1993 [Bej93(1)] and reported a difference in the homogeneity range of FeNb and  $\text{Fe}_2\text{Nb}$  intermetallic phases as compared with the results of Paul and Swartzendruber. Srikanth et al. [Sri94], however, eliminated the problem by taking the FeNb phase as a line compound. Raposa et al. [Rap94] studied the phases in the iron-niobium system and did not find any  $\text{Fe}_2\text{Nb}_3$  phase. Okamoto [Oka93, Oka95, Oka02] studied the phase diagram at various stages and did not report  $\text{Fe}_2\text{Nb}_3$  phase. Schon et al. [Sch96] studied the intermetallics of commercial grade iron-niobium alloys and concluded that sulphur, phosphorus and titanium are responsible for stabilizing the  $\text{Fe}_2\text{Nb}_3$  phase. The latest phase diagram (Figure 2.7) by Vob et al. [Vob11] also does not consider the  $\text{Fe}_2\text{Nb}_3$  phase. According to Vob et al., in a pure binary system of iron and niobium, the following phases are present as shown in the phase diagram (Figure 2.7) [Vob11]:

- 1) The liquid phase (L);
- 2) Niobium-rich solid solution BCC (Niobium);
- 3) Gamma iron FCC ( $\gamma$ -iron);
- 4) High temperature delta iron BCC ( $\delta$ -iron);
- 5) Low temperature alpha iron BCC ( $\alpha$ -iron);
- 6) Intermetallic compound  $\text{Fe}_7\text{Nb}_6$  ( $\mu$ );
- 7) Intermetallic compound Laves phase with composition near  $\text{Fe}_2\text{Nb}$  ( $\epsilon$ ).

Therefore, the only phase present at room temperature with a melting temperature higher than the steelmaking temperature is the niobium-rich solid solution (with iron).

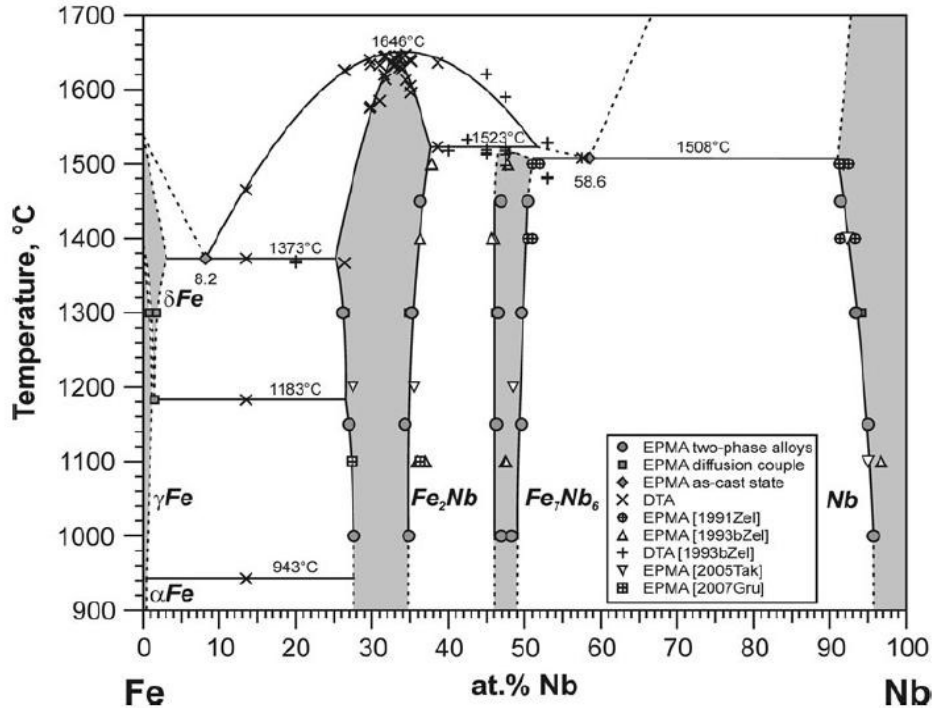


Figure 2.7: Iron-Niobium binary phase diagram [Vob11].

### 2.4.6. Iron-Titanium System

The iron-titanium binary phase diagram has been studied by several researchers [Dum98, Hon12, Jon81, Kub55, Mur81, Mur87, Ohn00, Oka96, Ros52, Thy52, Wan91]. In the pure binary iron-titanium system, the following phases are present as shown in the phase diagram by Murray (Figure 2.8) [Mur81]:

- 1) Liquid.
- 2) Alpha solid solution with a HCP structure. The maximum solubility of iron in alpha titanium is less than 0.05 at.% (0.043 wt.%).
- 3) Beta solid solution: this could be both beta titanium (pure and solid solution) and alpha iron (pure and sold solution) as both have a BCC structure.

- 4) Gamma solid solution with a FCC structure. The maximum solubility of titanium in the gamma solid solution is 0.8 at.% (0.69 wt.%) at about 1423 K (1150°C).
- 5) Equiatomic compound: FeTi forms from the melt in a peritectic reaction at 1590 K (1317°C) with a composition 47.5-50.3 at.% (51.35-54.14 wt.%) iron.
- 6)  $\text{TiFe}_2$ : it melts at 1700 K (1427°C) with a composition range of 64.5-72.4 at.% (60.9-69.2 wt.%) titanium.

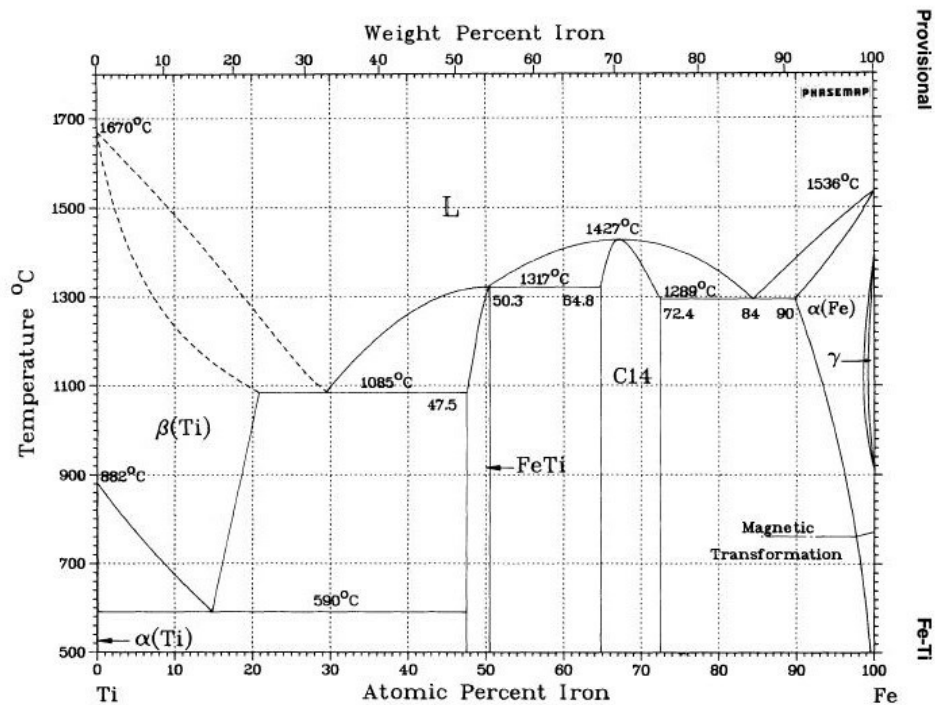


Figure 2.8: Iron-titanium binary phase diagram [Mur81].

Other than the above mentioned phases, two additional intermetallic phases have been previously reported in the literature. The controversial  $\text{Ti}_3\text{Fe}$  phase was reported, but later studies showed that this phase is due to contamination with aluminum and silicon. Similarly  $\text{Ti}_2\text{Fe}$  was also reported, but it is believed that this may be a ternary oxide phase. [Mur81]

Thyne et al. in 1952 [Thy52] did not report the  $Ti_2Fe$  phase in a binary iron-titanium system and concluded that  $Ti_2Fe$  reported in earlier literature may be an oxide phase. However, they reported that the melting point of pure titanium is 1993 K (1720°C), which contradicts Murray's phase diagram which shows the melting point to be 1943 K (1670°C). Similarly, there is a slight variation in the maximum solubility of iron in alpha titanium. Rostoker et al. [Ros52] prepared and characterized samples of  $Ti_2Fe$ ,  $Ti_3Fe_3O$  and  $Ti_4Fe_2O$ . The diffraction results for  $Ti_2Fe$  showed mainly the structure of  $TiFe$  phase along with some additional lines for alpha and beta titanium, indicating that the  $Ti_2Fe$  phase does not exist. However, the other two oxides yielded single phase patterns, which were identical to the  $Ti_2Fe$  patterns reported in previous literature. This again confirmed that  $Ti_2Fe$  is an oxide phase.

Initial studies also indicated that  $FeTi$  melts at a temperature above 1723 K (1500°C); however, Murray [Mur81] indicated a melting temperature for  $FeTi$  of around 1590 K (1317°C). It is, thus, argued that the higher melting temperature reported earlier was due to impurities. Jonsson [Jon81] assessed the phase diagram of iron-titanium binary system and, according to him, Murray did not take into account several phase boundaries involving the  $FeTi$  intermetallic compound. In an assessment of the iron-titanium system by Dumitrescu et al. [Dum98], emphasis is placed on the fact that all the assessments done on the iron-titanium binary system have certain discrepancies. More experimental work is required on 1) the width of the  $Fe_2Ti$  phase field, 2) the activity of titanium in the iron-rich liquid phase and BCC iron and 3) the eutectoid composition of beta titanium.

In the iron-titanium system the only phase that has a melting temperature higher than the steelmaking temperature is pure titanium (the melting temperature is 1943 K (1670°C)). It should

be kept in mind that the melting temperature of titanium decreases with the addition of iron in the form of a solid solution.

#### **2.4.7. Iron-Niobium-Aluminum System**

Since aluminum is the proposed addition to the ferroniobium alloy, it is necessary to discuss already available data for the ternary system (iron-niobium-aluminum). The initial study on the system was done by Raman in 1966 [Ram66(2)]. He studied the system at 1273 K (1000°C) and determined that the  $\text{Fe}_2\text{Nb}$  intermetallic phase extends in the direction of iron-aluminum system. Later Raghavan [Rag87] studied the system and found that the maximum solubility of aluminum in  $\text{Fe}_2\text{Nb}$  is 56 at.%. According to Bejarano in 1993 [Bej93(2)], an in-situ composite of the  $(\text{FeAl})_2\text{Nb}$  intermetallic and (FeAl) phase (eutectic) can be formed by using suitable amounts of iron, niobium and aluminum, where (FeAl) is the aluminum solid solution in iron. He also confirmed that  $\text{Fe}_2\text{Nb}$  and (FeAl) both dissolve almost 50 at.% aluminum by substituting iron atoms with the aluminum atoms. Thus, he suggested that a eutectic valley path would be followed by the ternary diagram (superimposed in Figure 2.9):

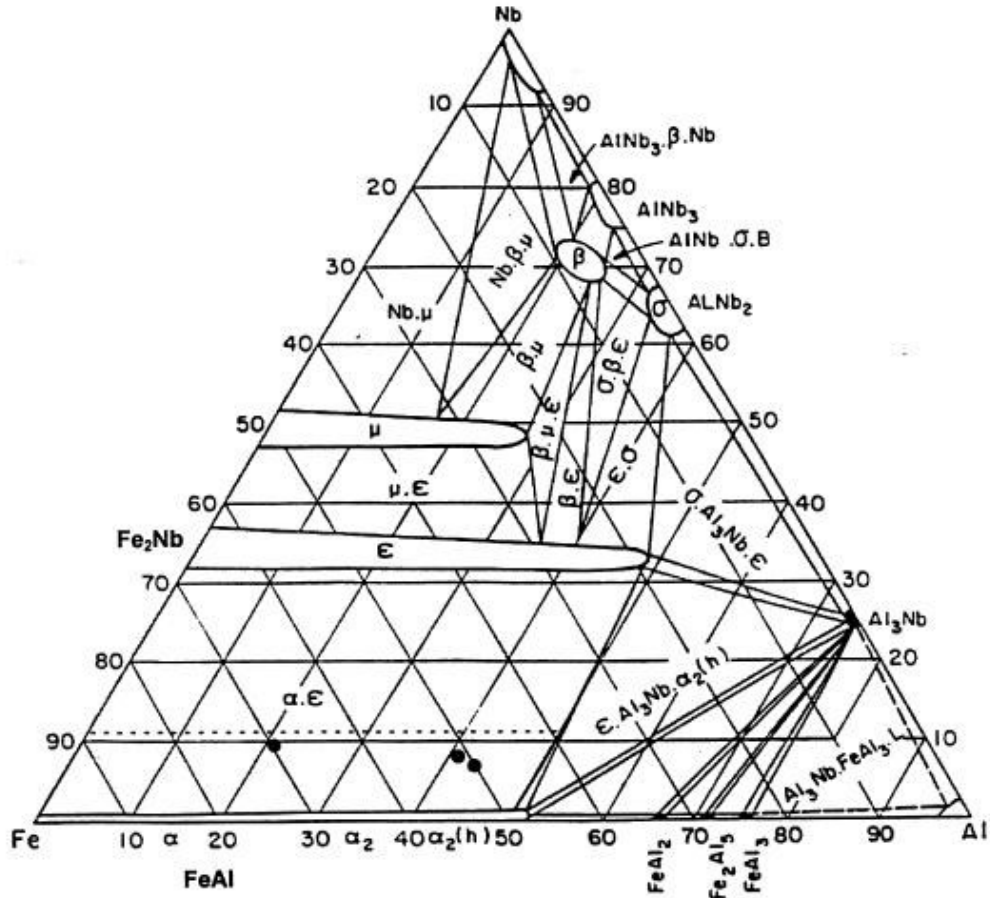


Figure 2.9: Isothermal cross-section for the iron-aluminum-niobium ternary system at 1273 K (1000°C) [Bej93(2)].

Mota et al. [Mot99] studied directional growth in iron-niobium-aluminum eutectic alloys with varying aluminum content, *i.e.*, 20 to 50 at.% (4.3 to 15.4 wt.%) and observed that with higher aluminum content around 41.2 at.% (11.28 wt.%) an additional phase,  $\text{Al}_3\text{Nb}$ , was observed. According to authors, a eutectic microstructure is achieved with a composition of  $\text{Fe}_{49.5}\text{Al}_{41.2}\text{Nb}_{9.1}$ . Morris et al. [Mor06] prepared and examined age hardening of iron-aluminum-niobium alloys with 15 to 30 at.% aluminum, 5 at.% and 2 at.% niobium (7.8 to 16.9 wt.% aluminum with 3.6 to 3.9

wt.% niobium and 7.6 to 16.5 wt.% aluminum with 8.7 to 9.4 wt.% niobium) and the balance iron. Martin Palm [Pal09] studied the iron-rich portion of iron-niobium-aluminum system in which the niobium content was 5 at.% and 10 at.% (5.6 wt.% to 11.1 wt.%). The microstructure of the as cast material was primary alpha (iron, aluminum) solid solution surrounded by a eutectic mixture of alpha (iron, aluminum) solid solution plus the Laves phase. By heating the material at 1073 K (800°C) for 1000 hrs, the eutectic coarsened and small precipitates of Laves phase formed within the primary alpha solid solution because of its apparent super saturation. Annealing at 1273 K (1000°C) and 1423 K (1150°C) resulted in the disappearance of the eutectic portion.

## **2.5. Summary**

The presence of coarse niobium- and titanium-rich particles in microalloyed steel can have a negative effect on the mechanical properties, by acting as crack initiation sites. Two school of thoughts exists on the origin of these coarse particles: 1) They form by nucleating at high temperatures (in molten steel) as a result of segregation and 2) they are undissolved, high melting temperature phases present in their respective ferroalloys. Several binary iron-niobium and iron-titanium phase diagrams are available in the literature. Since the alloys under study contain impurities, identification of high melting temperature phases in the ferroalloys is required, along with comparison with the phase diagrams available in the literature. Once the high melting temperature phases are identified (in ferroniobium), a comparison of such phases with the coarse niobium-rich particles is required in order to identify the origin of such particles. Lastly, a methodology is devised for elimination of high melting temperature phase(s) in the ferroniobium alloy.

## 2.6. References

Abr06(1): S. Abraham, R. Klein, R. Bodnar and O. Dremailova. Formation of coarse particles in steel as related to ferroalloy dissolution thermodynamics. Part 1: ferroalloy melting, dissolution and microstructures. Material Science and Technology (MS & T), Cincinnati, Ohio, October 2006.

Abr06(2): S. Abraham, R. Klein, R. Bodnar and O. Dremailova. Formation of coarse particles in steel as related to ferroalloy dissolution thermodynamics. Part II: crystallographic study of ferroalloys and coarse particles. Material Science and Technology (MS & T), Cincinnati, Ohio, October 2006.

Arg82: S. A. Argyropoulos, R. I. L. Guthrie. Dissolution kinetics of ferroalloys in steel making. 65<sup>th</sup> steel making conference proceedings: Pittsburgh, March 28-31, 1982.

Arg84: S. A. Argyropoulos. The effect of microexothermicity and macroexothermicity on the dissolution of ferroalloys in liquid steel. Electric Furnace Conference Proceedings, the Iron and Steel Society/AIME, 1984.

Bej91: J. M. Z. Bejarano, S. Gama, C. A. Ribeiro, G. Effenberg and C. Santos. On the existence of the Fe<sub>2</sub>Nb<sub>3</sub> phase in the Fe-Nb system Zeitschrift für Metallkunde, 1991, 82, 615–620.

Bej93(1): J. M. Z. Bejarano, S. Gama, C. A. Ribeiro and G. Effenberg. The iron-niobium phase diagram. Zeitschrift für Metallkunde, 1993, 84, 3, 160–164.

Bej93(2): J. M. Z. Bejarano. Investigation of the ternary diagram iron-aluminum-niobium. Ph.D. thesis, Department of Materials Engineering, Universidade Estadual de Campinas, Brazil, 1993.

Cal07: William D. Callister Jr. Materials Science and Engineering, An Introduction. John Wiley and Sons Inc., 2007.

Che87: Z. Chen, M. H. Loretto and R. C. Cochrane. Nature of large precipitates in titanium containing HSLA Steels. *Materials Science and Technology*, 1987, 3, 836-844.

Cos92: G. J. R. Costa. Niobium ferroalloy and niobium additive for steels, cast irons and other metallic alloys. Patent WO/1992/022675.

Cra00: A. J. Craven, K. He, L. A. J. Garvie and T. N. Baker. Complex heterogeneous precipitation in titanium-niobium microalloyed Al-killed HSLA steels-II. Non-Titanium based precipitates. *Acta Materialia*, 2000, 48, 3869-3878.

Dav01: J. R. Davis (Editor). *Alloying: Understanding the Basics*. ASM International, 2001.

Dum98: L. F. S. Dumitrescu, M. Hillert and N. Saunders. Comparison of Fe-Ti assessments. *Journal of Phase Equilibria*, 1998, 19, 5, 441-448.

Eng92: T. A. Engh. *Principles of Metal Refining*. Oxford University Press, 1992.

Gas13: Michael M. Gasik (Editor). *Handbook of Ferroalloys: Theory and Technology*. Oxford: Elsevier Science, 2013.

Gei73: G. H. Geiger and D. R. Poirer. *Transport Phenomena in Metallurgy*. Addison-Wesley, 1973.

Gla97: T. Gladman. *The Physical Metallurgy of Microalloyed Steels*. The Institute of Materials, London, 1997.

Gol57: H. J. Goldschmidt. New intermediate phases in the iron-niobium system. *Research*, 1957, 10, 289-291.

Gou84: L. Gourtsoyannis, R. I. L. Guthrie and G. A. Ratz. The dissolution of ferromolybdenum, ferroniobium and rare earth (Lanthanide) silicide in cast iron and steel melts. Electric Furnace Conference Proceedings, the Iron and Steel Society/AIME, 1984.

Hon12: B. Hong, W. Jiang, L. Duarte, C. Leinenbach, L. Li-bin, L. Hua-shan and J Zhan-peng. Thermodynamic re-assessment of Fe-Ti binary system. Transactions of Non-Ferrous Metals Society of China, 2012, 22, 2204-2211.

Ich89: E. Ichise and K. Horikawa. Thermodynamic study of Fe-Ta and Fe-Nb alloys by means of the Knudsen Cell Mass Spectrometry. ISIJ International, 1989, 29, 10, 843-851.

Jon81: S. Jonsson. Assessment of the Fe-Ti System. Metallurgical and Materials Transactions B, 1981, 29B, 361-370.

Kri68: P. I. Kripyakevitch, E. I. Gladyshevskii and R. V. Skolozdra. Soviet Physics, Crystallography, 12 (1968) 525.

Kub55: O. Kubaschewski and W. A. Dench. The heats of formation in the systems titanium-aluminum and titanium-iron. Acta Metallurgica, 1955, 3, 339-346.

Kub82: O. Kubaschewski. Iron Binary Phase Diagrams. Springer-Verlag, Berlin, 1982.

Loz07: E. Yu. Lozovaya, V. I. Zhuchkov and O. Yu. Sheshukov. Determination of melting time of an Fe-Al ferroalloy in an Iron-Carbon Melt. Russian Metallurgy (Metally), 2007, 7, 601-602.

Lu84: F. X. Lu and K. H. Jack. The occurrence of high speed steel carbide type  $\eta$  phases in the Fe-Nb system. Journal of Less Common Metals, 1985, 14, 123-127.

- Men99: R. Mendoza, J. Huante, M. Alanis, C. Gonzalez-Rivera and J. A. Juarez-Islas. Slab cracking after continuous casting of API 5L X-70 grade steel for pipeline sour gas application. *Iron and Steelmaking*, 1999, 26, 3, 205-209.
- Mor06: D. G. Morris, M. A. Munoz-Morris, L. M. Requejo and C. Baudin. Strengthening at high temperatures by precipitates in Fe-Nb-Al alloys. *Intermetallics*, 2006, 14, 1204-1207.
- Mot99: M. A. Mota, A. A. Coelho, J. M. Z. Bejarano, S. Gama and R. Caram. Directional growth and characterization of Fe-Al-Nb eutectic alloys. *Journal of Crystal Growth*, 1999, 198/199, 850-855.
- Mur81: J. L. Murray. The Fe-Ti (Iron-Titanium) system. *Bulletin of Alloy Phase Diagrams*, 1981, 2, 3, 320-334.
- Mur87: J. L. Murray (Editor). *Phase Diagrams of Binary Titanium Alloys*. ASM International, Metals Park, OH, 1987.
- Ohn00 I. Ohnuma, Y. Fujita, H. Mitsui, K. Ishikawa, R. Kainuma and K. Ishida. Phase equilibria in the Ti-Al binary system. *Acta Materialia*, 2000, 48, 3113-3123.
- Oka93: H. Okamoto. Fe-Nb (Iron-Niobium). *Journal of Phase Equilibria*, 1993, 14, 5, 650-652.
- Oka95: H. Okamoto. Comment on Fe-Nb (Iron-Niobium). *Journal of Phase Equilibria*, 1995, 16, 4, 369-370.
- Oka96: H. Okamoto. Fe-Ti (iron-titanium). *Journal of Phase Equilibria*, 1996, 17, 4, 369.
- Oka02: H. Okamoto. Fe-Nb (Iron-Niobium) supplementary literature review. *Journal of Phase Equilibria*, 2002, 23, 1, 112.

Pal09: M. Palm. Phase equilibria in the Fe corner of the Fe-Al-Nb system between 800 to 1150°C. *Journal of Alloys and Compounds*, 2009, 475, 173-177.

Pau86: E. Paul and L. J. Swartzendruber. The Fe-Nb (Iron-Niobium) system. *Bulletin of Alloy Phase Diagrams*, 1986, 7, 3, 248-254.

Por92: D. A. Porter and K. E. Easterling. *Phase Transformations in Metals and Alloys*. Chapman and Hall, London, 1992.

Pot01: R. M. Poths, R. L. Higginson and E. J. Palmiere. Complex precipitation behaviour in a microalloyed plate steel. *Scripta Materialia*, 2001, 44, 147-151.

Rag87: V. Raghavan. The Al-Fe-Nb (Aluminum-Iron-Niobium) system, phase diagrams of ternary iron alloys. Part 1, ASM International, Materials Park, OH, 1987.

Ram66(1): A. Raman. The  $\mu$  phase. *Zeitschrift für Metallkunde*, 1966, 57, 301-305.

Ram66(2): A. Raman. X-ray investigations of some T-T<sup>5</sup>-Al systems. *Zeitschrift für Metallkunde*. 1966, 57, 7, 535-540 (In German)

Ram67: A. Raman. Structural study of niobium-iron alloys. *Proceedings of the Indian Academy of Sciences-Section A*, 1967, 65, 4, 256-264.

Rap94: M. T. Raposo, J. D. Ardisson, A. I. S. Pesiano and R. A. Mansur. Characterization of phases in the Fe-Nb system. *Hyperfine Interactions*, 1994, 83, 235-238.

Rob84: W. Roberts. Recent innovations in alloy design and processing of microalloyed steels. *Conference Proceedings of International Conference on Technology and Applications of HSLA Steels*, Philadelphia, 3-6 October, 1983, American Society of Metals 1984.

Ros52: W. Rostoker. Observation on the occurrence of  $Ti_2X$  phases. *Journal of Metals*, 1952, 2, 209-210.

Sch96: C. G. Schon and J. A. S. Tenorio. The chemistry of iron-niobium intermetallics. *Intermetallics*, 1996, 4, 211-216.

Sou01: C. A. de F. Sousa. The evolution of FeNb manufacturing. In *Niobium, Science and Technology*; Minerals, Metals and Materials Society: Orlando, FL, United states, 2001.

Sri94: S. Srikanth and A. Petric. A thermodynamic evaluation of the Fe-Nb system. *Zeitschrift für Metallkunde*, 1994, 85, 3, 164–170.

Thy52: R. J. Van Thyne, H. D. Kessler and M. Hansen. The systems titanium-chromium and titanium-iron. *Transactions of the ASM*, 1952, 44, 974-989.

Tia07: Q. Tian, Y. Chen, J. Chen, G. Xu and Y. Zheng. Characterization of Nb-rich phase precipitation near internal cracks in continuously cast slabs. *Minerals, Metals and Materials Society (TMS)*, Warrendale, PA, 15086-7528, USA: 2007.

Vob11: S. Vob, M. Palm, F. Stein and D. Raabe. Phase equilibria in the Fe-Nb system. *Journal of Phase Equilibria and Diffusion*, 2011, 32, 97–104.

Wan91: H. Wang, R. Lueck and B. Predel. Calorimetric determination of the enthalpy of mixing of liquid iron-titanium alloys. *Zeitschrift für Metallkunde*, 1991, 82, 8, 659–665.

Wet69: K. Wetzig. Investigations of intermetallic compounds in the binary systems Nb-Fe and Ta-Co by means of an emission electron microscope. *Physica Status Solidi (b)*, 1969, 34, 2, K79-K81.

Yua09: S. Q. Yuan and G. L. Liang. Dissolving behaviour of second phase particles in Nb-Ti microalloyed steel. *Materials Letters*, 2009, 63, 2324-2326.

Zho96: C. Zhou and R. Priestner. The evolution of precipitates in Nb-Ti microalloyed steels during solidification and post-solidification cooling. *ISIJ International*, 1996, 36, 11, 1397-1405.

Zhu07: X. Zhuo, X. Wang, W. Wang and H. G. Lee. Nature of large (Ti, Nb)(C, N) particles precipitated during the solidification of Ti, Nb HSLA steel. *Journal of University of Science and Technology Beijing: Mineral Metallurgy Materials (Eng Ed)*, 2007, 14, 2, 112-117.

Zhu08: X. Zhuo, D. Woo, X. Wang and H. Lee. Formation and thermal stability of large precipitates and oxides in titanium and niobium microalloyed steel. *Journal of Iron and Steel Research International*, 2008, 15, 3, 70-77.

## Chapter 3: Experimental Procedures

### 3.1. Outline of Experimental Procedures

The experimental procedures of this thesis are divided into two parts. Experimental procedures related to Chapters 4 and 5 are discussed in part 1. Experimental procedures for Chapters 6 and 7 are discussed in Part 2.

Part 1: Characterization of as-received ferroniobium and ferrotitanium alloys.

This includes the use of the following tools: composition analysis by inductively coupled plasma (ICP) spectroscopy and direct current plasma atomic emission spectroscopy methods and microstructural study using scanning electron microscopy (SEM), transmission electron microscopy (TEM) and X-ray diffraction (XRD). In addition, differential scanning calorimetry (DSC) was used to study the liquidus temperature and solidification behavior of as-received ferroalloys.

Part 2: Development of new ternary alloys is described in two subsections.

- i) Modification of the chemistry of the as-received ferroniobium alloy in order to eliminate the high melting temperature phases, followed by characterization. This involves addition of aluminum to the as-received ferroniobium alloy using an induction melting unit. The new alloy is characterized with the help of SEM and TEM in order to identify the phases formed.
- ii) The second step studies the effect of aluminum on the liquidus temperature of the ferroniobium alloy. This takes into account preparing different compositions, by arc

melting ternary master alloys using pure iron, niobium and aluminum. These master alloys are then subjected to DSC to study the liquidus temperature.

### **3.2. Composition Analysis**

Evraz Inc. NA, provided samples of as-received ferroniobium and ferrotitanium alloys. The composition of the two ferroalloys was provided by the supplier. Samples of the as-received ferroalloys were sent to Cambridge Scientific for chemical analysis in order to verify their composition. Chemical analysis was performed by Cambridge Scientific according to ASTM E1097-07 (modified) and E1479-99 (2005) using ICP spectroscopy and direct current plasma atomic emission spectroscopy analysis. Only iron and titanium compositions in ferrotitanium and iron and niobium compositions in ferroniobium were analyzed by Cambridge Scientific. The results of chemical analysis are compared in the next chapter.

### **3.3. Scanning Electron Microscopy (SEM)**

Most of the microstructural analysis was done using SEM. Sample preparation for SEM was done using conventional metallographic techniques. Samples were cut, using an automatic diamond cutter and then mounted using cold mounting techniques. SiC papers were used for grinding purposes, with a continual increase in grit up to 1500. Final polishing was done using 1  $\mu\text{m}$  diamond paste. Most of the grinding and polishing was done manually; however, some was done using an automated polishing unit. After polishing the samples were ultrasonically cleaned in ethanol. Microstructural analysis of as-received ferroniobium, ferrotitanium and newly formed ternary alloys was done using different SEMs.

A Hitachi S-2700 SEM, equipped with a PGT (Princeton Gamma-Tech) IMIX digital imaging system and operated at 20 kV, was used. The SEM was equipped with an Everhart-Thornley (E-T) type secondary electron (SE) detector and a four quadrant solid state backscattered electron (BSE) detector. For energy dispersive X-ray (EDX) spectroscopy, the SEM was equipped with a PGT PRISM IG (intrinsic germanium) detector with an energy resolution of 114 eV. A VEGA-3 (Tescan) SEM operated at 20 kV, with an E-T type SE detector and a scintillation type BSE detector, was also used for microstructural analysis. The VEGA-3 (Tescan) SEM was equipped with an INCAx-act silicon drift detector (SDD) (Oxford Instruments) for X-ray microanalysis. This detector has an energy resolution of 133 eV. For higher resolution SE and BSE images a third SEM, a Zeiss EVO MA 15 LaB<sub>6</sub> filament SEM, was used at an operating voltage of 20 kV. It was equipped with an E-T SE detector and a silicon diode BSE detector. For EDX analysis, the SEM was equipped with a Peltier-cooled 10 mm<sup>2</sup> Bruker Quantax 200 SDD with an energy resolution of 123 eV. A Cameca SX100 electron probe with five wavelength energy spectrometers was used for wavelength dispersive X-ray (WDX) spectroscopy. The accelerating voltage and probe current were 20 kV and 20 nA respectively. The PAP correction procedure [Pou85] was used for data reduction. For Auger analysis a JAMP-9500F Auger microprobe was used. In order to remove any contamination, samples were cleaned and etched before Auger analysis. Ar<sup>+</sup> ion etching was done using an emission current of 20 mA, an accelerating voltage of 2000 V at a sputtering rate of 15 nm/min (calibrated by SiO<sub>2</sub>) for a period of 30 s. For SEM and Auger imaging, an accelerating voltage of 15 kV and an emission current of 8 nA were used. The electron probe had a diameter of 2 to 8 nm and was produced by a Schottky field emitter. A working distance of 24 mm was used and the sample was rotated 30° away from the primary electron beam. The energy resolution of the M5 lens used for Auger spectroscopy and imaging was 0.6%.

The phase fraction of different samples was calculated using ImageJ and FIJI software [Abr04]. At least five representative microstructures (BSE images) from each sample were taken at low magnifications (50X to 150X) and the phase fraction was reported on the basis of an average calculated value. Image enhancement tools in ImageJ and FIJI software were used to clearly distinguish between different phases. The phase fraction of different phases was calculated by randomly imposing a square grid that contained equally spaced points formed as a result of intersection of horizontal and vertical straight lines, on the image. The basic concept is that the volume fraction of a phase/region/area of interest is equal to the statistical probability of finding randomly placed point(s) in that region/phase/area of interest [Deh68]. Each point laying within a phase was counted as one and any point lying on the boundary of two phases was considered as one-half for each phase. The volume fraction was calculated using the following equation:

$$V_v = \frac{N_p + 0.5N_b}{N} \quad \text{Equation 3.1}$$

where  $N_p$ ,  $N_b$  and  $N$  are the number of points laying on the phase, the number of points laying on the boundary of two phases and the total points, respectively. The standard deviation was calculated using Equation 3.2.

$$S = \sqrt{\frac{1}{N-1} \sum_{i=1}^N (V_{v(i)} - \bar{V}_v)^2} \quad \text{Equation 3.2}$$

where  $S$  is the standard deviation and  $\bar{V}_v$  is the average of the volume fractions, *i.e.* the average of  $V_{v(i)}$ .

### 3.4. Transmission Electron Microscopy (TEM)

A Hitachi NB5000 dual beam focused ion beam-scanning electron microscope (FIB-SEM) was used to prepare TEM samples from the regions of interest. The three main steps involved in TEM sample preparation through FIB-SEM were sectioning, thinning and polishing. Gallium ions were used for these three steps. For sectioning, a gallium ion beam with a large beam current between 20 nA and 60 nA was used. Then the sectioned sample was mounted on a copper grid. Lower beam currents (0.7 nA to 4 nA) were then used for thinning, followed by polishing using very low beam currents ( $< 0.1$  nA). The purpose was to make the sample electron transparent for TEM analysis by decreasing the thickness of the sample to about 100 nm. Once the desired thickness was achieved the sample was then viewed using a JEOL JEM-2010 TEM. The TEM was equipped with a Noran ZMAX30 Si-Li EDX detector and was operated at 200 kV. Figure 3.1 shows the steps involved in preparing a TEM sample with a FIB.

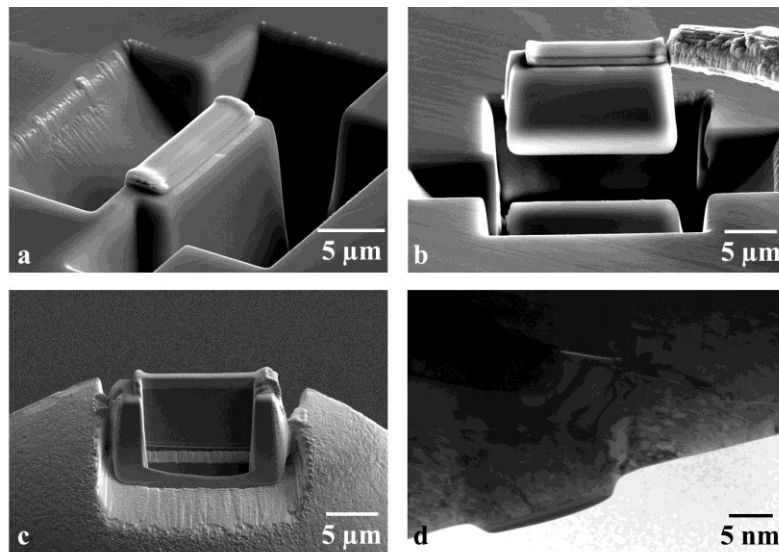


Figure 3.1: Steps involved in TEM sample preparation using a FIB: a) sectioned area of interest; b) FIB probe welded to the lamella which is then plucked out; c) sample placed on a copper grid for thinning; d) final prepared sample as imaged in the TEM.

Selected area diffraction (SAD) patterns, EDX spectra, bright field (BF) images and dark field (DF) images were collected from selected regions. A standardless approach was taken for EDX analysis; therefore, the compositions determined are approximate. For indexing selected area diffraction patterns, a camera constant was determined using silicon. This camera constant was then used in the following equation to calculate the d-spacing for diffracted planes. [Wil96]

$$(R'')(d') = (\lambda)(L) \quad \text{Equation 3.3}$$

where  $R''$  is distance between the central undiffracted spot and a specific diffracted spot measured from the SAD pattern (Figure 3.2),  $L$  is the camera length for the TEM, *i.e.*, the effective distance between specimen and the camera,  $\lambda$  is the wavelength of the electrons and  $d'$  is the d-spacing for the plane of interest.

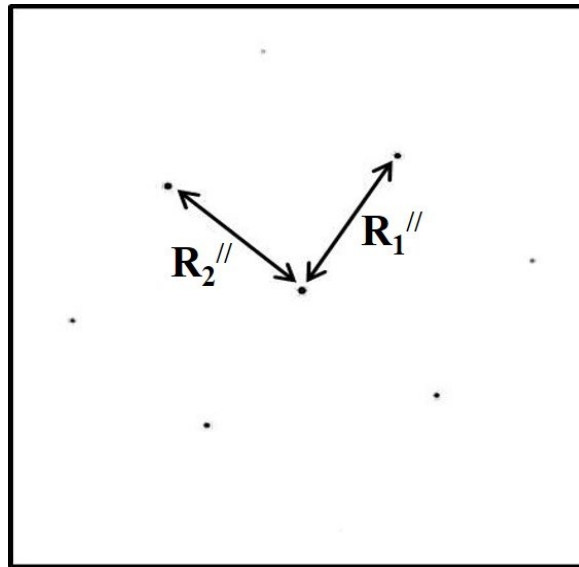


Figure 3.2: An example of the measurement of  $R''$  values from an SAD pattern.

The product of  $\lambda$  and  $L$ , *i.e.*,  $(\lambda)L$  is called the camera constant. The value of  $\lambda$  can fluctuate some due to electronic instabilities. Therefore, for better accuracy, the camera constant is used rather than  $\lambda$  and  $L$  separately. The d-spacing calculated from Equation 3.3 was then used to determine the (hkl) planes.

### **3.5. X-ray Diffraction (XRD)**

Sample preparation for XRD analysis was done by polishing one side of the surface using SiC papers. The starting paper was 120 grit with a gradual increase to a maximum of 1200 grit. The samples were then subjected to ultrasonic cleaning in ethanol solution. A Rigaku rotating anode (RU-200B) XRD system with a copper anode was used for XRD analysis. The system was operated at 100 mA and 40 kV with a continuous mode of operation and a scan speed of 2°/min. The data achieved was analyzed using Jade-7 software. Each pattern was indexed manually using the crystallographic information ( $2\theta$ , relative intensities and d-spacing values) of possible phases involved.

### **3.6. Differential Scanning Calorimetry (DSC)**

For phase transformations and liquidus temperature determination, a Setaram Labsys Evo 1600 differential scanning calorimeter was used. Four to five different standards (pure metals: zinc, aluminum, silver, gold and nickel) with melting temperatures in the range of 573 K-1773 K (300-1500°C) were used to calibrate the machine. Solid samples were heated and cooled in inert argon or helium atmosphere in alumina crucibles. For homogenization purposes, samples were kept at

elevated temperature for 15 minutes. In order to account for the effects of undercooling and superheating, different cooling and heating rates of 10, 20 and 50 K/min were used.

### 3.7. Induction Melting

The as-received ferroniobium alloy was melted with pure aluminum (99.9 wt.% aluminum) in a high frequency induction melting unit to fabricate ternary niobium-iron-aluminum alloys. Different amounts of aluminum were added, varying from 5-15 wt.%. Fully fired  $ZrO_2$  crucibles were used for melting. These zirconia crucibles were surrounded by graphite crucibles. The gap between the two crucibles was filled with graphite powder acting as a susceptor. The temperature of the system was continuously monitored using C-type thermocouples, inserted within the melt inside the  $ZrO_2$  crucible. The total melt weight inside the crucible was usually less than 800 g (depending on the amount of aluminum added). The graphite crucibles containing the  $ZrO_2$  crucibles were placed inside water-cooled copper coils connected to the generator. A schematic diagram showing this setup is shown in Figure 3.3.

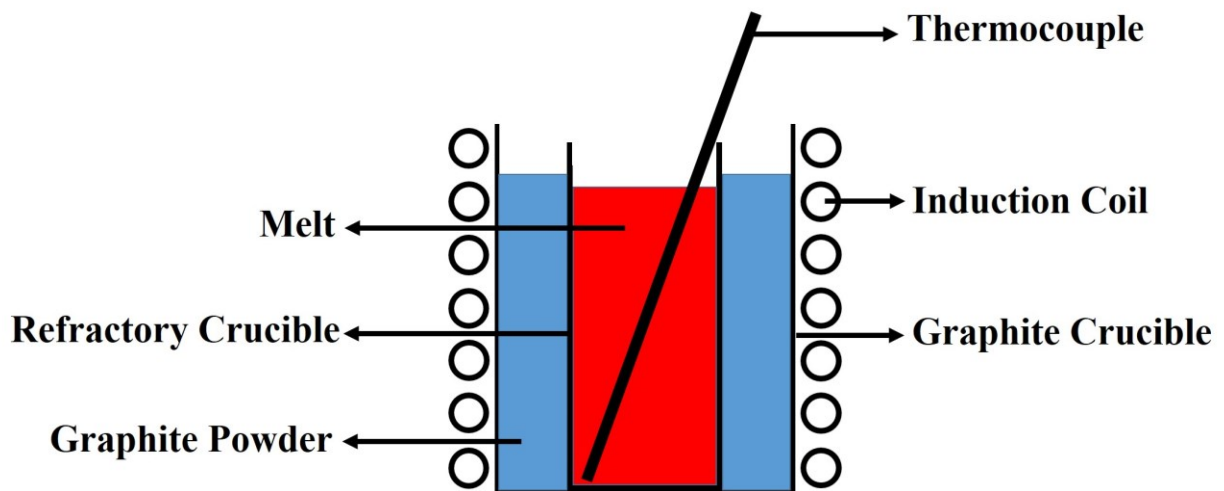


Figure 3.3: Schematic diagram showing the experimental setup for induction melting.

The complete melting practice was done in an inert atmosphere of argon gas. The chamber, once closed and sealed, was evacuated and then filled with argon gas. The oxygen level inside the chamber was measured with an oxygen sensor. If the oxygen level was around 1000 ppm, then another cycle of evacuation and argon gas purging followed; in addition, the chamber was checked for any possible leak(s). After the second purge, the oxygen level was usually reduced to less than 500 ppm. At this stage the chamber was continuously purged with argon gas for some period of time until the oxygen level was reduced to less than 20 ppm. The samples were then heated gradually to a maximum temperature between 2023 K and 2123 K (1750°C and 1850°C) under a positive argon pressure. After maintaining the melt at high temperature for a considerable period of time (between 40 and 75 minutes), the melt was then cooled slowly by decreasing the power of the generator. Finally, the power was switched off and the melt was allowed to cool inside the furnace to room temperature.

In another set of experiments the steel samples was heated to 1873 K (1600°C) using induction furnace in a positive argon pressure. Instead of using  $ZrO_2$  crucibles, fully fired  $Al_2O_3$  crucibles were used for melting. The rest of the setup was same as described earlier. The steel samples were then kept at that temperature for 15-20 minutes for homogenization. After homogenization as-received ferroniobium was added to molten steel samples using glove box. Different dissolution times were given (ranging from 6 minutes to 40 minutes) for ferroniobium dissolution in molten steel. The samples were then cooled by slowly decreasing power and cooling the sample to room temperatures.

### 3.8. Arc Melting

A very important study was to observe the effect of aluminum additions on the liquidus temperature of the as-received ferroniobium alloy. For this purpose, master alloys of similar compositions to the induction melted alloys were made with pure aluminum (99.999 wt.%), iron (99.95 wt.%) and niobium (99.95 wt.%) using a compact MAM-1 arc melter\* (non-consumable tungsten electrode). A powerful arc melted generator was preinstalled and integrated in the housing. The connection parameters were as follows: voltage: 230V, frequency: 50/60 Hz and 1-phase. The arc melter can go up to a maximum temperature of 3773 K (3500°C). Required weights of aluminum, iron and niobium were placed together on a water-cooled copper plate. An aluminum or titanium pellet was also placed alongside the metals to be melted. This metal pellet was used as an oxygen getter. The small chamber was then closed and sealed. The chamber was evacuated and then purged with argon gas. This practice was done three times before melting could begin. A tungsten electrode was used to generate the spark for melting purposes. Initially the aluminum/titanium metal was melted in order to react with any oxygen present in the chamber. Afterwards aluminum, niobium and iron were melted together using the same tungsten electrode. Once the sample was cooled, the chamber was opened and the sample was inverted to melt the other side to improve homogeneity. The same procedure was followed for evacuation, purging and melting. The sample was then inverted for a second time and melted again.

---

\* *Professor Arthur Mar Laboratory, Department of Chemistry, University of Alberta.*

### 3.9. References

Abr04: M. D. Abramoff, P. J. Magalhaes and S. J. Ram. Image processing with ImageJ. *Biophotonics International*, 2004, 11, 7, 36-42.

Deh68: R. T. Dehoff and F. N. Rhines. *Quantitative Microscopy*. McGraw-Hill Book Company, New York, 1968.

Pou85: J. L. Pouchou and F. Pichoir. "PAP" ( $\Phi$ - $\rho$ - $Z$ ) procedure for improved quantitative microanalysis. In: Armstrong JT, Editor. *Microbeam Analysis*. California: San Francisco Press, 1985.

Sha13(1): S. J. Shah, H. Henein and D. G. Ivey. Microstructural characterization of ferrotitanium and ferroniobium. *Materials Characterization*, 2013, 78, 96-107.

Sha13(2): S. J. A. Shah, H. Henein and D. G. Ivey. Microstructural evolution and characterization of a ferroniobium alloy. *Emerging Materials Research*, 2013, 2, EMR2, 79-89.

Wil96: D. B. Williams and C. B. Carter, *Transmission Electron Microscopy: A Textbook for Materials Science*, Plenum Press, 1996.

## Chapter 4: Microstructural Characterization of Ferrotitanium and Ferroniobium<sup>1</sup>

### 4.1. Introduction

Microalloyed steels are manufactured by the addition of small amounts of niobium, titanium, vanadium and molybdenum. These alloying elements are added in the form of their respective ferroalloys. Generally ferroalloys are classified into two categories; ferroalloys with melting points lower than steelmaking temperatures and ferroalloys with melting points higher than steelmaking process temperatures [Eng92]. Ferroalloys with melting points higher than the temperatures experienced during steelmaking do not melt; they dissolve as a result of a composition gradient between the ferroalloy and the molten steel and by liquid phase mass transfer [Gou84]. Commercial grade ferroniobium (iron-niobium) is believed to have a liquidus temperature higher than steelmaking process temperatures; therefore, when added to the molten steel, ferroniobium dissolves rather than melts [Cos92]. Coarse titanium- and niobium-rich particles have been reported in some microalloyed steels, and these particles have a negative influence on the mechanical properties of the steel [Abr06(1), Abr06(2), Che87, Cra00, Men99, Pot01, Rob84, Yua09]. According to Mendoza et al. [Men99] and Abraham et al. [Abr06(1), Abr06(2)], the presence of coarse particles is associated with undissolved phases from their respective ferroalloys. Sunday et al. characterized commercial grades of ferrotitanium, ferromolybdenum and ferroniobium. They reported four phases in ferrotitanium and two phases in ferroniobium.

---

<sup>1</sup> Chapter 4 has been published as Shah et al. "Microstructural characterization of a ferrotitanium and ferroniobium. *Materials Characterization*. 2013, 78, 96-107. This chapter has excerpts from the paper.

According to the authors the undissolved phases in ferroniobium and ferrotitanium are a niobium-rich solid solution containing iron and a TiN intermetallic, respectively [Abr06(1), Abr06(2)].

In the current chapter, detailed characterization of commercial grade ferroniobium (iron-niobium) and ferrotitanium (iron-titanium) is carried out in order to identify all phases present and specifically those with melting points in excess of steelmaking temperatures. The characterization techniques utilized are scanning electron microscopy, transmission electron microscopy and X-ray diffraction.

## **4.2. Experimental Section**

The chemical compositions of the ferroalloys were verified by the chemical analysis performed at Cambridge Scientific and the methods are discussed in Section 3.2 of the thesis.

The microstructures of the as-received ferrotitanium and ferroniobium were investigated using a Hitachi S-2700 SEM and Zeiss EVO MA 15 LaB<sub>6</sub> filament SEM. WDX spectroscopy analysis was done using a Cameca SX100 electron microprobe. Data reduction was performed using the PAP correction procedure [Pou85]. SEM samples were prepared by conventional metallographic methods. The operating conditions for these instruments are discussed in Section 3.3 of this thesis.

TEM specimens were prepared using a Hitachi NB5000 dual beam FIB-SEM. Prepared samples were studied using A JEOL JEM-2010, equipped with an EDX detector, to obtain BF and DF images as well as SAD patterns and EDX spectra from localized regions. The details on the sample preparation procedure and the operating conditions of both instruments are discussed in Section 3.4.

XRD analysis was done on all samples using a Rigaku rotating anode (RU-200B) XRD system, with copper as the target anode. Sample preparation and operating conditions are discussed in Section 3.5 of the thesis.

### 4.3. Results and Discussion

Comparison of the results of chemical analysis of ferrotitanium and ferroniobium is shown in Table 4.1. There is good agreement between the nominal compositions and those determined by Cambridge Scientific.

Table 4.1: Chemical analysis of ferrotitanium and ferroniobium

Analysis method	Ferroalloys	Ti	Fe	Nb	Al	Si	V	N	C
Evraz, Inc. (wt.%)	Ferrotitanium	69.23	22.8	-	4.896	0.083	2.258	0.367	0.198
Cambridge Scientific (wt.%)*	Ferrotitanium	70.1	18.5	11.4					
Evraz, Inc. (wt.%)	Ferroniobium	0.57	30.7	65.5	1.4	1.4	-	-	0.1
Cambridge Scientific (wt.%)*	Ferroniobium		32.8	64.1	3.1				

\* These represent mean values from at least 2 samples.

### 4.3.1. Ferrotitanium (Iron-Titanium)

According to the equilibrium binary phase diagram for iron-titanium [Oka96], shown in Figure 4.1, the phases that should be present in this ferroalloy (dashed vertical line), based on the chemistry in Table 4.1, are the FeTi intermetallic and the titanium-rich solid solution ( $\alpha$ -titanium).

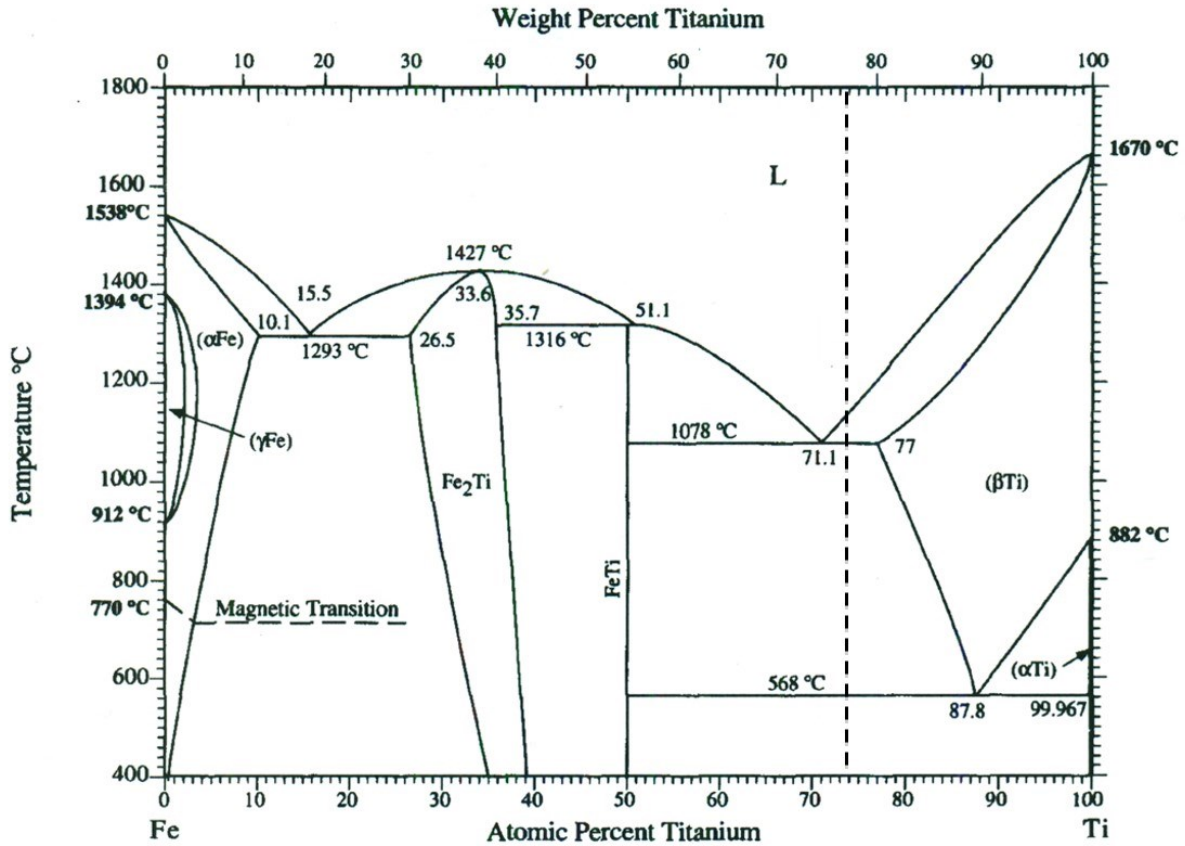


Figure 4.1: Iron-titanium binary phase diagram [Oka96]. The vertical line represents the ferrotitanium alloy composition (iron and titanium only).

XRD analysis was the first characterization method used to identify phases present in the as-received ferrotitanium (Figure 4.2). Not all the peaks in the diffraction pattern were indexed

successfully. In particular, two intense low angle peaks (at  $2\text{-theta} < 20^\circ$ ) could not be identified at this point; these peaks will be addressed later. Three phases were tentatively identified as  $\alpha$ -titanium,  $\beta$ -titanium and FeTi. It should be pointed out that there is a measurable difference between the d-spacings for the pure phases and those in the XRD pattern, which is not surprising due to the presence of impurities in the commercial ferroalloy (Table 4.1). In addition,  $\beta$ -titanium is not thermodynamically stable at room temperature (Figure 4.1); however, non-equilibrium phases are indeed possible in these commercial alloys as a result of the processing conditions.

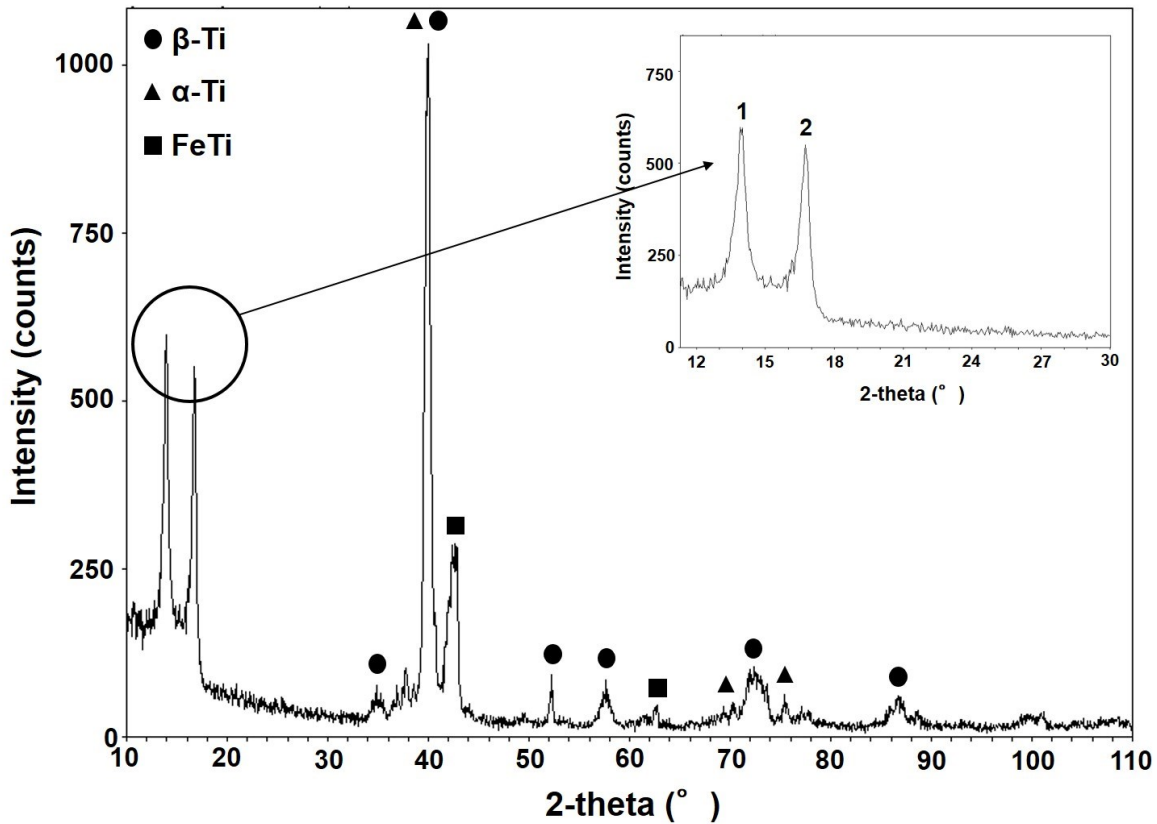


Figure 4.2: XRD pattern for as-received ferrotitanium alloy.

Figure 4.3 shows typical SEM BSE images (lower and higher magnification) of the as-received commercial grade ferrotitanium alloy. Five different contrast regions, labelled 1 through 5, are visible. BSE images reveal atomic number contrast, with regions containing higher atomic number elements appearing bright relative to low atomic number regions.

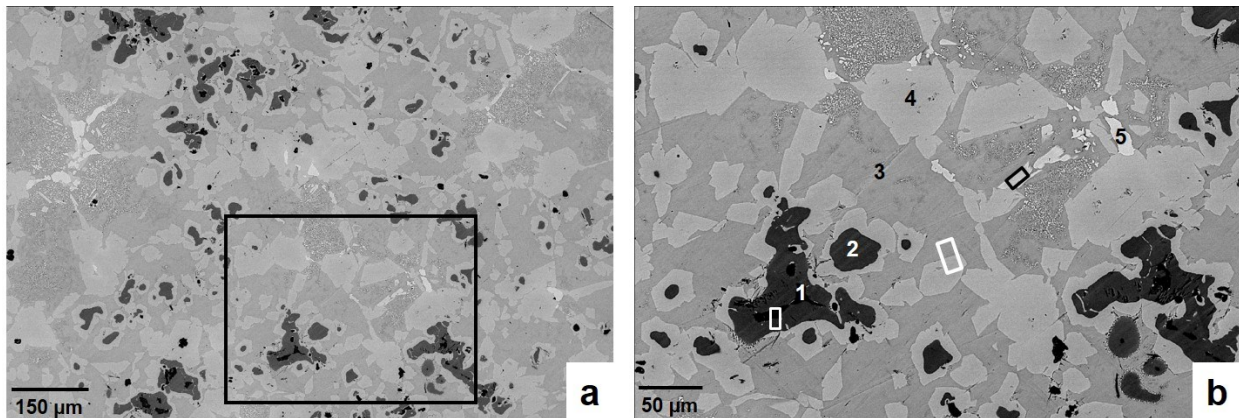


Figure 4.3: a) SEM BSE image of as-received commercial grade ferrotitanium alloy showing the overall microstructure. b) Higher magnification SEM BSE image of the area indicated in (a) showing five different contrast regions labelled 1-5.

The chemical composition of each of the areas labelled in Fig. 4.3 was analyzed using EDX spectroscopy in the SEM. Several regions with similar contrast were analyzed; composition ranges are given in Table 4.2.

Table 4.2: EDX analysis of chemical composition (wt.%) of the regions labeled in Figure 4.3

<b>Analysis Technique</b>	<b>Element</b>	<b>Region 1</b>	<b>Region 2</b>	<b>Region 3</b>	<b>Region 4</b>	<b>Region 5</b>
SEM EDX	Ti	Nearly 100	97-98	70-73	64-68	48-49
	Fe	-	-	17-21	27-30	45-46
	Al	-	2-3	5-6	3-4	2-3
	V	-	-	3-4	1.5-2.5	1-2
	Others	-	-	-	-	~2
TEM EDX	Ti	Nearly 100	95-98	79-80	70-74	51-52
	Fe	-	~1	11-12	22-24	42-43
	Al	-	2-4	8-10	3-6	2.5-3.5
	V	-	-	-	-	~2
	Others	-	-	-	-	1-1.5

The volume fraction of each region was calculated using FIJI software. Five low magnification (ranging from 50X to 150X) images of representative microstructure were used and the average volume fractions of each region are reported in Table 4.3 along with their standard deviations. Regions 3 and 4 are the major constituents of the alloy.

Table 4.3: Volume fractions for the regions identified in Figure 4.3

<b>Region 1</b>	<b>Region 2</b>	<b>Region 3</b>	<b>Region 4</b>	<b>Region 5</b>
Mean: 0.013	Mean: 0.102	Mean: 0.475	Mean: 0.404	Mean: 0.0054
St Dev: 0.0055	St Dev: 0.008	St Dev: 0.0233	St Dev: 0.0327	St Dev: 0.003

St Dev: standard deviation

Region 1 in Figure 4.3b has the darkest contrast and is almost pure titanium, according to the EDX analysis. Based on the phase diagram, this phase might be expected to be hexagonal  $\alpha$ -titanium, which has virtually no solubility for iron. Region 2 is slightly less dark and is almost all titanium with a small amount of aluminum (Table 4.2). According to the titanium-aluminum phase diagram,  $\alpha$ -titanium can dissolve more than 7 wt.% aluminum at temperatures exceeding 773 K (500°C) [Ohn00], so region 2 could be  $\alpha$ -titanium as well. It is unlikely that both regions are  $\alpha$ -titanium. This will be discussed in subsequent paragraphs. In addition, based on the BSE image in Figure 4.3b, region 1 has a lower average atomic number than region 2, which is counterintuitive to the SEM EDX data in Table 4.2. The EDX detector used for the composition analysis in the SEM was not able to reliably detect lighter elements, such as carbon and nitrogen. The apparent discrepancy between the EDX and BSE imaging results may be due to the presence of one or more of these lighter elements. WDS analysis was done on regions 1 and 2. Both carbon and nitrogen were detected in region 1 (1-2 wt.% carbon and 3-4 wt.% nitrogen), while no carbon or nitrogen was detected in region 2. Regions 1 and 2 were, therefore, tentatively identified as titanium carbonitride and  $\alpha$ -titanium, respectively.

A FIB sample was prepared across the boundary between region 1 and 2 (indicated by the white rectangle in Figure 4.3b). The sample was then analyzed in the TEM, initially through EDX analysis to confirm the SEM EDX results (Table 4.2). Figure 4.4 shows a low magnification TEM bright field (BF) image of regions 1 and 2; a third region is visible in this image as well (darker contrast). EDX spectra, from the low energy range, for regions 1 and 2 are also shown to compare the relative carbon and nitrogen compositions. Nitrogen is difficult to discern with any certainty, as its K X-ray peak overlaps with the L X-ray peak for titanium. However, region 1 clearly contains more carbon than region 2; the small carbon peak in region 2 may just be carbon contamination from the atmosphere. Based on the TEM EDX results, as well as the WDS results, region 1 appears to be a titanium carbonitride and not  $\alpha$ -titanium. In addition, region 1 does not contain any aluminum (Table 4.2), while region 2 contains about 2-4 wt.% aluminum.

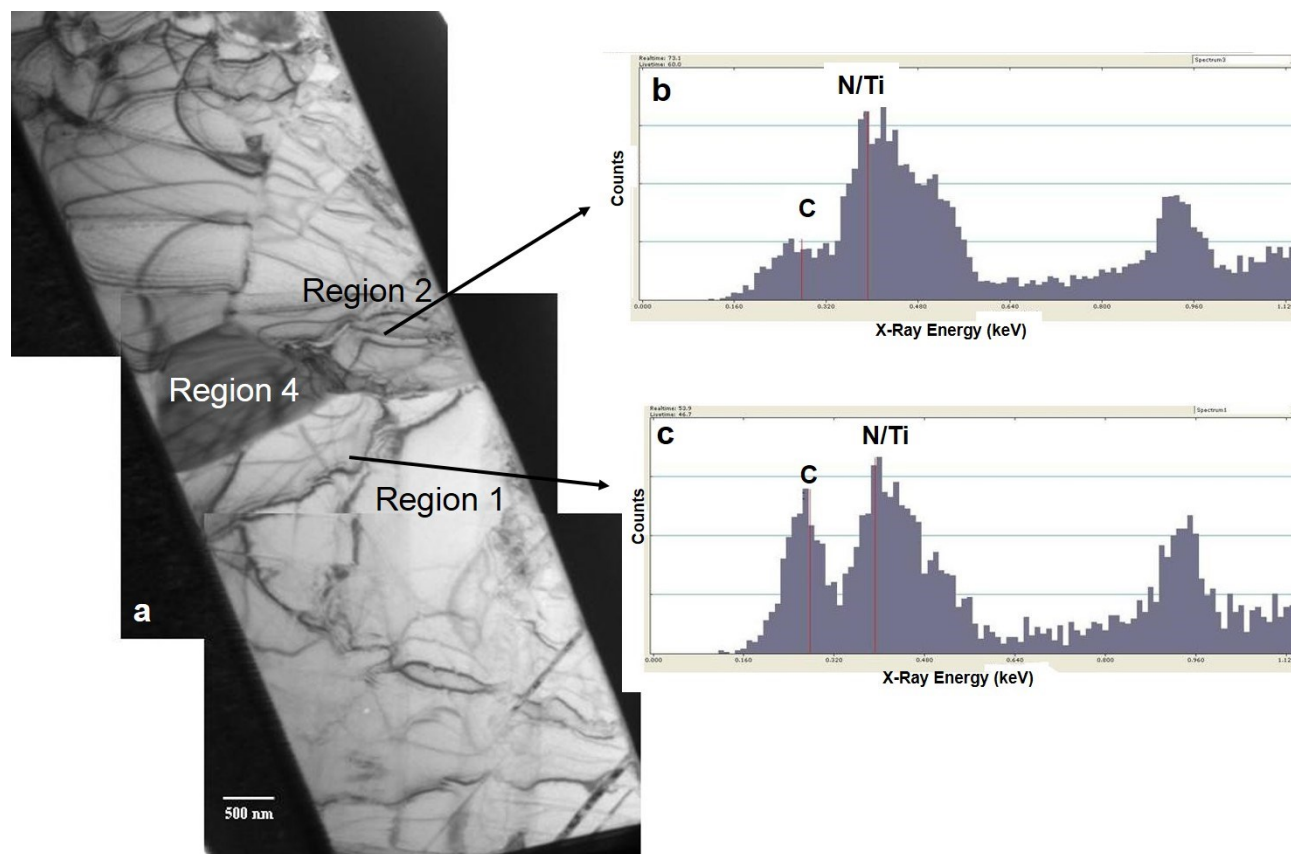


Figure 4.4: a) TEM BF image of regions 1 and 2 from Fig. 3b, b) and c) EDX spectra for the low energy range from regions 2 and 1, respectively.

Several selected area diffraction (SAD) patterns, from at least three different orientations, were taken from region 1 and region 2; two orientations for each region are shown in Figure 4.5. Region 1 was indexed to  $\text{Ti}(\text{C}_x\text{N}_{1-x})$  ( $0 \leq x \leq 1$ ) which has a NaCl-type crystal structure, while region 2 was indexed to  $\alpha$ -titanium. The carbon and nitrogen compositions in the carbonitride could not be determined directly from EDX analysis. Instead they were indirectly approximated based on Vegard's Law [Den91], *i.e.*, by assuming a linear dependence between the lattice parameter and the composition variable  $x$ . The lattice parameter was determined from the diffraction pattern d-spacings. The lattice parameters for TiN and TiC are 0.424 nm and 0.435 nm, respectively. The

lattice parameter for  $\text{Ti}(\text{C}_x\text{N}_{1-x})$  was slightly larger than the value for  $\text{TiN}$  ( $\sim 0.425$  to  $0.427$  nm), which means that the carbonitride is nitrogen rich with  $x < 0.3$ .

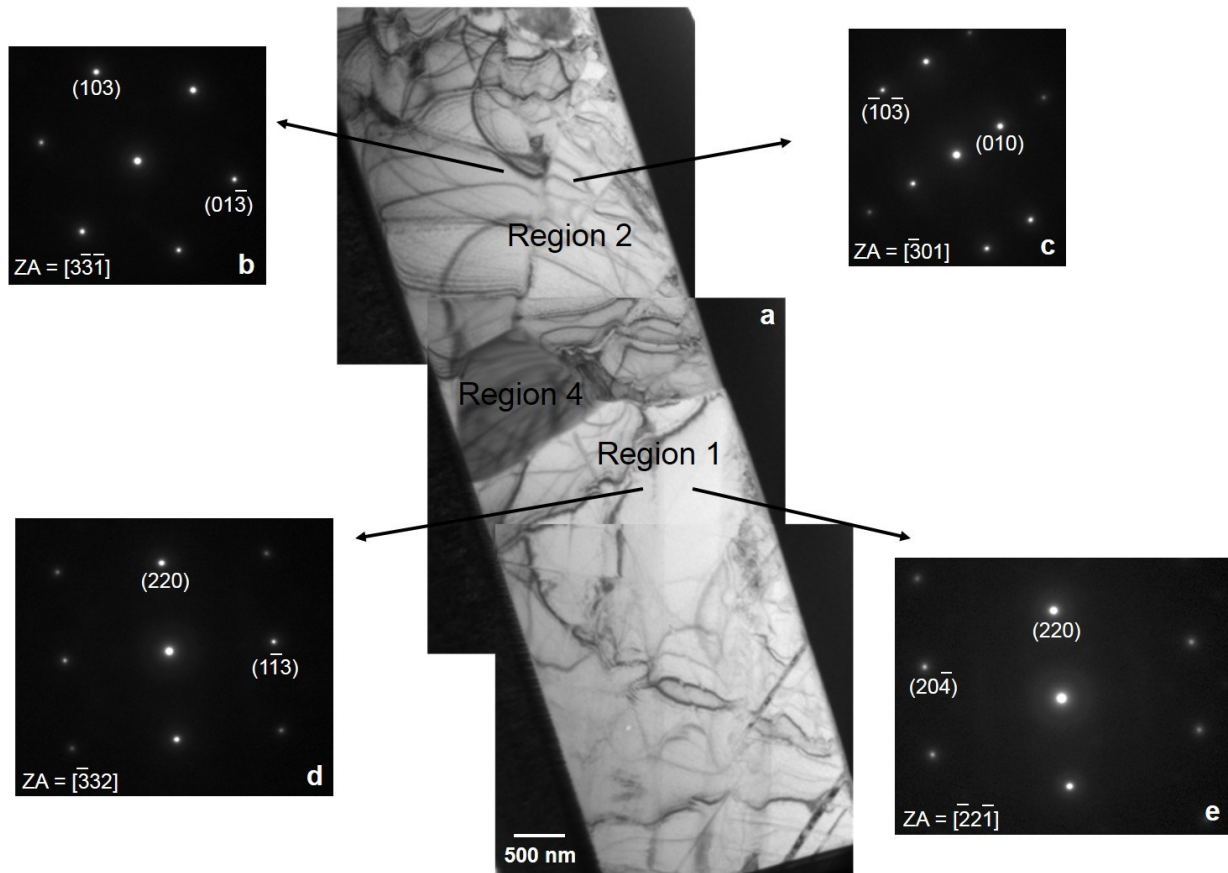


Figure 4.5: a) TEM BF image of regions 1, 2 and 4 from Fig. 3b. b) and c) SAD patterns from region 1, indexed as  $\text{Ti}(\text{C}_x\text{N}_{1-x})$ . d) and e) SAD patterns from region 2, indexed as  $\alpha$ -titanium.

Regions 3 and 4 in Figure 4.2 have similar compositions (Table 4.2), with the main difference being the amount of iron which is higher for region 4. Either or both of these regions could be  $\beta$ -titanium, which has a high solubility for iron (up to 20 wt.% - Figure 4.1)) and aluminum (up to 30 wt.%) [Oka96, Ohn00]. However, it is unlikely that both regions are  $\beta$ -titanium; one region may be a titanium-iron-aluminum intermetallic. Again, for conclusive identification, a FIB sample

was prepared across the boundary between regions 3 and 4 (indicated by the white rectangle in Figure 4.3b). A TEM BF image of this sample is shown in Figure 4.6. The phase boundary is clearly visible; at least three SAD patterns were taken from both regions at different orientations. Representative patterns are shown in Figure 4.6. Patterns from region 3 were indexed to  $\beta$ -titanium (BCC crystal structure). There is a significant difference between the lattice parameter for pure  $\beta$ -titanium and the lattice parameter for region 3. The lattice parameter for pure  $\beta$ -titanium is 0.3306 nm, while the lattice parameter for region 3 ranges from 0.318 to 0.324 nm (calculated from the SAD patterns). This difference can be attributed to the presence of up to 21 wt.% iron and 10 wt.% aluminum in solid solution (Table 4.2) in region 3. The atomic radii for both iron (0.1241 nm) and aluminum (0.1431 nm) are smaller than that for titanium (0.1432 nm) [Wil07], which accounts for the reduction in the lattice parameter for  $\beta$ -titanium.  $\beta$ -titanium is not thermodynamically stable at room temperature, but is present in the ferroalloy because of the presence of impurities and non-equilibrium conditions during ferroalloy formation.

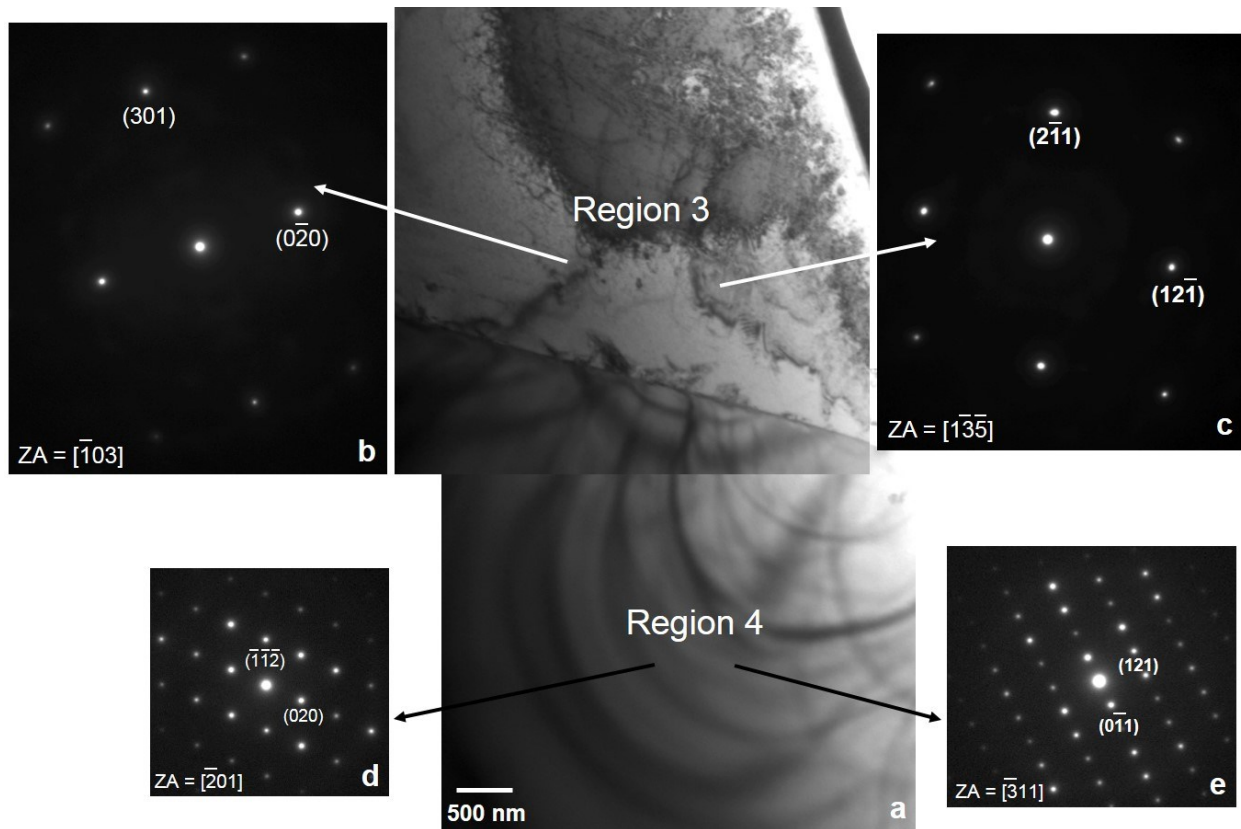


Figure 4.6: a) TEM BF image showing regions 3 and 4 from Figure 4.3b. b) and c) SAD patterns from regions 3 indexed to  $\beta$ -titanium. d) and e) SAD patterns from region 4 indexed to titanium-iron-aluminum ternary intermetallic (magnified 1.5 times relative to SAD patterns in (b) and (c)).

The SAD patterns from Region 4 do not correspond to any known iron-titanium binary phases. Abraham et al. [Abr06(2)] reported an unknown phase with nearly the same composition with a BCC crystal structure ( $a \sim 1.3$  nm). Gertsman et al. [Ger06] also studied similar commercial iron-titanium alloys and reported a new phase with a composition of 68-74 at.% titanium, 20-24 at.% iron and 3.5-7 at.% aluminum (68-73.5 wt.% titanium, 23-28 wt.% iron and 2-4 wt.% aluminum). The structure was body centered orthorhombic with  $a$  almost equal to  $b = 1.299$  nm and  $c = 1.344$  nm and contained 128 atoms. The lattice parameters are approximately four times larger than that

of  $\beta$ -titanium. The exact positions of the atoms in the structure are not yet known. The SAD patterns for region 4 can be indexed to this ternary intermetallic phase; two orientations are shown in Figure 4.6.

Earlier in this section, it was mentioned that there were two intense low angle peaks in the XRD pattern at 2-theta values of  $13.9^\circ$  and  $16.7^\circ$  (corresponding to d-spacings of 0.635 nm and 0.529 nm, respectively) (Figure 4.2). Based on the ternary intermetallic identified by Gertsman et al. [Ger06], the two peaks can be indexed as  $\{200\}/\{020\}$  planes ( $d= 0.6495$  nm in [Ger06] and  $\{121\}/\{211\}$  planes ( $d= 0.533$  nm in [Ger06]). The d-spacing differences for this work and Gertsman's work are not significant, especially considering the range of composition for the ternary intermetallic.

Region 5 in Figure 4.3b is the brightest region, as well as the region with the lowest volume fraction of the 5 regions. Region 5 has comparable amounts of titanium and iron, with smaller amounts of aluminum and vanadium (Table 4.2). Based on the titanium-iron phase diagram, this area may be the FeTi intermetallic. A third FIB sample was prepared from this region (indicated by the black rectangle in Figure 4.3b). TEM BF images and representative SAD patterns from two orientations are shown in Figure 4.7. The SAD patterns were indexed to FeTi, which has a CsCl-type crystal structure with a lattice parameter close to that of  $\beta$ -titanium (due to similar atomic radii for titanium and iron).

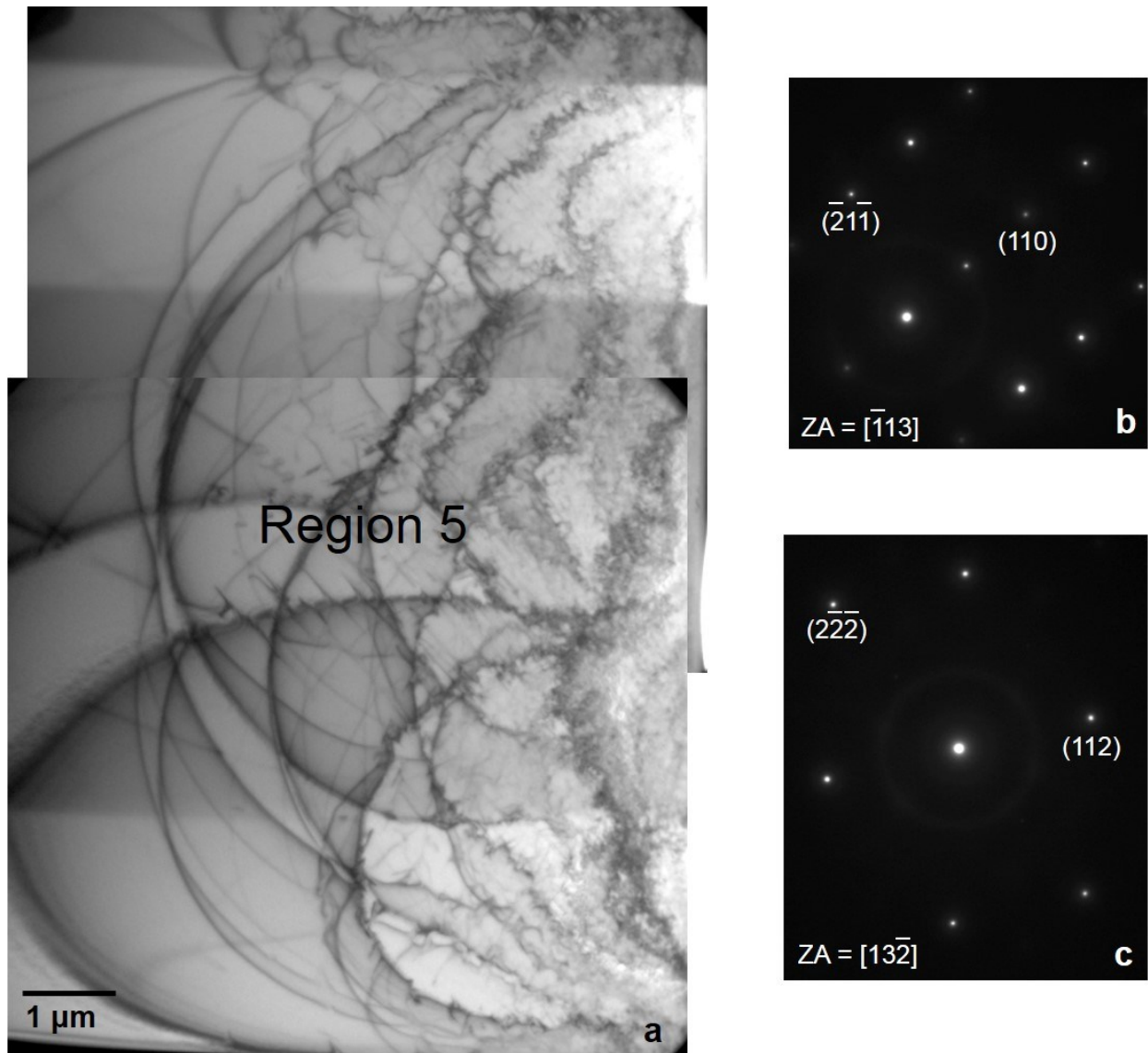


Figure 4.7: a) TEM BF image of region 5 from Figure 4.3b. b) and c) SAD patterns from region 5. The patterns were indexed to FeTi.

To summarize, five phases were identified for the ferrotitanium alloy. Crystallographic data for these phases is given in Table 4.4.

Table 4.4: Crystallographic data for ferrotitanium phases

Phase	Ti(C <sub>x</sub> N <sub>1-x</sub> )	$\alpha$ -Ti	$\beta$ -Ti	Ternary intermetallic	FeTi
Structure	NaCl	HCP	BCC	body-centred orthorhombic	CsCl
Space Group	Fm-3m	P63/mmc	Im-3m	Immm	Pm-3m
Lattice parameters (nm)	0.425- 0.426 (this work)	a = b = 0.295 c = 0.4683 [Database*]	a = 0.318- 0.324 nm (this work)	a ~ b = 1.299 c = 1.344 [Ger06]	a = 0.2976 [Database*]

\* International Center for Diffraction Data (ICDD) database, pdf charts

#### 4.3.2. Ferroniobium (Iron-Niobium)

According to the equilibrium iron-niobium binary phase diagram [Oka93], shown in Figure 4.8, the ferroalloy (based on the composition in Table 4.1) should be primarily  $\mu$ -Fe<sub>7</sub>Nb<sub>6</sub> with smaller amounts of the niobium-rich solid solution. These two phases were tentatively identified from the XRD pattern in Figure 4.9. Unlike ferrotitanium, there was not much difference between the d-spacings for the pure phases and those in the XRD pattern, which is due to the lower impurity content in the commercial ferroniobium (Table 4.1).

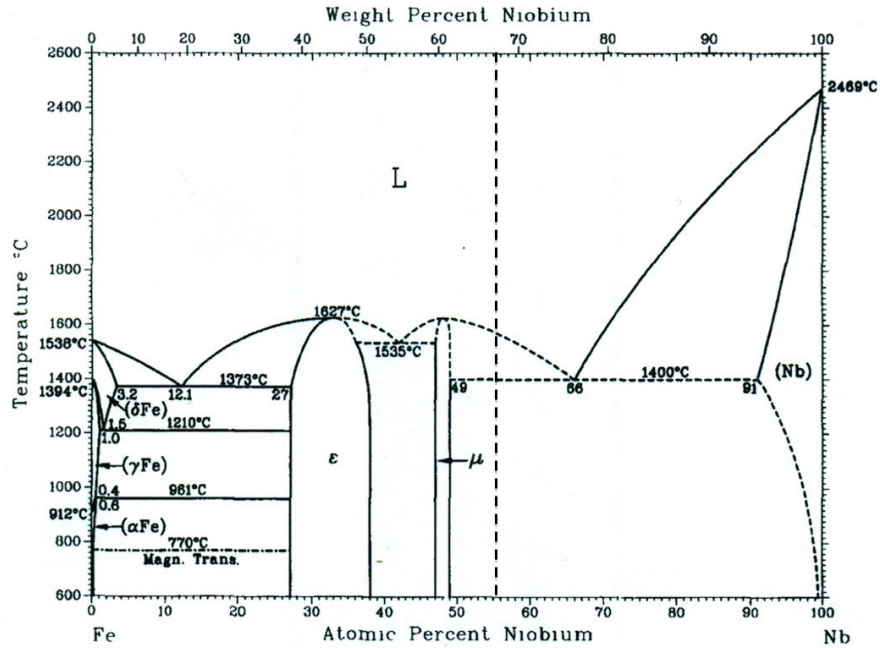


Figure 4.8: Iron-niobium binary phase diagram [Oka93]. The vertical line represents the ferroniobium alloy composition (iron and niobium only).

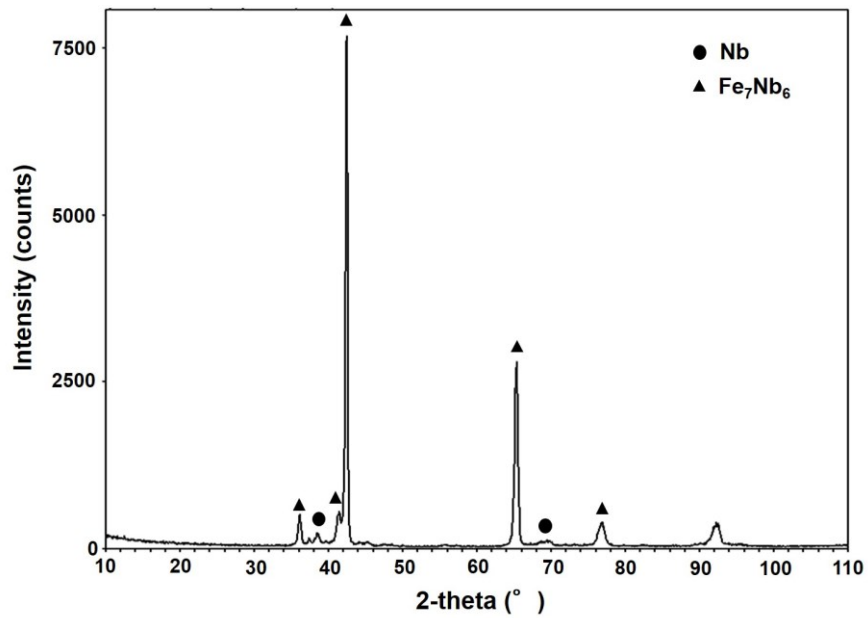


Figure 4.9: XRD pattern for as-received ferroniobium alloy.

Fig. 4.10 shows SEM BSE images of the as-received commercial ferroniobium alloy; three different contrast regions, labelled as 1, 2 and 3, are shown. The composition of each region is given in Table 4.5 and volume fractions of each region are provided in Table 4.6. The alloy consists primarily of region 3, with smaller and similar amounts of regions 1 and 2.

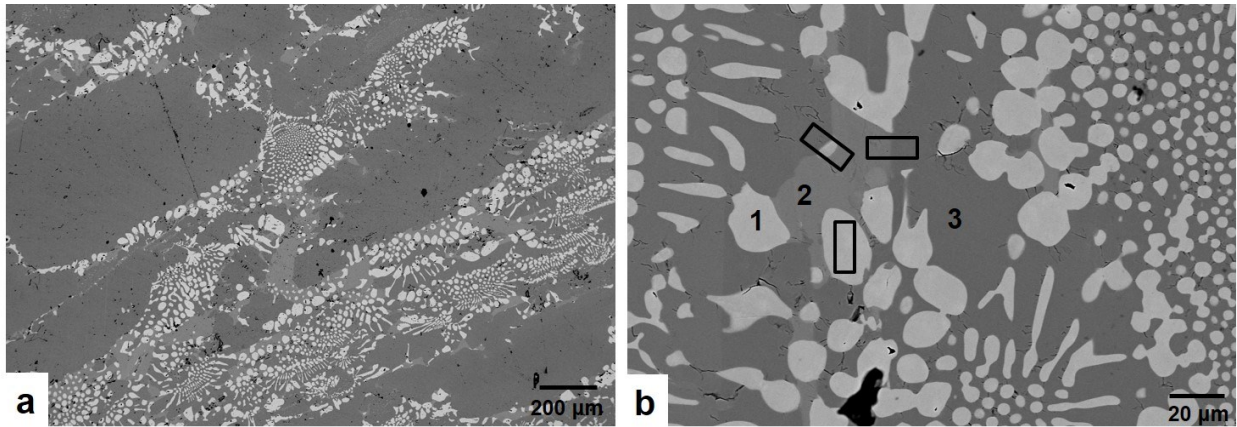


Figure 4.10: a) SEM BSE image of as-received commercial grade ferroniobium alloy showing overall microstructure. b) Higher magnification SEM BSE image of ferroniobium showing three different contrast regions labelled 1-3.

Table 4.5: Chemical composition of each region (wt.%) labeled in Fig. 4.10

<b>Analysis Technique</b>	<b>Element</b>	<b>Region 1</b>	<b>Region 2</b>	<b>Region 3</b>
SEM EDX	Nb	94-95	64-66	58-59
	Fe	5-6	33-34	41-42
	Ti	-	~ 1	~ 1
TEM EDX	Nb	95-97	63-64	55-56
	Fe	3-5	35-36	43-44
	Ti	-	< 1	< 1

Table 4.6: Volume fractions of the regions labeled in Figure 4.10

<b>Region 1</b>	<b>Region 2</b>	<b>Region 3</b>
Mean: 0.1013	Mean: 0.105	Mean: 0.794
St Dev: 0.017	St Dev: 0.019	St Dev: 0.029

St Dev: standard deviation

Based on the EDX analysis in Table 4.5, region 1 appears to be a niobium-rich solid solution, although the iron content exceeds the equilibrium value for room temperature (Figure 4.8). A FIB sample was prepared from region 1 (indicated by the black rectangle in Figure 4.10b) and a TEM BF image is shown in Figure 4.11. Three grains are clearly visible; grains 1 and 2 are niobium-rich (95-97 wt.% niobium – Table 4.5) and correspond to region 1 in the SEM images. Several SAD patterns were taken from these grains at different orientations. Two representative patterns are shown in Figure 4.11b and 4.11c; these were indexed to BCC niobium.

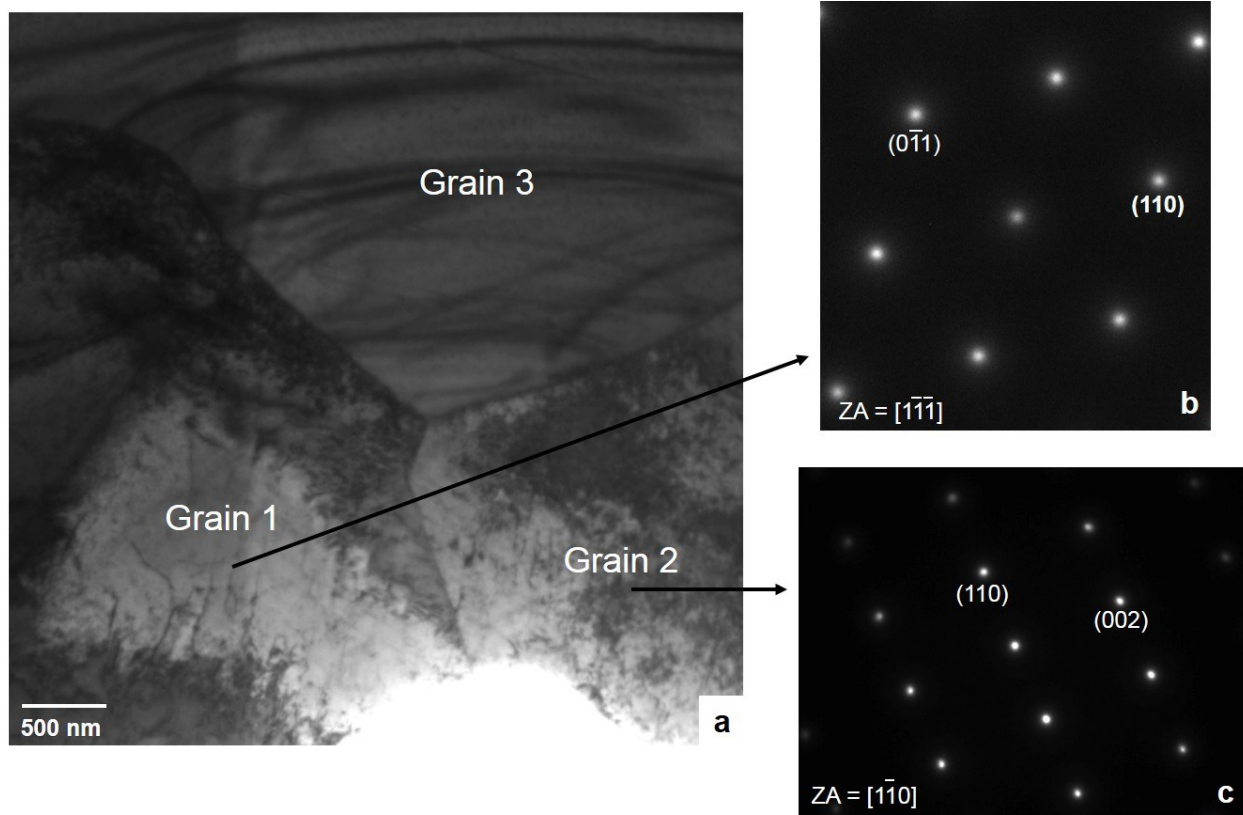


Figure 4.11: a) TEM BF image taken from region 1 of Figure 4.10. b) and c) SAD patterns taken from grains 1 and 2 (both region 1) and indexed to BCC niobium.

Regions 2 and 3 have similar compositions (region 2 is slightly niobium-rich relative to region 3) and appear to correlate with  $\mu$ -Fe<sub>7</sub>Nb<sub>6</sub>. This intermetallic phase is non-stoichiometric and exists over a range of composition from 59.1-63.4 wt.% niobium (Figure 4.8) [Vob11]. However, it seems unlikely that two distinctly different regions (in terms of composition) of the same phase would form in the alloy unless they formed at different times during alloy fabrication. To determine the nature of the two regions, a FIB sample across the boundary separating regions 2 and 3 was prepared (indicated by the black rectangle in Figure 4.10b) and examined in the TEM.

Figure 4.12 shows a TEM BF image and SAD patterns from regions 2 and 3. EDX analysis in the TEM confirmed that region 2 is niobium-rich relative to region 3 (Table 4.5). Both patterns can be indexed to  $\mu\text{-Fe}_7\text{Nb}_6$ , which appears to indicate that the two different contrast regions (2 and 3) in Figure 4.10 are the same phase.

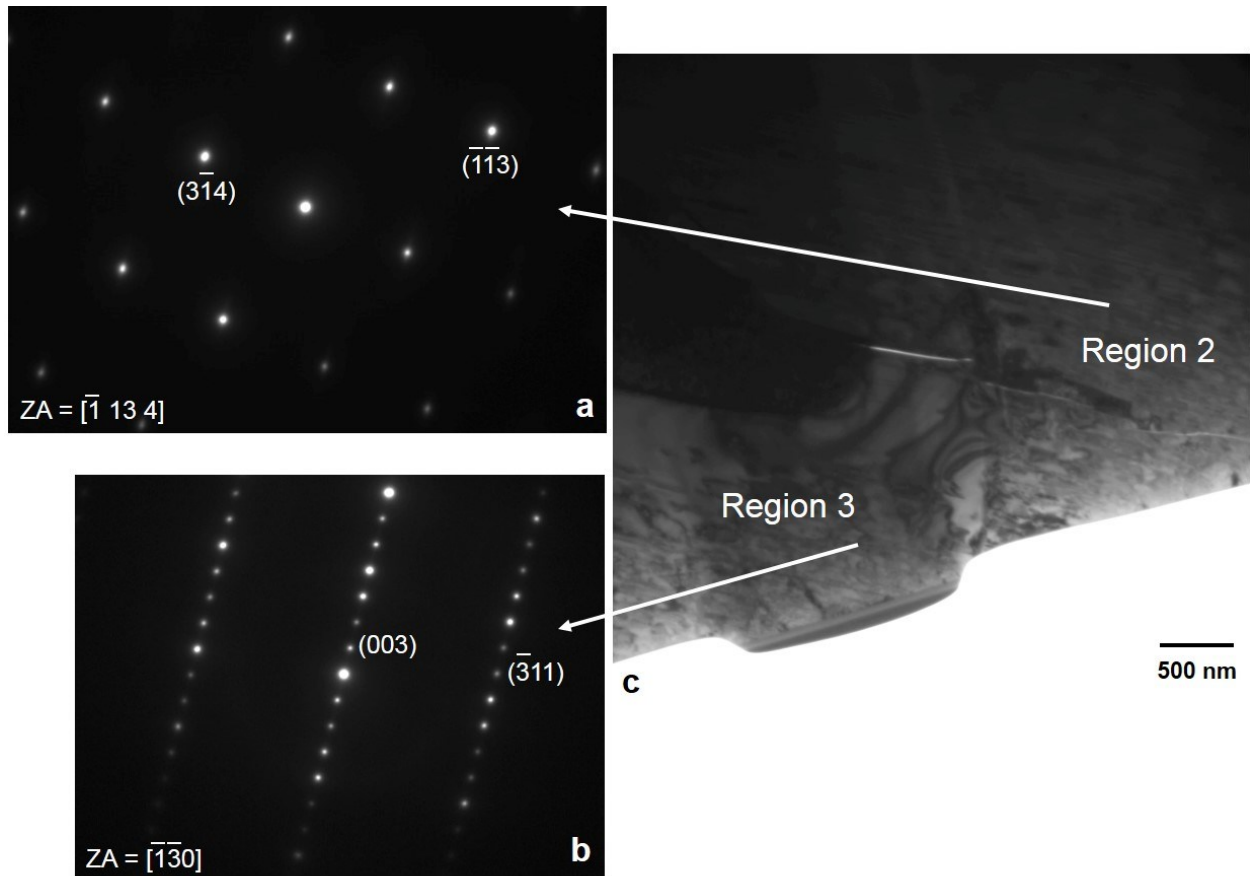


Figure 4.12: a) TEM BF image of region 2 and 3 from Figure 4.10. b) and c) SAD patterns taken from region 2 and 3, respectively and indexed to  $\mu\text{-Fe}_7\text{Nb}_6$ .

For clarification, the FIB sample shown in Figure 4.12 was further thinned to obtain better images and for additional analysis. The resulting images are shown in Figure 4.13. Figure 4.13b shows a magnified image of the region indicated in Figure 4.13a; this region has been tilted to a different

orientation. Tilting the sample leads to the appearance and disappearance of parallel striation features, which appear to be microtwins or stacking faults. The SAD pattern in Figure 4.13c shows streaking of the diffraction spots in the direction perpendicular to the striations in Figure 4.13b, which is another indication of faulting.

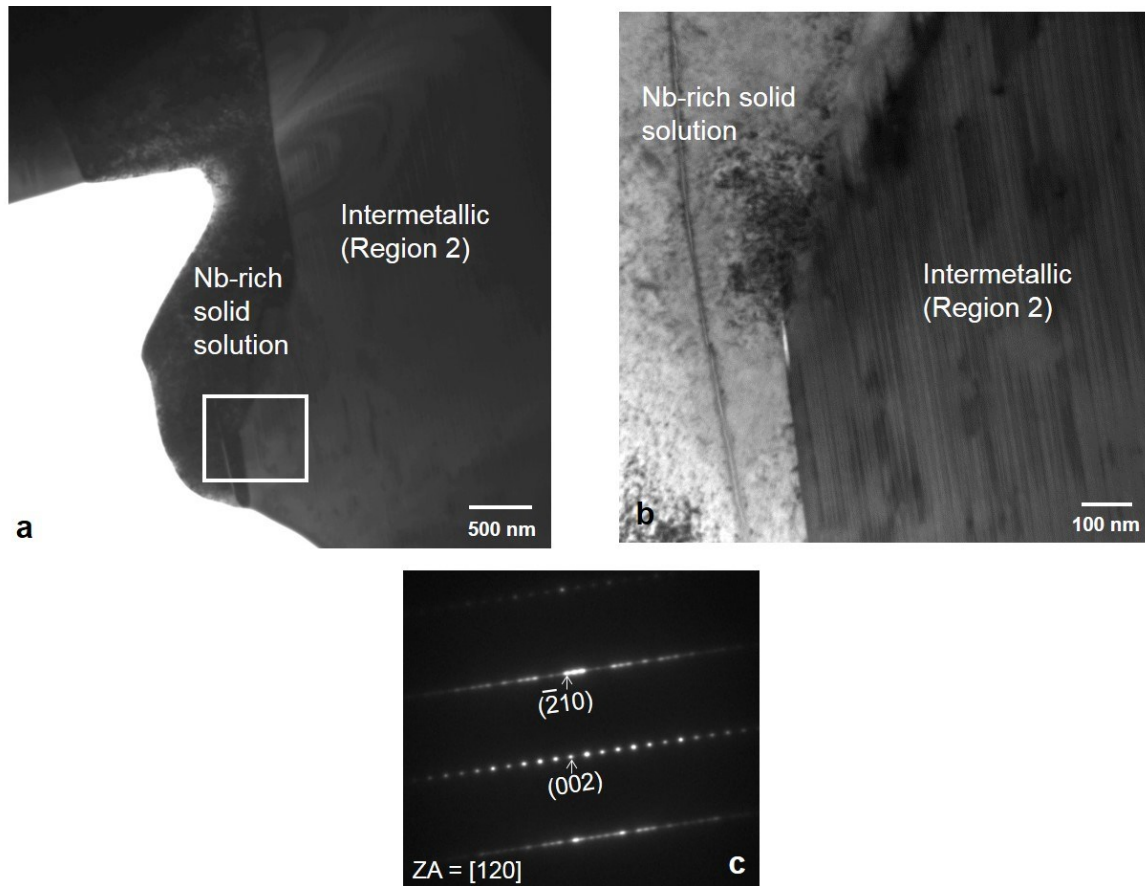


Figure 4.13: a) TEM BF image of FIB sample after further thinning, b) Higher magnification TEM BF image of area indicated in (a) showing striation features in the  $\mu$  phase when tilted. c) SAD pattern from intermetallic indexed to the  $\mu$  phase showing streaking of diffraction spots perpendicular to striation features.

The  $\mu$  phase has a rhombohedral unit cell, with 13 atoms in total, and exhibits polytypism [Kum98, Del92]. Striation features, similar to the ones reported here, have been reported for other intermetallic compounds ( $\text{Co}_7\text{W}_6$ ), oxides ( $\text{Cr}_2\text{O}_3$ ) and pure metals (boron) with rhombohedral structures. The striations in those cases were found to be associated with twinning and stacking faults [Car01, Man07, Mck82].

Another FIB sample, containing all three regions, was prepared (indicated by the black rectangle in Figure 4.10b). The striation features also show up in region 3, but are much more prevalent in region 2 (Figure 4.14). In addition, region 2 has relatively more niobium compared with region 3 (Table 4.3). Note also that from the quantitative phase analysis shown in Table 4.6 (calculated using FIJI software), Region 3 is the largest phase component in the structure of this ferroalloy. Hence, it must be a primary phase as per the phase diagram.

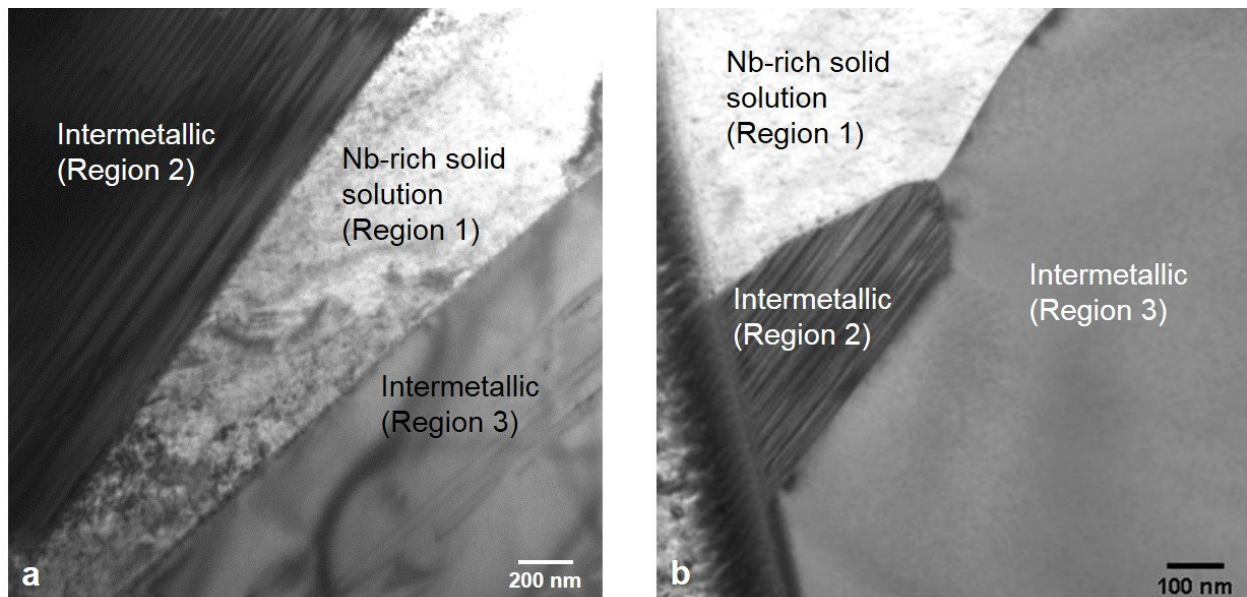


Figure 4.14: a) and b) TEM BF images showing the three regions in the ferroniobium alloy. The striation features are more prevalent in region 2 than region 3.

A possible explanation for the difference in the composition and morphology between these two regions, even though they are essentially the same phase ( $\mu\text{-Fe}_7\text{Nb}_6$ ), can be given with the help of the iron-niobium phase diagram (Figure 4.8). According to the phase diagram,  $\mu\text{-Fe}_7\text{Nb}_6$  forms at two different temperatures during cooling from the liquid. Proeutectic  $\mu\text{-Fe}_7\text{Nb}_6$  forms initially (starting at  $\sim 1873$  K ( $1600^\circ\text{C}$ )), followed by  $\mu\text{-Fe}_7\text{Nb}_6$  as part of the eutectic reaction ( $\mu\text{-Fe}_7\text{Nb}_6$  + niobium solid solution phase at  $\sim 1673$  K ( $1400^\circ\text{C}$ )). The proeutectic  $\mu\text{-Fe}_7\text{Nb}_6$  should be iron-rich (at least initially) relative to  $\mu\text{-Fe}_7\text{Nb}_6$  that forms as part of the eutectic reaction. If the cooling rate is slow enough the niobium content in the proeutectic phase should increase as solidification proceeds reaching the same composition as the eutectic  $\mu\text{-Fe}_7\text{Nb}_6$  at the eutectic temperature. However, during commercial alloy fabrication it is unlikely to reach equilibrium conditions. As such, the proeutectic  $\mu\text{-Fe}_7\text{Nb}_6$  will be slightly iron-rich relative to the eutectic  $\mu\text{-Fe}_7\text{Nb}_6$ . Based on this argument, region 3 is likely proeutectic  $\mu\text{-Fe}_7\text{Nb}_6$  and region 2 is eutectic  $\mu\text{-Fe}_7\text{Nb}_6$ . The difference in formation temperatures for the two forms of  $\mu\text{-Fe}_7\text{Nb}_6$  may also account for the morphology difference. Diffusion rates will be slower at lower transformation temperatures, so the eutectic  $\mu\text{-Fe}_7\text{Nb}_6$  is more likely to form non-equilibrium structures such as the stacking faults/twins seen in region 2 (eutectic form of  $\mu\text{-Fe}_7\text{Nb}_6$ ). Figure 4.10a, which shows a relatively low magnification image of the overall microstructure, provides additional justification for this explanation. Distinct regions of  $\text{Fe}_7\text{Nb}_6$ , with lower niobium content (proeutectic phase), and eutectic regions, with a mixture of the niobium-rich solid solution and the higher niobium content  $\text{Fe}_7\text{Nb}_6$  intermetallic (formed during the eutectic reaction), are visible.

Closer examination of Figure 4.13b reveals several indistinct regions of dark contrast within the intermetallic phase. These regions are iron-rich relative to the rest of the grain (iron:niobium ratios close to 2:1 - determined through TEM EDX analysis). Diffraction patterns taken from the

intermetallic grain, including the dark contrast regions, do not show any additional diffraction spots. As such these regions do not correspond to a different phase. Instead, these areas are likely localized regions of  $\mu\text{-Fe}_7\text{Nb}_6$  rich in iron, which may be responsible in part for the faulting. Crystallographic information for the two phases in the ferroniobium alloy is summarized in Table 4.7.

Table 4.7: Crystallographic data for ferroniobium phases

Phase	Nb-rich solid solution	$\text{Fe}_7\text{Nb}_6$
Structure	BCC	Rhombohedral
Space Group	Im-3m	R-3m
Lattice parameters (nm)	a = 0.3303 [Database*]	a = b = 0.4928 c = 2.683 [Database*]

\* International Center for Diffraction Data (ICDD) database, pdf charts

Only a limited amount of work has been done previously to characterize these ferroalloys. The phases and phase distributions determined here are likely to be similar for other ferroalloys with similar compositions. For example, as-received ferrotitanium alloys were characterized by Abraham et al. [Abr06(1), Abr06(2)] and Gertsman et al. [Ger06] and their results are consistent with the current study, except for the identification of titanium carbonitride in this work. It is quite possible that titanium carbonitride was present in their samples, but was missed because of its low volume fraction and limited contrast difference relative to  $\alpha$ -titanium. Pande et al. [Pan10] characterized two different chemistries of ferrotitanium, *i.e.*, 70 wt.% titanium and 35 wt.% titanium alloys. Their results for the 70 wt.% titanium alloy are consistent with the ferrotitanium

alloy studied here, with exception of the titanium carbonitride and FeTi, both of which were present in small amounts and may have been missed in their analysis. Abraham et al. [Abr06(1), Abr06(2)] and Pande et al. [Pan10] also studied ferroniobium alloys and their results are consistent with this study. For example, Abraham et al. [Abr06(1)] obtained phase fractions of 0.121 and 0.851 for the niobium-rich solid solution and Fe<sub>7</sub>Nb<sub>6</sub>, respectively. Note that they did differentiate between the two types of the intermetallic phase, as was done in this work.

The phases identified in this study, with melting temperatures higher than steelmaking temperatures, are the niobium-rich solid solution (~ 2673 K (2400°C)) for the ferroniobium alloy and Ti(C<sub>x</sub>N<sub>1-x</sub>) (~ 3273 K (3000°C)) and the titanium-rich solid solution (1833 K (1560°C) to 1923 K (1650°C)) (both  $\alpha$  and  $\beta$  phases) for the ferrotitanium alloy. Not much has been reported in the literature that correlates the presence of coarse niobium- and titanium-rich particles with the high melting phases present in ferroalloys. However, Abraham et al. [Abr06(1), Abr06(2)] have reported the presence of coarse niobium- and titanium-rich particles in processed steel and have also characterized commercial ferroalloys. They attribute the coarse, non-stoichiometric particles to undissolved, high melting temperature phases within the ferroalloys. These coarse particles can have an adverse effect on the mechanical properties of the steel by acting as crack initiation sites. The phase fraction calculations indicate that for the ferroniobium alloy about 10% of the alloy will not melt during steelmaking; for the ferrotitanium alloy this amount is close to 60%. These phases, instead, will need to dissolve and this will only occur if sufficient time is provided. It should be noted that the physical properties for the ternary iron-titanium-aluminum intermetallic, including the melting temperature, are not yet known.

#### 4.4. Conclusions

Two commercial ferroalloys, ferrotitanium and ferroniobium, were characterized using X-ray diffraction and electron microscopy techniques. The ferrotitanium alloy contained ~ 10 wt.% of impurities (aluminum, silicon and vanadium) and was made up of 5 phases. The main phases were a  $\beta$ -titanium solid solution and a titanium-iron-aluminum ternary phase (40-45% each), with smaller amounts of an  $\alpha$ -titanium solid solution (~ 10%), a titanium carbonitride ( $\text{Ti}(\text{C}_x\text{N}_{1-x})$  - 1-2%) and FeTi (trace amounts < 1%). The ferroniobium alloy contained fewer impurities and, as such, fewer phases. The major phase was the  $\mu$  phase ( $\text{Fe}_7\text{Nb}_6$ ) with significant amounts (~ 10% by volume) of the niobium solid solution phase (iron in solution). The  $\mu$  phase ( $\text{Fe}_7\text{Nb}_6$ ) exhibits two morphologies; one contains slightly less niobium and is the proeutectic phase (~ 80% of the overall microstructure), while the other is part of the eutectic (nearly 10% of overall microstructure). A study of the phase evolution process in the ferroniobium alloy is needed in order to evaluate and understand the presence of  $\text{Fe}_7\text{Nb}_6$  intermetallic with two different compositions. This is done in Chapter 5.

#### 4.5. References

Abr06(1): S. Abraham, R. Klein, R. Bodnar and O. Dremailova. Formation of coarse particles in steel as related to ferroalloy dissolution thermodynamics. Part 1: ferroalloy melting, dissolution and microstructures. Material Science and Technology (MS & T), Cincinnati, Ohio, October 2006.

Abr06(2): S. Abraham, R. Klein, R. Bodnar and O. Dremailova. Formation of coarse particles in steel as related to ferroalloy dissolution thermodynamics. Part II: crystallographic study of ferroalloys and coarse particles. Material Science and Technology (MS & T), Cincinnati, Ohio, October 2006.

Cal07: William D. Callister Jr. Materials Science and Engineering, An Introduction. John Wiley and Sons Inc., 2007.

Car01: P. A. Carvalho and JTh. De Hosson. Stacking faults in the  $\text{Co}_7\text{W}_6$  isomorph of the  $\mu$  phase. Scripta Materialia, 2001, 45, 333-340.

Che87: Z. Chen, M. H. Loretto and R. C. Cochrane. Nature of large precipitates in titanium containing HSLA Steels. Materials Science and Technology, 1987, 3, 836-844.

Cos92: G. J. R. Costa. Niobium ferroalloy and niobium additive for steels, cast irons and other metallic alloys. Patent WO/1992/022675.

Cra00: A. J. Craven, K. He, L. A. J. Garvie and T. N. Baker. Complex heterogeneous precipitation in titanium-niobium microalloyed Al-killed HSLA steels-II. Non-Titanium based precipitates. Acta Materialia, 2000, 48, 3869-3878.

Del92: J. Delamare, D. Lemarchand and P. Vigier. Transmission electron microscopy study of the  $\mu$  phase in the Fe-Nd-Al system. *Journal of Magnetism and Magnetic Materials*, 1992, 104, 7, 1092-1093.

Den91: A. R. Denton and N. W. Ashcroft. Vegard's Law. *Physical Review A: Atomic, Molecular and Optical Physics*, 1991, 3, 6, 3161-3164.

Eng92: T. A. Engh. *Principles of Metal Refining*. Oxford University Press, 1992.

Ger06: V. Y. Gertsman and O. Dremailova. Transmission electron microscopy identification of a new Ti-Al-Fe intermetallic compound. *Journal of Material Science*, 2006, 41, 14, 4490-4504.

Gou84: L. Gourtsoyannis, R. I. L. Guthrie and G. A. Ratz. The dissolution of ferromolybdenum, ferroniobium and rare earth (Lanthanide) silicide in cast iron and steel melts. *Electric Furnace Conference Proceedings, the Iron and Steel Society/AIME*, 1984.

Kum98: K. C. H. Kumar, I. Ansara and P. Wollants. Sublattice modelling of the  $\mu$  phase. *Calphad*, 1998, 22, 3, 323-334.

Man07: H. Mandar, T. Uustare, J. Aarik, A. Tarre and A. Rosental. Characterization of asymmetric rhombohedral twins in epitaxial -  $\text{Cr}_2\text{O}_3$ , thin films by X-ray and electron diffraction. *Thin Solid Films*, 2007, 515, 11, 4570-4579.

Mck82: M. J. Mckelvy, A. R. R. Smith and L. Eyring. High resolution electron microscope analysis of  $\{100\}$  twinning in  $\beta$  - rhombohedral boron. *Journal of Solid State Chemistry*, 1982, 44, 3, 374-381.

- Men99: R. Mendoza, J. Huante, M. Alanis, C. Gonzalez-Rivera and J. A. Juarez-Islas. Slab cracking after continuous casting of API 5L X-70 grade steel for pipeline sour gas application. *Iron and Steelmaking*, 1999, 26, 3, 205-209.
- Ohn00: I. Ohnuma, Y. Fujita, H. Mitsui, K. Ishikawa, R. Kainuma and K. Ishida. Phase equilibria in the Ti-Al binary system. *Acta Materialia*, 2000, 48, 3113-3123.
- Oka93: H. Okamoto. Fe-Nb (Iron-Niobium). *Journal of Phase Equilibria*, 1993, 14, 5, 650-652.
- Oka96: H. Okamoto. Fe-Ti (iron-titanium). *Journal of Phase Equilibria*, 1996, 17, 4, 369.
- Pan10: M. M. Pande, M. Guo, X. Guo, D. Geysen, S. Devisscher, B. Blanpain et al. Impurities in commercial ferroalloys and its influence on steel cleanliness. In the proceedings of the Twelfth International Ferroalloys Congress Sustainable Future. Helsinki, Finland, 2010.
- Pot01: R. M. Poths, R. L. Higginson and E. J. Palmiere. Complex precipitation behaviour in a microalloyed plate steel. *Scripta Materialia*, 2001, 44, 147-151.
- Pou85: J. L. Pouchou and F. Pichoir. "PAP" ( $\Phi$ - $\rho$ - $Z$ ) procedure for improved quantitative microanalysis. In: Armstrong JT, Editor. *Microbeam Analysis*. California: San Francisco Press, 1985.
- Rob84: W. Roberts. Recent innovations in alloy design and processing of microalloyed steels. Conference Proceedings of International Conference on Technology and Applications of HSLA Steels, Philadelphia, 3-6 October, 1983, American Society of Metals 1984.
- Vob11: S. Vob, M. Palm, F. Stein and D. Raabe. Phase equilibria in the Fe-Nb system. *Journal of Phase Equilibria and Diffusion*, 2011, 32, 97-104.

Yua09: S. Q. Yuan and G. L. Liang. Dissolving behaviour of second phase particles in Nb-Ti microalloyed steel. *Materials Letters*, 2009, 63, 2324-2326.

## Chapter 5: Microstructural Evolution of a Commercial Grade Ferroniobium

### Alloy<sup>2</sup>

#### 5.1. Introduction

Microalloyed steels are steels with low amounts of alloying additions (a total of less than 0.1 wt.%). This results in a substantial increase in the yield strength compared with plain carbon steels [Gla97]. To achieve the desired mechanical and chemical properties, ferroalloys are added during the steelmaking process [Har71]. However, it has been reported that the addition of ferroalloys, like ferroniobium and ferrotitanium, can lead to the presence of coarse niobium-rich and titanium-rich particles in microalloyed steels which can adversely affect the mechanical properties. The composition of these particles is variable, from very simple to complex non-stoichiometric values [Abr06(1), Abr06(2), Che87, Cra00, Men99, Pot01, Rob84, Yua09].

Ferroalloys can be broadly classified into two categories. There are alloying additions containing phases with melting points lower than the temperatures of the steelmaking process. These generally melt and are dispersed in the molten steel. The second type is alloying additions with phases that have melting points above the temperatures of the steelmaking process. The phases do not melt and must dissolve in the liquid steel, which can require significant dissolution times [Eng92]. For instance, when commercial grade ferroniobium is added during steelmaking it does not melt; rather it progressively dissolves which may result in chemical reactions between the

---

<sup>2</sup> Chapter 5 has been published as Shah et al. "Microstructural evolution and characterization of a ferroniobium alloy. *Emerging Materials Research*. 2013, 2, 79-89. This chapter has excerpts from the paper.

surface of the ferroalloy and the liquid [Cos92]. Abraham et al. [Abr06(1), Abr06(2)] and Pande et al. [Pan10] characterized commercial grade ferroniobium and reported two phases in ferroniobium. According to Abraham et al. [Abr06(1), Abr06(2)], the two phases are a niobium-rich solid solution containing iron and an Fe<sub>7</sub>Nb<sub>6</sub> intermetallic phase. The partially dissolved phase found in the steel is the niobium-rich solid solution.

Microstructural characterization of a commercial grade ferroniobium alloy was done in Chapter 4, using SEM, TEM and XRD [Sha13(1)]. Two phases were identified, a niobium-rich solid solution and Fe<sub>7</sub>Nb<sub>6</sub> intermetallic (with two different morphologies and slightly different compositions). In Chapter 4, it was not clear how the phases developed during alloy formation. The aim of this chapter is to combine microstructural characterization with DSC to better understand the phase evolution mechanisms in the commercial grade ferroniobium alloy.

## **5.2. Experimental Methods**

A VEGA-3 (Tescan) SEM was used at an operating voltage of 20 kV to analyze the microstructure of as-received ferroniobium. A Hitachi NB5000 dual beam FIB-SEM was used to prepare TEM samples. A JEOL JEM-2010 operating at 200 kV was used to obtain both BF and DF images along with SAD patterns. EDX spectra from localized regions were also obtained via a Noran ZMAX30 Si-Li detector EDX detector. SEM, TEM and sample preparation details are given in Sections 3.3 and 3.4 of the thesis. A Setaram Labsys Evo 1600 DSC was used for phase transformation analysis of the ferroniobium alloy. Details of the operating conditions, calibrations and the operating procedure are discussed in Section 3.6 of the thesis.

### 5.3. Results

Scanning electron microscopy was used for preliminary microstructural characterization of ferroniobium and the details are presented in Chapter 4 of the thesis [Sha13(1)]. The SEM results are summarized in Figure 5.1; BSE images show three different contrast regions, labelled as 1, 2 and 3. The composition of each region, as determined by EDX analysis is shown in Table 4.5 of the thesis. Region 1 is niobium-rich and was confirmed through TEM diffraction analysis (section 4.3.2) [Sha13(1)] to be BCC niobium with iron in solid solution. Regions 2 and 3 have similar compositions with the relative amounts of niobium and iron varying by several percent. Region 2 contains more niobium compared with region 3, *i.e.*, 64-65 wt.% niobium for region 2 compared with 58-59 wt.% niobium for region 3.

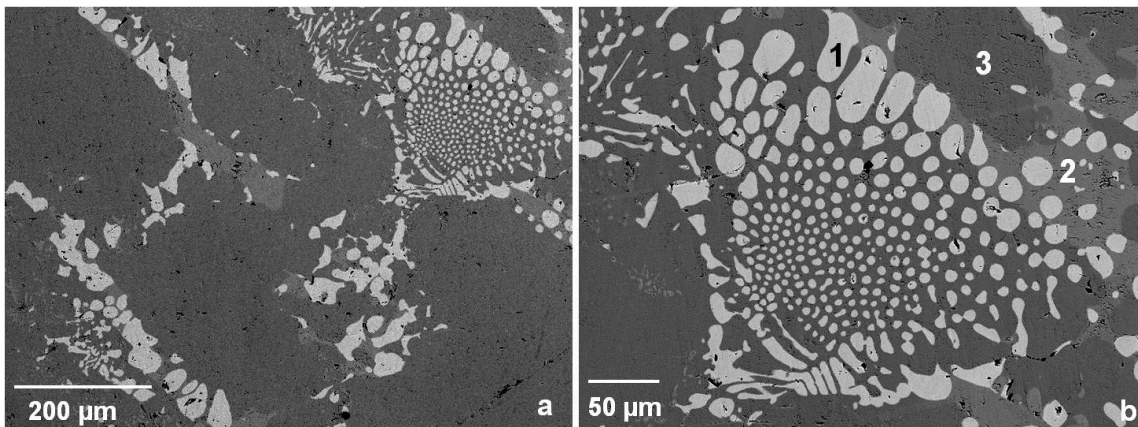


Figure 5.1: a) SEM BSE image of as-received commercial grade ferroniobium alloy showing overall microstructure. b) Higher magnification SEM BSE image of ferroniobium showing three different contrast regions labelled 1-3.

Image J software was used to determine the volume fractions of each region using four representative images of the microstructure (Table 5.1). Region 3 is the majority microconstituent,

making up about 80% of the microstructure, while regions 1 (niobium-rich solid solution) and region 3 comprise about 10% each.

Table 5.1: Volume fractions of the regions labeled in Figure 5.1b - mean fraction (standard deviation)

<b>Treatment</b>	<b>Region 1</b>	<b>Region 2</b>	<b>Region 3</b>
As-received	0.1013 (0.017)	0.105 (0.019)	0.794 (0.029)
DSC sample (10K/min)	0.094 (0.007)	0.101 (0.011)	0.801 (0.005)
DSC sample (20K/min)	0.093 (0.006)	0.148 (0.0006)	0.759 (0.005)
DSC sample (50K/min)	0.093 (0.006)	0.104 (0.007)	0.803 (0.007)

TEM analysis was done to conclusively identify the three regions through imaging, electron diffraction analysis and EDX analysis (section 4.3.2.) [Sha13(1)]. FIB samples were prepared from the three regions. The TEM BF image shown in Figure 5.2 shows all three regions. The TEM EDX results show good agreement with the SEM EDX results (Table 4.5).

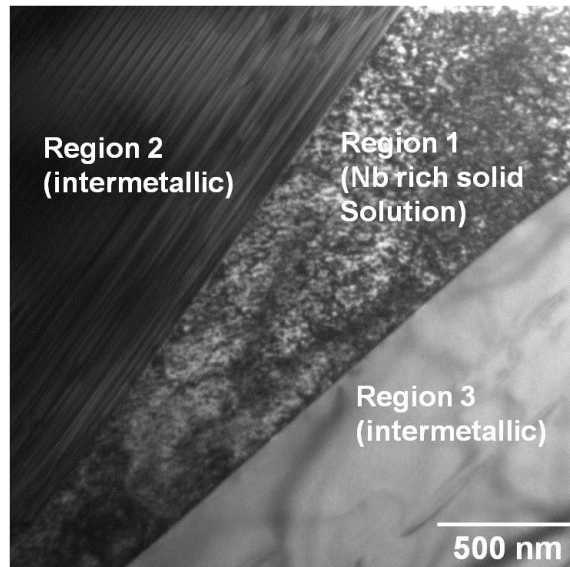


Figure 5.2: TEM BF image showing the three regions in the ferroniobium alloy. The striation features are more prevalent in region 2 than region 3.

Each of the regions was identified through electron diffraction analysis (Section 4.3.2.) [Sha13(1)]. As mentioned above, region 1 was identified as the BCC niobium-rich solid solution phase. The electron diffraction patterns from both regions 2 and 3 were indexed to  $\mu$ -Fe<sub>7</sub>Nb<sub>6</sub>, despite having slightly different compositions. Region 2 exhibited striation-like features, which were also observed in region 3 but were much less prevalent (Figure 4.14 and 5.2). The striations were only visible at certain orientations, as a result of diffraction contrast effects, and as such these were attributed to stacking faults or microtwins [Sha13(1)]. According to Kumar et al. [Kum98] and Delamare et al. [Del92], the  $\mu$  phase has a rhombohedral unit cell, with 13 atoms in total, and exhibits polytypism. Striation-like features associated with twins or stacking faults have also been reported for other alloys systems with  $\mu$  phases as well as some pure metals and oxides which form rhombohedral structures; e.g., the cobalt-tungsten system [Car00, Car01], the molybdenum-

tungsten system [Zhu90], the iron-molybdenum system [Ste79],  $\beta$ -rhombohedral boron [Mck82] and  $\alpha$ -Cr<sub>2</sub>O<sub>3</sub> [Man07].

Regions 2 and 3 are essentially the same intermetallic phase, but with different compositions and defect structures. Region 2 is more niobium-rich compared with region 3 and is more heavily faulted relative to region 3. The obvious question is why there are essentially two forms of the same phase. Region 3 is the majority phase in the alloy, making up about 80% of the microstructure (Table 5.1), while regions 1 and 2 each represent about 10% of the microstructure.

In an attempt to understand the microstructure of the as-received ferroniobium alloy, the solidification behavior was studied using DSC. The samples were heated to 1873 K (1600°C) and cooled in argon gas at 3 different rates: 10 K/min, 20 K/min and 50 K/min. The heating and cooling cycles for the 10 K/min heating/cooling rate are shown in Figure 5.3. The heating and cooling cycles for the 20 and 50 K/min rates were similar. The major difference was the specific values of the transformation temperatures; faster heating/cooling rates led to larger amounts of superheating/undercooling. There were a total of four peaks for all heating and cooling rates. There are three characteristic temperatures in a DSC peak, *i.e.*, the onset temperature (reaction starting temperature), the maximum temperature (temperature of maximum reaction) and the end point temperature (temperature where reaction finishes). The onset temperatures for all three heating and cooling rates are summarized in Table 5.2. Different methods have been reported in literature to determine the onset temperature of a DSC peak, but no one method is considered as a standard method [Fer10]. In the current study a simple approach is taken by using a tangent method to measure the onset temperature of all the peaks in the DSC curve. According to this method the onset temperature is the intersection point of the baseline extension with the tangent to the curve.

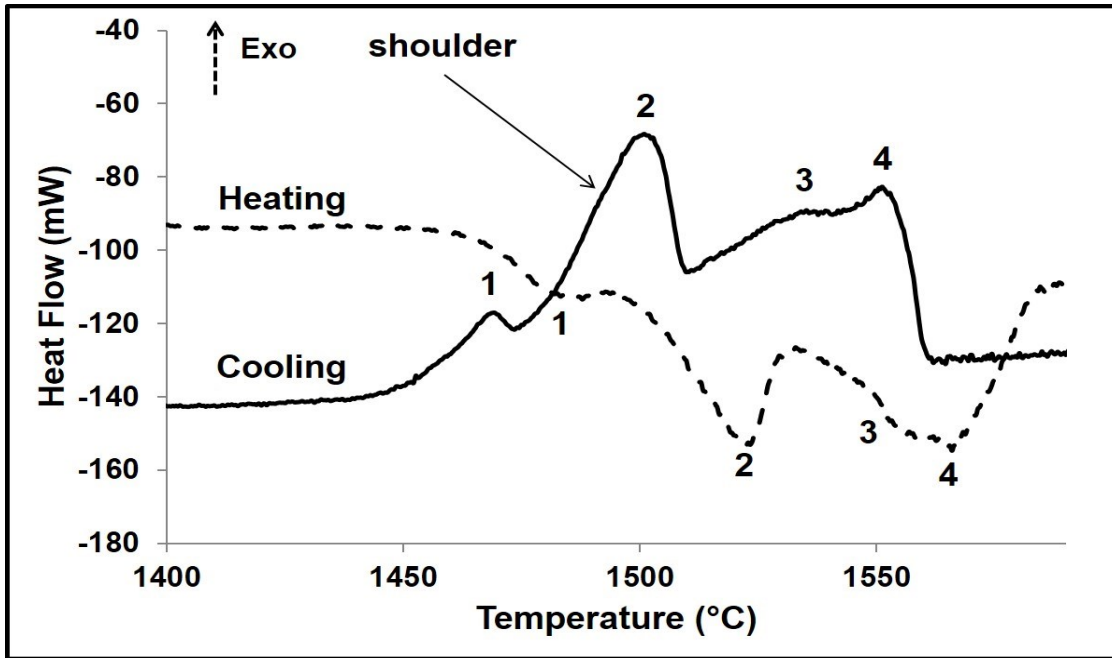


Figure 5.3: Heating and cooling DSC curves at 10 K/min for the ferroniobium alloy.

For the 10 K/min sample the first peak starts at about 1738 K (1465°C) and continues to 1768 K (1495°C) (with a peak maximum at 1760 K (1487°C)). The second peak starts at 1768 K (1495°C) and finishes at 1803 K (1530°C) (with a peak maximum at 1795 K (1522°C)). The third peak starts at 1803 K (1530°C) and ends at 1824 K (1551°C) (with a peak maximum at 1817 K (1544°C)) and the last peak starts at 1824 K (1551°C) and ends at 1853 K (1580°C) (with a peak maximum at 1839 K (1566°C)). For all three heating rates, the four peaks overlap with one another to some degree, *i.e.*, the tail of one peak overlaps with the start of the next peak. Before the first endothermic reaction is completed, the second one has started; the same is true for the second and third and third and fourth endothermic reactions.

Table 5.2: Onset temperatures of DSC peaks for ferroniobium alloy at different heating and cooling rates

Rate (K/min)	Treatment	Peak 1		Peak 2		Peak 3		Peak 4	
		K (°C)		K (°C)		K (°C)		K (°C)	
		Onset	End	Onset	End	Onset	End	Onset	End
Equilibrium [Bej93(1)]	-	1733 (1460)	1763 (1490)	1773 (1500)	1773 (1500)	1773 (1500)	1793 (1520)	1793 (1520)	1801 (1528)
10	Heating	1738 (1465)	1768 (1495)	1768 (1495)	1803 (1530)	1803 (1530)	1824 (1551)	1824 (1551)	1853 (1580)
	Cooling	1748 (1475)	1725 (1452)	1782 (1509)	1748 (1475)	1816 (1543)	1782 (1509)	1833 (1560)	1816 (1543)
20	Heating	1733 (1460)	1770 (1497)	1770 (1497)	1804 (1531)	1804 (1531)	1821 (1548)	1821 (1548)	1848 (1575)
	Cooling	1745 (1472)	1721 (1448)	1777 (1504)	1745 (1472)	1806 (1533)	1777 (1504)	1829 (1556)	1806 (1533)
50	Heating	1738 (1465)	1778 (1505)	1778 (1505)	1819 (1546)	1819 (1546)	1837 (1564)	1837 (1564)	1862 (1589)
	Cooling	1739 (1466)	1712 (1439)	1767 (1494)	1739 (1466)	1793 (1520)	1767 (1494)	1821 (1548)	1793 (1520)

The cooling curves essentially mirror the heating curves, with the slowest cooling rate (10 K/min) exhibiting four distinct exothermic peaks. For the slowest cooling rate, the first exothermic peak (peak 4) starts at about 1833 K (1560°C) and finishes at about 1816 K (1543°C) (peak maximum at 1824 K (1551°C)), the second peak (peak 3) starts at 1816 K (1543°C) and finishes at about 1782 K (1509°C) (peak maximum at 1808 K (1535°C)), the third peak (peak 2) starts at 1782 K (1509°C) and finishes at 1748 K (1475°C) (peak maximum at 1774 K (1501°C)) and the last exothermic peak (peak 1) starts at 1748 K (1475°C) and ends at 1725 K (1452°C) (peak maximum at 1742 K (1469°C)). As with the heating peaks, the cooling peaks also overlap somewhat, indicating overlap among the exothermic reactions. It appears that the four endothermic peaks (on heating) correspond to the four exothermic peaks (on cooling), with the temperature differences corresponding to superheating for the heating cycle and undercooling for the cooling cycle.

All samples, after going through the heating and cooling cycles, were studied using SEM. The resultant images are shown in Figure 5.4. The same three contrast regions, as identified in the as-received sample, are present and are labeled accordingly. EDX analysis confirmed that these regions were the niobium-rich solid solution, the niobium-rich  $\text{Fe}_7\text{Nb}_6$  intermetallic and the niobium depleted  $\text{Fe}_7\text{Nb}_6$  intermetallic. However, as expected, the microstructure became progressively finer as the cooling rate increased.

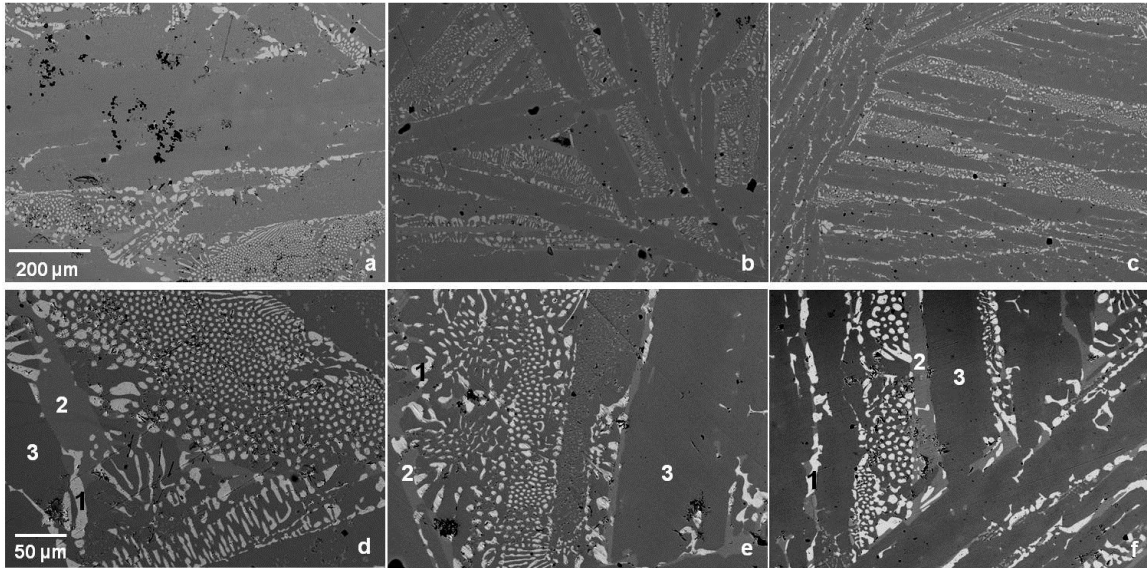


Figure 5.4: SEM BSE images of DSC ferroniobium samples after heating and cooling at different rates: a), d) 10 K/min; b), e) 20 K/min; c), f) 50 K/min.

The phase fraction for each region was measured, using four representative images of each microstructure, and is reported in Table 5.1. The phase fractions are similar for each cooling rate and similar to those determined for the as-received sample. There is approximately 10% of the niobium-rich solid solution phase, 10% of the niobium-rich  $\text{Fe}_7\text{Nb}_6$  intermetallic and 80% of the niobium deficient  $\text{Fe}_7\text{Nb}_6$  intermetallic. The only anomaly is the 20 K/min DSC sample, where the intermetallic amounts vary, *i.e.*, about 15% of the niobium-rich  $\text{Fe}_7\text{Nb}_6$  phase and about 75% of the niobium deficient  $\text{Fe}_7\text{Nb}_6$  phase. This variation may just be a sampling phenomenon. Comparison of Figure 5.4 with Figure 5.1 shows that the microstructure of the as-received ferroniobium alloy is closest to that of the slowest cooled (10 K/min) DSC sample. As such, it is likely that the as-received alloy was subjected to a cooling cycle similar to that for the 10 K/min DSC sample.

## 5.4. Discussion

The DSC curves were compared with the iron-niobium phase diagram, in an attempt to rationalize the solidification process. Several equilibrium binary iron-niobium phase diagrams have been reported in literature (e.g., references [Bej93(1), Fer10, Oka93, Pau86, Sri94, Vob11]), showing significant differences from one another especially in the vicinity of the niobium-rich eutectic region. For instance, according to Paul et al. [Pau86] and Okamoto [Oka93], the niobium-rich eutectic reaction occurs at 1673 K (1400°C). On the other hand, Bejarano et al. [Bej93(1)], Srikanth et al. [Sri94] and Vob et al. [Vob11] put the niobium-rich eutectic at 1773 K (1500°C), 1758 K (1485°C) and 1781 K (1508°C), respectively. The most recent diagram is shown in Figure 5.5 [Vob11].

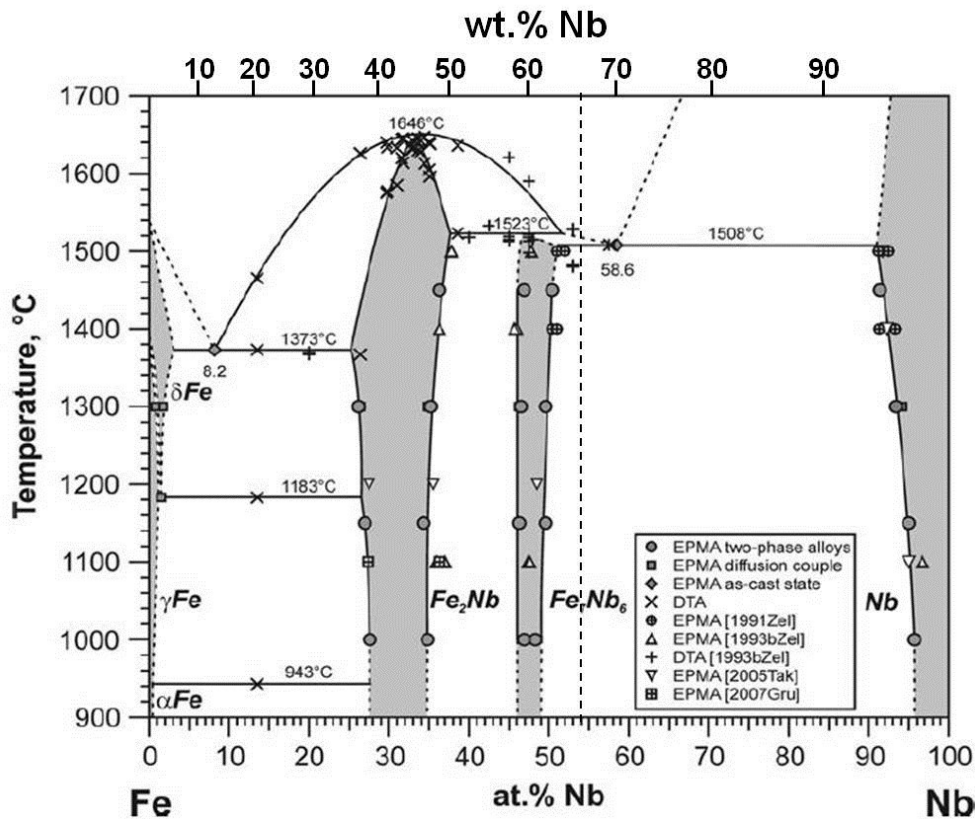


Figure 5.5: Iron-niobium binary phase diagram (redrawn/labeled) [Vob11].

It should be pointed out that the ferroniobium alloy is not a binary system; there are in excess of 3 wt.% impurities. However, if the alloy is approximated as a binary system, the alloy composition can be denoted by the vertical dashed line in Figure 5.5 (~ 66.2 wt.% niobium, based on the Cambridge Scientific compositions given in Table 4.1). Note that the liquidus lines and the solidus and solvus lines for the  $\text{Fe}_7\text{Nb}_6$  intermetallic near the eutectic are dashed, which is an indication of some degree of uncertainty. Based on this phase diagram, during equilibrium solidification the primary phase,  $\mu\text{-Fe}_7\text{Nb}_6$ , should start to form at ~ 1788 K (1515°C) and should contain ~ 61.5 wt.% niobium. As solidification proceeds, more  $\text{Fe}_7\text{Nb}_6$  will form and become slightly more niobium-rich. In addition, niobium will be rejected into the liquid phase until it reaches the eutectic composition, whereupon the liquid will transform via the eutectic reaction to a mixture of niobium-rich solid solution and  $\text{Fe}_7\text{Nb}_6$ . According to the phase diagram, the liquid should reach the eutectic composition at about 1781 K (1508°C) and at a composition of 70.2 wt.% niobium (58.6 at.% niobium). Under equilibrium solidification conditions, at the end of solidification, both the proeutectic  $\text{Fe}_7\text{Nb}_6$  intermetallic and the  $\text{Fe}_7\text{Nb}_6$  intermetallic formed during the eutectic reaction should have the same composition (63.4 wt.% niobium). Just after eutectic solidification, there should be about 40.8% of the eutectic and about 59.2% of the proeutectic  $\text{Fe}_7\text{Nb}_6$ , which corresponds to a total of 92.2%  $\text{Fe}_7\text{Nb}_6$  and 7.8% of the niobium-rich solid solution phase. The final amounts of these phases will change upon further cooling to room temperature, resulting in about 89.1% of  $\text{Fe}_7\text{Nb}_6$  and about 10.9% of the solid solution phase. A DSC cooling curve for this scenario should contain two exothermic peaks, one for the proeutectic reaction and one for the eutectic reaction. Recall that four exothermic peaks were obtained for all three DSC cooling rates. It is clear that the solidification behavior cannot be explained based only on the diagram shown in Figure 5.5.

It is conceivable that the diagram in Figure 5.5 is not entirely correct; as mentioned above, several of the transformation lines are dashed. In addition, the presence of impurities can cause shifting of the transformation lines. One possibility is that the liquidus line bordering the  $\text{Fe}_2\text{Nb} + \text{liquid}$  region could be extended further to the right (a more niobium-rich composition) so that the alloy passes through the  $\text{Fe}_2\text{Nb} + \text{liquid}$  region during solidification. This would add a third exothermic peak to any DSC cooling curve, but would not account for the fourth peak

One of the iron-niobium phase diagrams in the literature incorporates metastable phases and is shown in Figure 5.6 [Bej93(1)]. The diagram in Figure 5.6b is just a magnified view of the niobium-rich eutectic region in Figure 5.6a. The dashed vertical line (labelled A) in Figure 5.6b represents the overall composition of the ferroniobium alloy. Note that the  $\mu\text{-Fe}_{21}\text{Nb}_{19}$  phase in Figure 5.6 is the same as the  $\mu\text{-Fe}_7\text{Nb}_6$  phase in Figure 5.5 and there is an additional metastable phase,  $\text{Fe}_2\text{Nb}_3$ . (To avoid confusion and to maintain consistency,  $\mu\text{-Fe}_{21}\text{Nb}_{19}$  and  $\mu\text{-Fe}_7\text{Nb}_6$  will henceforth be referred to as  $\text{Fe}_7\text{Nb}_6$ .)

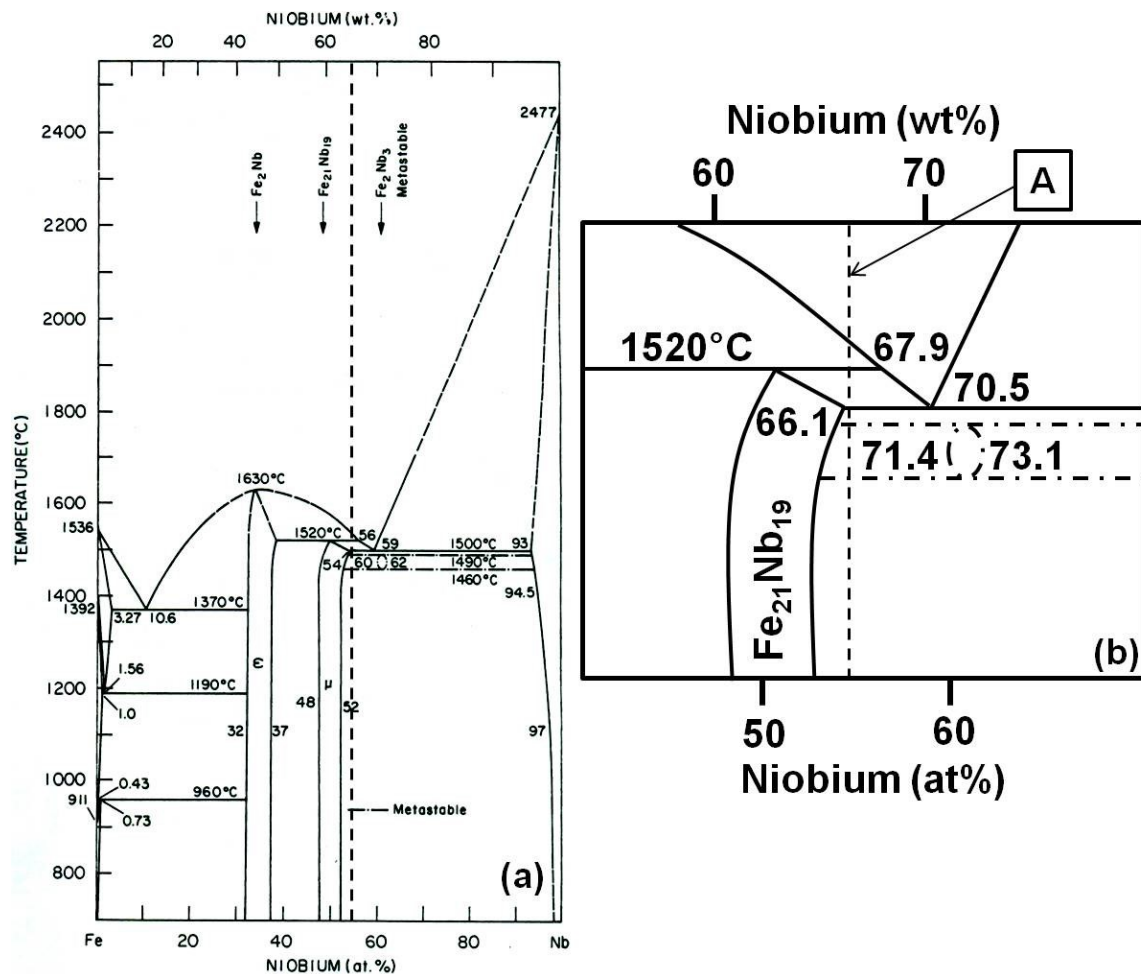


Figure 5.6: a) Iron-niobium binary phase diagram showing the metastable Fe<sub>2</sub>Nb<sub>3</sub> phase [Bej93(1)]. b) Magnified view of the niobium-rich eutectic region (compositions are given in wt.% and at.%).

According to the authors in [Bej91], Fe<sub>2</sub>Nb<sub>3</sub> forms metastably at slow cooling rates with the aid of certain impurities. Fe<sub>2</sub>Nb<sub>3</sub> has been reported in differential thermal analysis (DTA) studies; it forms on cooling at 1763 K (1490°C) and then decomposes at 1733 K (1460°C) [Bej91]. Vellios et al. [Vel07] also identified Fe<sub>2</sub>Nb<sub>3</sub>, indicating that its formation depends on the solidification rate and impurities as well. Based on Figure 5.6, upon equilibrium cooling from the liquid (line A in Figure 5.6b), there are two proeutectic reactions (Fe<sub>2</sub>Nb from the liquid and then the formation of

$\text{Fe}_7\text{Nb}_6$  from the liquid and  $\text{Fe}_2\text{Nb}$  at 1793 K (1520°C) via a peritectic reaction), one eutectic reaction (liquid transforming to  $\text{Fe}_7\text{Nb}_6$  and the niobium-rich solid solution), one peritectoid reaction ( $\text{Fe}_7\text{Nb}_6$  and the niobium-rich solid solution transforming to  $\text{Fe}_2\text{Nb}_3$ ) and one eutectoid reaction ( $\text{Fe}_2\text{Nb}_3$  transforming to  $\text{Fe}_7\text{Nb}_6$  and the niobium-rich solid solution). These reactions would give rise to five exothermic peaks in a DSC curve. Again, this does not correlate with the four peaks observed for the DSC curves in this work; however, this discrepancy can be explained in the following paragraph.

In this analysis, the DSC curve corresponding to the 10 K/min cooling rate will be considered and compared with the phase diagram in Figure 5.6b. There are two reasons for using the 10 K/min sample: 1) This cooling rate is the slowest studied and, as such, will be closest to the condition for equilibrium cooling, *i.e.*, closest to the phase diagram. 2) This cooling rate produced a microstructure closest to that observed for the as-received ferroniobium alloy. With reference to the DSC results, upon cooling of the liquid from 1873 K (1600°C), the first exothermic peak (peak 4) starts to appear at about 1833 K (1560°C). This corresponds to the first proeutectic reaction and the formation of  $\text{Fe}_2\text{Nb}$ . This process is completed by about 1816 K (1543°C), which corresponds to the formation of the second proeutectic phase ( $\text{Fe}_7\text{Nb}_6$ ); all the  $\text{Fe}_2\text{Nb}$  is consumed via a peritectic reaction (peak 3).  $\text{Fe}_7\text{Nb}_6$  continues to form over a fairly wide temperature range, *i.e.*, from 1816 K to 1782 K (1543°C to 1509°C). At about 1782 K (1509°C) the eutectic reaction begins (peak 2) and any remaining liquid is transformed to  $\text{Fe}_7\text{Nb}_6$  and the niobium-rich solid solution phase. The eutectic reaction appears to extend over a fairly wide temperature range, *i.e.*, from 1782 K (1509°C) to about 1748 K (1475°C); however, there appears to be a slight shoulder in the eutectic peak, which corresponds to the peritectoid reaction (some of the eutectic  $\text{Fe}_7\text{Nb}_6$  and niobium-rich solid solution transforms to the metastable  $\text{Fe}_2\text{Nb}_3$  phase). A shoulder (labelled

on Figure 5.3) appears, and not a separate peak, because the two peaks overlap due to the small temperature difference between the eutectic and peritectoid reactions. At about 1748 K (1475°C), the eutectoid reaction starts (finishes at about 1725 K (1452°C)) and  $\text{Fe}_2\text{Nb}_3$  transforms to  $\text{Fe}_7\text{Nb}_6$  and niobium-rich solid solution.

The final microstructures for the 10 K/min DSC sample (Figure 5.4a and 5.4d) and the as-received sample (Figure 5.1) are quite similar and consist of a large amount of eutectic microstructure (~45% of the total microstructure). There are also two distinct two-phase regions, a coarser microstructure surrounding a finer microstructure (e.g., see Figure 5.1b). The coarser two-phase region corresponds to the eutectic microstructure, while the finer two-phase region corresponds to  $\text{Fe}_7\text{Nb}_6$  and niobium-rich solid solution that has formed from eutectoid decomposition of  $\text{Fe}_2\text{Nb}_3$ . Note that  $\text{Fe}_7\text{Nb}_6$  formed via the eutectic reaction exhibits brighter contrast in the BSE images, which means that it is niobium-rich relative to the proeutectic  $\text{Fe}_7\text{Nb}_6$  or the  $\text{Fe}_7\text{Nb}_6$  which forms during the eutectoid reaction. The latter two forms of  $\text{Fe}_7\text{Nb}_6$  exhibit similar contrast and therefore have similar compositions. The difference in composition can be explained using the phase diagram in Figure 5.6b. The proeutectic  $\text{Fe}_7\text{Nb}_6$  forms initially with a composition of ~62.5 wt.% niobium (50 at.% niobium).  $\text{Fe}_7\text{Nb}_6$  becomes more enriched in niobium as solidification proceeds, but unlikely reaches the equilibrium composition when the eutectic reaction starts due to limited solid state diffusion. As such, proeutectic  $\text{Fe}_7\text{Nb}_6$  is slightly niobium deficient.  $\text{Fe}_7\text{Nb}_6$  that forms during the eutectic reaction will be niobium-rich, *i.e.* ~66.1 wt.% niobium (54 at.% niobium) relative to proeutectic  $\text{Fe}_7\text{Nb}_6$ , which accounts for the brighter contrast  $\text{Fe}_7\text{Nb}_6$  regions in Figure 5.1b and Figure 5.4d.  $\text{Fe}_7\text{Nb}_6$  which forms during eutectoid decomposition will be niobium deficient, *i.e.* ~64.3 wt.% niobium (52 at.% niobium).

Further support for the proposed solidification process is provided by the TEM microstructure in Figure 5.2 and Figure 4.14. The niobium-rich  $\mu$ -Fe<sub>7</sub>Nb<sub>6</sub> intermetallic (formed from the eutectic reaction) is heavily faulted, while the proeutectic Fe<sub>7</sub>Nb<sub>6</sub> (niobium deficient) contains a much lower concentration of faults. The presence or absence of faults can be justified by the temperature of formation. At lower temperatures the rate of diffusion is relatively low which would favor the formation of faulted structures; as such, stacking faults or twins are more prominent in Fe<sub>7</sub>Nb<sub>6</sub> formed at lower temperature (eutectic reaction) compared with proeutectic Fe<sub>7</sub>Nb<sub>6</sub> formed at higher temperatures (proeutectic reaction).

Figure 5.7 shows the effect of cooling rate on the onset temperature. The straight lines have been extrapolated back to 0 K/min. The purpose of this approach is to eliminate the effect of cooling rate and to obtain the transformation temperature for the near equilibrium condition. Based on the above analysis, the niobium-rich eutectic region of the commercial ferroniobium (iron-niobium with 3 wt.% impurities) phase diagram is redrawn in Figure 5.8. This diagram is very similar to the one in Figure 5.6b, with the main differences being the positions of the transformation temperatures. It should be noted that the diagram in Figure 5.8 is not being proposed as the pure iron-niobium binary diagram, but is a modified version that includes the effect of impurities.

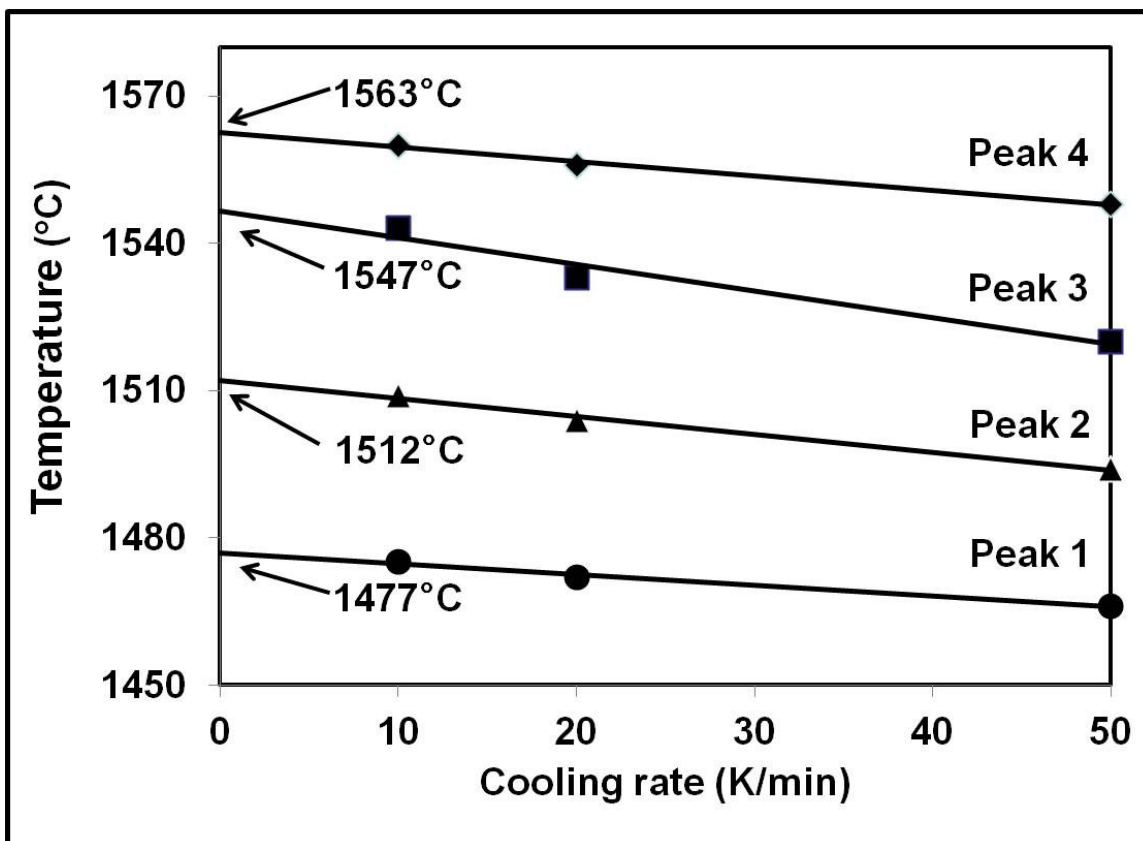


Figure 5.7: Onset temperature for DSC peaks versus cooling rate. Data is extrapolated to 0 K/min.

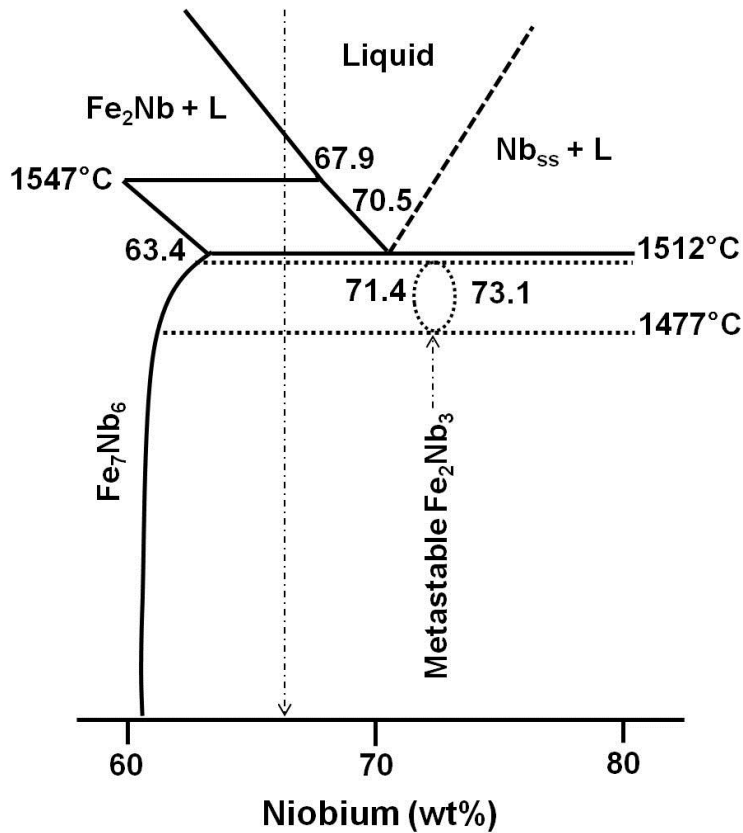


Figure 5.8: Proposed niobium-rich eutectic region of commercial ferroniobium (iron-niobium with 3 wt.% impurities) phase diagram.

In practical terms, solidification does not occur under equilibrium conditions; often the rate of solidification is too fast to allow for significant solid state diffusion. As such, solidification behavior can be approximated by the solidification model, where no diffusion is assumed in the solid state, perfect mixing occurs in the liquid and local equilibrium is achieved at the interface [Por92]. In addition, a certain degree of undercooling is required for the liquid to solidify. Based on these assumptions, the amount of solid formed before the eutectic reaction (proeutectic  $\mu$ -Fe<sub>7</sub>Nb<sub>6</sub>) is calculated using [Por92]:

$$X_s = kX_o(1 - f_s)^{(k-1)} \quad \text{Equation 5.1}$$

The amount of liquid remaining, which then transforms via the eutectic reaction, is given by [Por92]:

$$X_l = X_o (f_l)^{(k-1)} \quad \text{Equation 5.2}$$

$X_o$  is the overall composition of the alloy,  $X_s$  and  $X_l$  are the compositions of the solid and liquid, respectively,  $f_s$  and  $f_l$  are the phase fractions of solid and liquid, respectively, and  $k$  is the partition coefficient and is equal to  $X_s/X_l$ .  $X_s$  and  $X_l$  vary with temperature such that as temperature drops both quantities become more enriched in niobium. Eutectic fractions were calculated for 3 different eutectic temperature depressions (-10, -20 and -30 K) using Equations 5.1 and 5.2. This was done by extending the proeutectic intermetallic solidus line and the liquidus line of the proposed iron-niobium phase diagram, as illustrated in Figure 5.9.

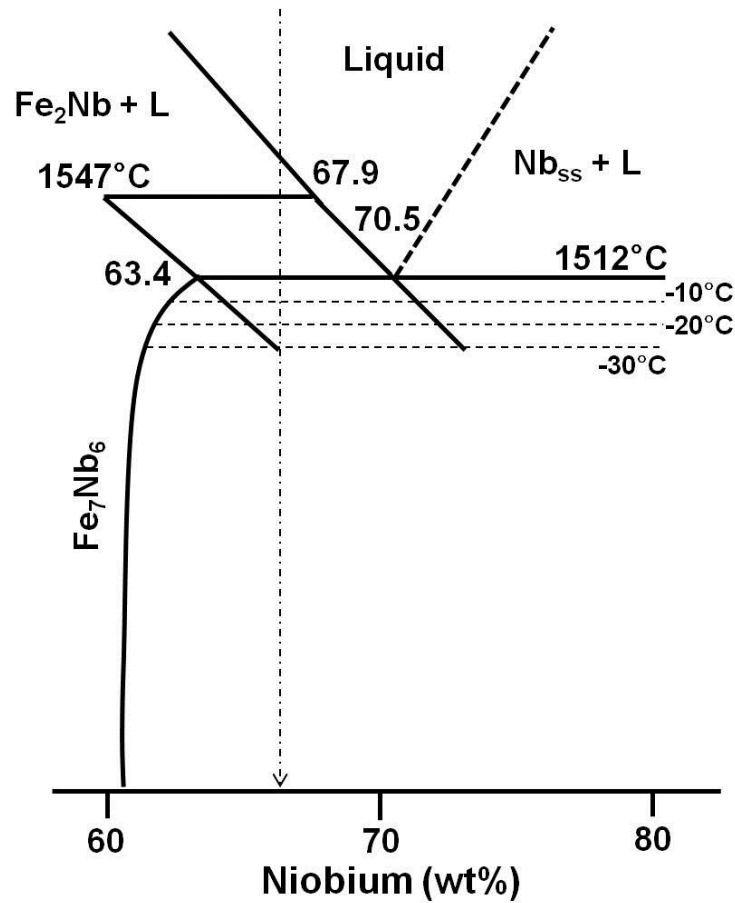


Figure 5.9: Approximate extension of liquidus and solidus (proeutectic intermetallic) lines for Scheil calculations. (The metastable lines and region are omitted for simplicity)

The compositions of the liquid and proeutectic intermetallic were calculated for the three eutectic temperature depressions and were then incorporated in Equation 5.2 to give the fraction of liquid that transformed to the eutectic microstructure. As an example, for the 10 K depression  $X_s$  and  $X_l$  are 64.3 wt.% and 71.2 wt.%, respectively (52 at.% and 59.8 at.%). The original composition of the alloy  $X_o$  is 66.2 wt.% (54.1 at.%). If these values are incorporated into Equation 5.2, a liquid phase fraction ( $f_l$ ) of 0.46 is obtained. This amount transforms to the eutectic microstructure (Table 5.3). Similar calculations were done for the 20 K and 30 K eutectic temperature depressions; these

are indicated by horizontal dotted lines below the eutectic temperature in Figure 5.9. The fraction of eutectic microstructure formed is affected by the amount of eutectic temperature depression, *i.e.*, increasing the amount of depression decreases the amount of eutectic microstructure. This effect is shown in Table 5.3 for various amounts of eutectic temperature depressions.

Table 5.3: Volume fraction of eutectic microstructure at different temperatures

<b>Temperature K (°C)</b>	<b>Scheil</b>	<b>Equilibrium (new proposed phase diagram)</b>	<b>As-received sample at room temperature (quantitative metallography)</b>
1785 K (1512°C)	0.53	0.39 at 1785 K (1512°C)	0.41
1775 K (1502°C) (10 K eutectic depression)	0.46		St Dev: 0.046
1765 K (1492°C) (20 K eutectic depression)	0.40		
1755 K (1482°C) (30 K eutectic depression)	0.35		

St Dev: standard deviation

Table 5.3 also shows eutectic fractions calculated for equilibrium cooling and determined experimentally for the actual ferroniobium alloy. An eutectic temperature depression between 10 K and 20 K (closer to 20 K) gives a eutectic fraction close to that observed for the ferroniobium alloy. The Scheil calculations agree reasonably well with the DSC results. The 10 K/min DSC sample (cooling), which had a microstructure closest to that of the as-received ferroniobium alloy,

was composed of ~ 55% proeutectic Fe<sub>7</sub>Nb<sub>6</sub> and ~ 45% eutectic microstructure. The eutectic reaction occurred at 1765 K (1492°C) or a eutectic temperature depression of 20 K for the commercial alloy.

## 5.5. Conclusions

The phase evolution mechanism in a commercial grade ferroniobium alloy was studied using electron microscopy and differential scanning calorimetry. The ferroniobium alloy contained nearly 3 wt.% impurities and two phases. The primary phase was the  $\mu$  intermetallic phase (Fe<sub>7</sub>Nb<sub>6</sub>) with significant amounts (~ 10% by volume) of the niobium solid solution phase (iron in solution). On the basis of DSC results, the  $\mu$  phase (Fe<sub>7</sub>Nb<sub>6</sub>) is formed at three different temperatures during solidification, *i.e.*, during proeutectic, eutectic and eutectoid reactions. A modified iron-niobium phase diagram (accounting for impurities in the commercial ferroniobium alloy) is proposed with the aid of the DSC results. Solidification of the alloy system was also modeled using the Scheil solidification model, which showed that the as-received ferroniobium alloy likely formed with a cooling rate close to 10 K/min having eutectic depression of 20 K and was corroborated by quantitative metallography.

## 5.6. References

Abr06(1): S. Abraham, R. Klein, R. Bodnar and O. Dremailova. Formation of coarse particles in steel as related to ferroalloy dissolution thermodynamics. Part 1: ferroalloy melting, dissolution and microstructures. Material Science and Technology (MS & T), Cincinnati, Ohio, October 2006.

Abr06(2): S. Abraham, R. Klein, R. Bodnar and O. Dremailova. Formation of coarse particles in steel as related to ferroalloy dissolution thermodynamics. Part II: crystallographic study of ferroalloys and coarse particles. Material Science and Technology (MS & T), Cincinnati, Ohio, October 2006.

Bej91: J. M. Z. Bejarano, S. Gama, C. A. Ribeiro, G. Effenberg and C. Santos. On the existence of the Fe<sub>2</sub>Nb<sub>3</sub> phase in the Fe-Nb system Zeitschrift für Metallkunde, 1991, 82, 615–620.

Bej93(1): J. M. Z. Bejarano, S. Gama, C. A. Ribeiro and G. Effenberg. The iron-niobium phase diagram. Zeitschrift für Metallkunde, 1993, 84, 3, 160–164.

Car00: P. A. Carvalho, H. S. D. Haarsma, B. J. Kool, P. M. Bronsveld, J. Th. De Hosson and M. De Hosson. HRTEM study of Co<sub>7</sub>W<sub>6</sub> and its typical defect structure, Acta Materialia. 2000, 48, 2703-2712.

Car01: P. A. Carvalho and JTh. De Hosson. Stacking faults in the Co<sub>7</sub>W<sub>6</sub> isomorph of the  $\mu$  phase. Scripta Materialia, 2001, 45, 333-340.

Che87: Z. Chen, M. H. Loretto and R. C. Cochrane. Nature of large precipitates in titanium containing HSLA Steels. Materials Science and Technology, 1987, 3, 836-844.

Cos92: G. J. R. Costa. Niobium ferroalloy and niobium additive for steels, cast irons and other metallic alloys. Patent WO/1992/022675.

Cra00: A. J. Craven, K. He, L. A. J. Garvie and T. N. Baker. Complex heterogeneous precipitation in titanium-niobium microalloyed Al-killed HSLA steels-II. Non-Titanium based precipitates. *Acta Materialia*, 2000, 48, 3869-3878.

Del92: J. Delamare, D. Lemarchand and P. Vigier. Transmission electron microscopy study of the  $\mu$  phase in the Fe-Nd-Al system. *Journal of Magnetism and Magnetic Materials*, 1992, 104, 7, 1092-1093.

Eng92: T. A. Engh. *Principles of Metal Refining*. Oxford University Press, New York, US, 1992.

Fer10: E. B. Ferreira, M. L. Lima and E. D. Zanotto. DSC method for determining the liquidus temperature of glass-forming systems. *Journal of American Ceramic Society*, 2010, 93, 11, 3757-3763.

Gla97: T. Gladman. *The Physical Metallurgy of Microalloyed Steels*. The University Press Cambridge, UK, 1997.

Har71: E. M. Harold (ed.) *The Making, Shaping and Treating of Steel*. United States Steel, 1971.

Kum98: K. K. C. Kumar, I. Ansara and P. Wollants. Sublattice modelling of the  $\mu$  phase, *Calphad*, 1998, 22, 3, 323-34.

Man07: H. Mandar, T. Uustare, J. Aarik, A. Tarre and A. Rosental. Characterization of asymmetric rhombohedral twins in epitaxial – Cr<sub>2</sub>O<sub>3</sub>, thin films by X-ray and electron diffraction. *Thin Solid Films*, 2007, 515, 11, 4570-4579.

Mck82: M. J. Mckelvy, A. R. R. Smith and L. Eyring. High resolution electron microscope analysis of {100} twinning in  $\beta$  – rhombohedral boron. *Journal of Solid State Chemistry*, 1982, 44, 3, 374-381.

- Men99: R. Mendoza, J. Huante, M. Alanis, C. Gonzalez-Rivera and J. A. Juarez-Islas. Slab cracking after continuous casting of API 5L X-70 grade steel for pipeline sour gas application. *Iron and Steelmaking*, 1999, 26, 3, 205-209.
- Oka93: H. Okamoto. Fe-Nb (Iron-Niobium). *Journal of Phase Equilibria*, 1993, 14, 5, 650-652.
- Pan10: M. M. Pande, M. Guo, X. Guo, D. Geysen, S. Devisscher, B. Blanpain et al. Impurities in commercial ferroalloys and its influence on steel cleanliness. In the proceedings of the Twelfth International Ferroalloys Congress Sustainable Future. Helsinki, Finland, 2010.
- Pau86: E. Paul and L. J. Swartzendruber. The Fe-Nb (Iron-Niobium) System. *Bulletin of Alloy Phase Diagrams*, 1986, 7, 3, 248-254.
- Por92: D. A. Porter and K. E. Easterling. *Phase Transformations in Metals and Alloys*. Chapman and Hall, London, 1992.
- Pot01: R. M. Poths, R. L. Higginson and E. J. Palmiere. Complex precipitation behaviour in a microalloyed plate steel. *Scripta Materialia*, 2001, 44, 147-151.
- Rob84: W. Roberts. Recent innovations in alloy design and processing of microalloyed steels. Conference Proceedings of International Conference on Technology and Applications of HSLA Steels, Philadelphia, 3-6 October, 1983, American Society of Metals 1984.
- Sha13(1): S. J. Shah, H. Henein and D. G. Ivey. Microstructural characterization of ferrotitanium and ferroniobium. *Materials Characterization*, 2013, 78, 96-107.
- Sri94: S. Srikanth and A. Petric. A thermodynamic evaluation of the Fe-Nb system. *Zeitschrift für Metallkunde*, 1994, 85, 3, 164–170.

Ste79: L. Stenberg and S. Andersson. Electron microscope studies on a quenched Fe-Mo alloy, *Journal of Solid State Chemistry*, 1979, 28, 269-277.

Vel07: N. Vellios and P. Tsakiroopoulos. The role of Fe and Ti additions in the microstructure of Nb-18Si-5Sn silicide-based alloys. *Intermetallics*, 2007, 15, 1529-1537.

Vob11: S. Vob, M. Palm, F. Stein and D. Raabe. Phase equilibria in the Fe-Nb system. *Journal of Phase Equilibria and Diffusion*, 2011, 32, 97–104.

Yua09: S. Q. Yuan and G. L. Liang. Dissolving behaviour of second phase particles in Nb-Ti microalloyed steel. *Materials Letters*, 2009, 63, 2324-2326.

Zhu90: J. Zhu and H. Q. Ye. On the microstructure and its diffraction anomaly of the  $\mu$  phase in superalloys, *Scripta Metallurgica et Materialia*, 1990, 24, 1861-1866.

## Chapter 6: Analysis of Coarse Niobium-Rich Particles in the Steel

### 6.1. Introduction

Ferroniobium is added to steel as a source of niobium to improve the mechanical properties, by: 1) forming finely dispersed NbC and/or Nb(C,N) precipitates, 2) controlling the grain size and 3) solute strengthening [Gla97, Har71]. However, several studies have shown the presence of coarse niobium-rich particles in the steel, which can have an adverse effect on the mechanical properties [Abr06(1), Abr06(2), Che87, Cra00, Men99, Pot01, Tia07, Yua09, Zho96, Zhu07, Zhu08]. Two schools of thought exist regarding the origin of such particles. Some researchers believe that the particles are from undissolved phases in the ferroniobium [Abr06(1), Abr06(2), Men99], while others believe that the particles are precipitated at high temperatures during solidification of the steel [Che87, Yua09, Zho96]. An extensive study of the ferroniobium alloy has already been done and reported in Chapters 4 and 5 of this thesis. In this chapter, a study is done to evaluate the two schools of thought by investigating different steels with niobium-rich particles and doing thermodynamic calculations. The three main sections in this chapter are as follows:

- a) Niobium (in the form of ferroniobium) is added to a steel to investigate the presence of any undissolved, niobium-rich solid solution phase.
- b) Steel samples with coarse niobium-rich particles are studied to identify their exact nature.
- c) Thermodynamic calculations are done to determine the precipitation temperature for NbC particles.

## **6.2. Experimental Methods**

Two steel samples with different chemistries were used for experimental purposes in this chapter. The steel samples and their chemistries were provided by Evraz Inc. NA. Due to confidentiality issues, exact compositions of these steels are not provided; rather a range of compositions is given as shown in Table 6.1. Steel A has significantly more carbon as compared with Steel B. Steel A is used for niobium addition experiments, since it has a low amount of niobium relative to Steel B.

Table 6.1: Composition range of steels studied (provided by Evraz)

<b>Elements</b>	<b>Steel A (wt.%)</b>	<b>Steel B (wt.%)</b>
C	0.2-0.3	0.05-0.07
Mn	1.2-1.4	1.2-1.5
S	< 0.003	< 0.003
P	0.007-0.009	0.008-0.015
Si	0.2-0.3	0.15-0.2
Cu + Ni + Cr	0.5-0.6	0.3-0.4
V	0.001-0.003	0.0005-0.0015
Nb	< 0.0015	0.06-0.07
Mo	0.02-0.03	0.03-0.04
Sn	0.007-0.009	0.007-0.01
Al	0.04-0.05	0.02-0.03
Ca	0.002-0.003	0.002-0.004
Ti	0.002-0.003	0.01-0.02
N	0.007-0.008	0.007-0.008
O	0.005-0.006	0.002-0.003
Ce	< 0.001	< 0.001
Pb	< 0.001	< 0.001
As	< 0.005	< 0.005
Zn	< 0.005	< 0.005

A VEGA-3 (Tescan) SEM was used for imaging and EDX analysis. A JAMP-9500F Auger microprobe was used for Auger analysis. The sample preparation technique and operating conditions for SEM and Auger analysis have already been described in Section 3.3 of the thesis.

TEM samples were prepared using a Hitachi NB5000 dual beam FIB-SEM. A JEOL JEM-2010 TEM was used for both dark field (DF) and bright field (BF) imaging along with selected area diffraction (SAD). Operating conditions have been discussed in detail in Section 3.4 of the thesis.

For XRD analysis, a Rigaku rotating anode (RU-200B) XRD system with a copper anode was used; the details are provided in Section 3.5.

## **6.3. Results and Discussion**

### **6.3.1. Ferroniobium Additions to Steel A**

For this set of experiments Steel A was used, with a niobium content less than 0.0015 wt.% (Table 6.1). Figure 6.1 shows low and high magnification SEM BSE images of steel samples where 1 wt.% niobium was added in the form of ferroniobium. The steels were held at 1873 K (1600°C) for 6 minutes (Figure 6.1a and b), 20 minutes (Figure 6.1c and d) and 40 minutes (Figure 6.1e and f) after the addition of ferroniobium.

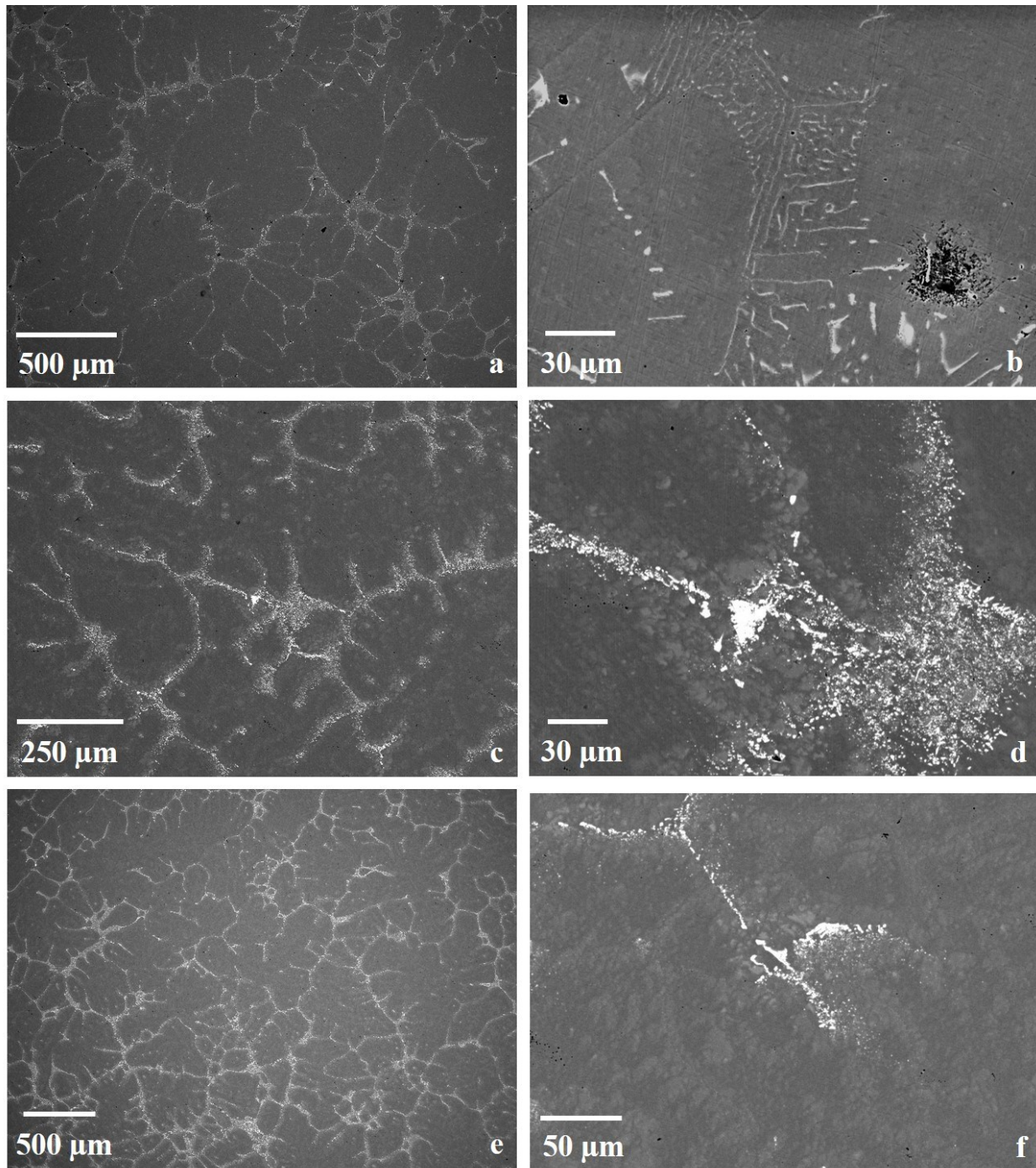


Figure 6.1: SEM BSE images of Steel A with 1 wt.% niobium added at 1873K (1600°C). a) and b) Ferroniobium dissolution time of 6 minutes; c) and d) dissolution time of 20 minutes; and e) and f) dissolution time of 40 minutes.

However, the melting conditions used in these experiments is different from the industrial practise, i.e. significant stirring in case of small laboratory scale induction melting as compared to large scale industrial practice. In order to compensate this 1 wt.% niobium was added instead of very small amounts (0.1 wt.%). Samples were removed from the center of the cross-section of crucible at the top, middle and bottom half of the melt, yielding three samples from each experiment.

The dark areas in the images are iron-rich and the white areas are niobium-rich. On the basis of size, the niobium-rich particles can be divided into two groups. The finer particles (present in abundance) average around 2 microns in size and the coarser particles (fewer) average around 20 microns in size. EDX analysis performed on the niobium-rich particles showed a small amount of titanium and iron (3-4 wt.% combined). The fundamental issue is whether the niobium-rich particles are the undissolved niobium-rich, solid solution phase from ferroniobium or niobium-rich particles that have precipitated in the steel at high temperatures. TEM analysis of the niobium-rich regions was done.

The steel sample with a ferroniobium dissolution time of 6 minutes was chosen for TEM study. This was the shortest dissolution time and should, therefore, provide the greatest likelihood for finding the undissolved niobium-rich solid solution phase. Figure 6.2a shows a TEM BF image from an area that contains two niobium-rich regions surrounded by the iron-rich matrix. Figure 6.2b shows a higher magnification view of the region indicated in Figure 6.2a. SAD patterns were taken from both regions (Figures 6.2c-e). The iron-rich region patterns were indexed to BCC alpha iron. The patterns from the niobium-rich regions could not be indexed to the niobium-rich solid solution phase. Instead they were indexed to NbC;  $Nb(C_xN_{1-x})$  is another possibility since it has the same crystal structure. NbC is more likely as there is significantly more carbon than nitrogen in Steel A (Table 6.1).

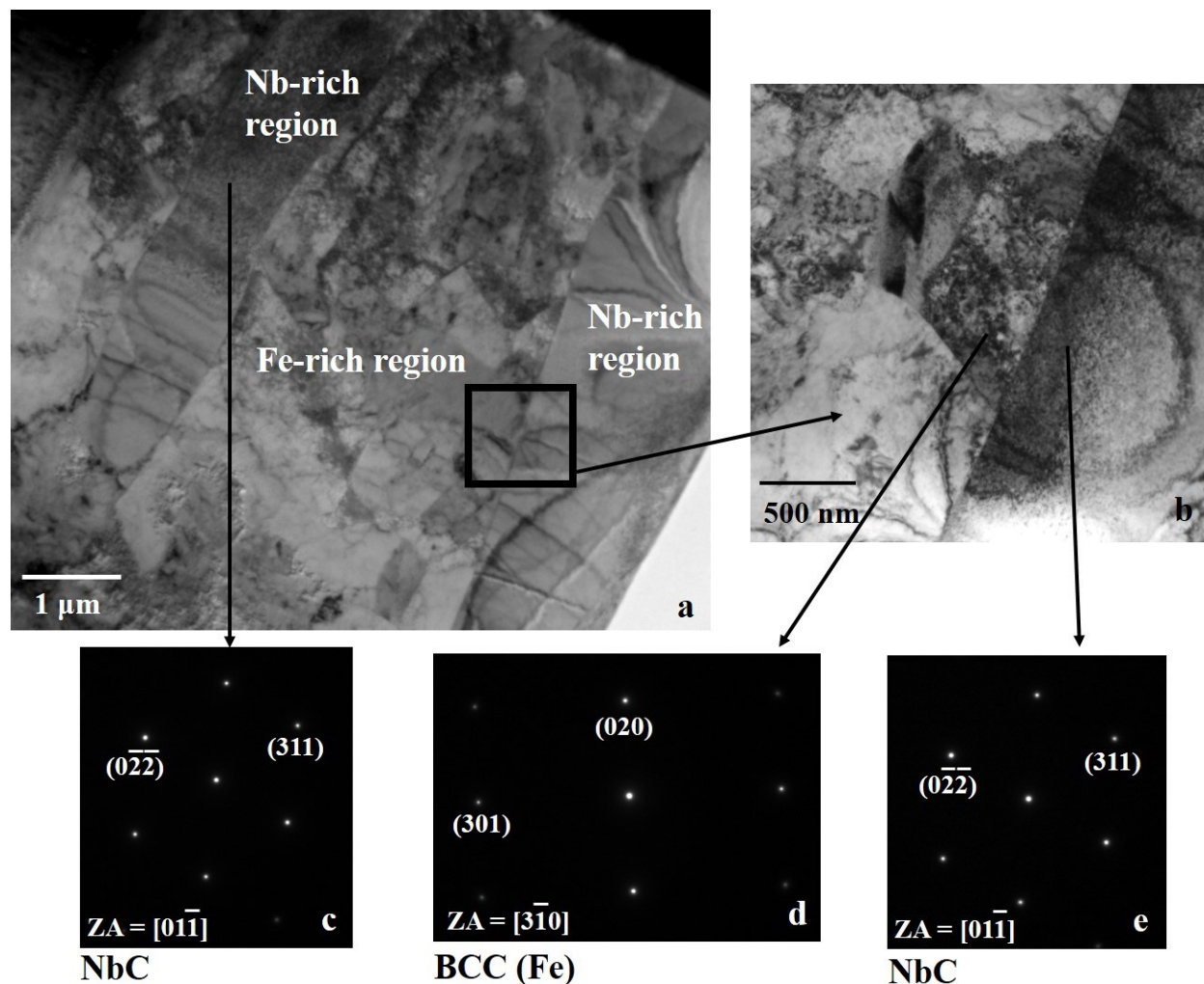


Figure 6.2: a) and b) Low and high magnification TEM BF images of steel samples with 1 wt.% niobium addition (dissolution time was 6 minutes). c) – e) SAD patterns from the iron-rich and niobium-rich regions respectively.

The TEM analysis showed that at least the smaller niobium-rich regions were precipitated carbides and not the niobium-rich solid solution phase (undissolved from the as-received ferroniobium). Further analysis was done using XRD. Figure 6.3 shows an XRD pattern for Steel A after the addition of 1 wt.% niobium (dissolution time of 6 minutes). The peaks can all be indexed to NbC

and BCC ferrite (majority phase). The results indicate that despite an excessive amount of niobium (1 wt.%) being added to the steel, all the ferroniobium phases dissolved in 6 minutes at 1873 K (1600°C), leaving no undissolved niobium-rich solid solution phase.

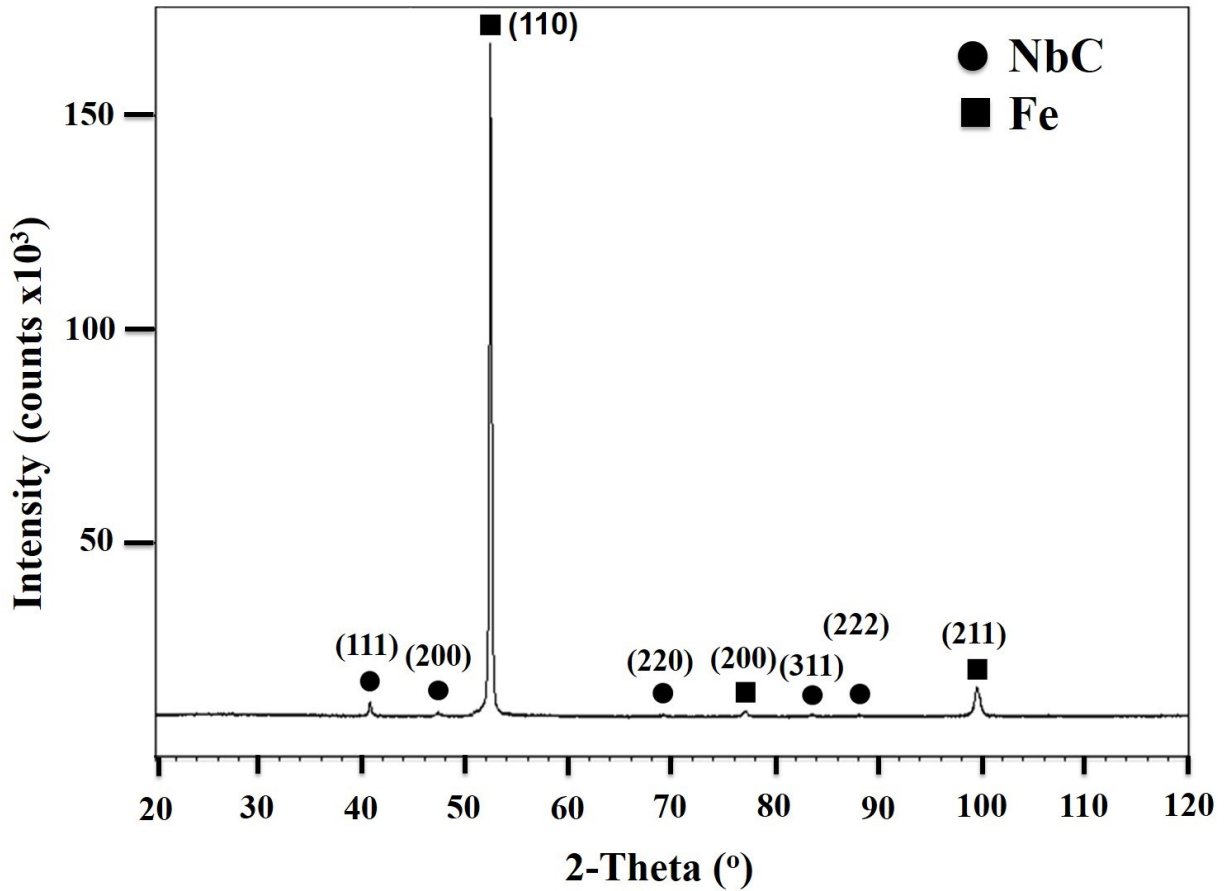


Figure 6.3: XRD pattern for Steel A with 1 wt.% niobium added (6 minutes dissolution time).

### 6.3.2. Characterization of Steel B for Coarse Niobium-Rich Particles

Samples with coarse niobium-rich particles (Steel B) were provided by Evraz; the composition is given in Table 6.1. Figures 6.4a and 6.4c show low magnification SEM BSE images of the steel samples. Coarse niobium-rich particles are indicated (black squares). Magnified images of these

particles are shown in Figures 6.4b and 6.4d. The coarse particles are present in the center line of the steel slab and have an adverse effect on the mechanical properties of the steel.

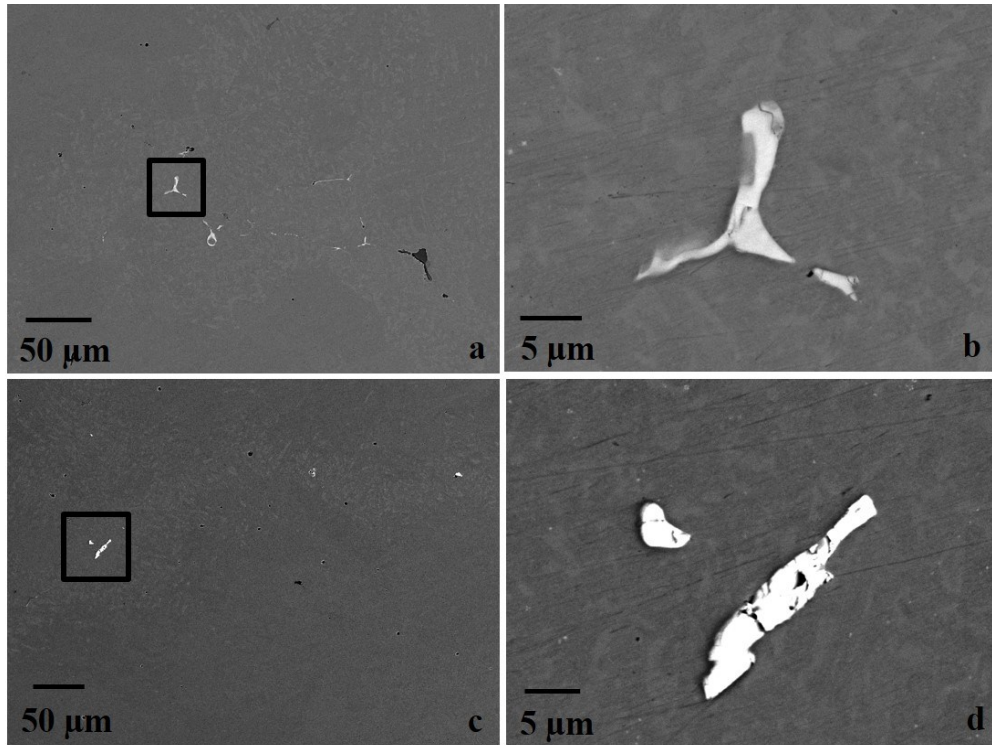


Figure 6.4: a) and c) Low magnification SEM BSE images of Steel B showing coarse niobium-rich particles. b) and d) Magnified SEM BSE images of the coarse niobium-rich particles (a) and (c), respectively.

An EDX line scan was done across two of the coarse niobium-rich particles shown in Figure 6.4d (Figure 6.5). In addition to niobium, small amounts of carbon, silicon and aluminum are present. Titanium and/or nitrogen are also present. The titanium L peaks overlap with the nitrogen K peak, so it is difficult to separate the two elements. However, given the low concentration of nitrogen in the steel, the peak is likely from titanium. Another line scan is shown in Figure 6.6; the results are

similar. Auger electron spectroscopy was utilized to confirm the EDX results and to separate the titanium signal from the nitrogen signal.

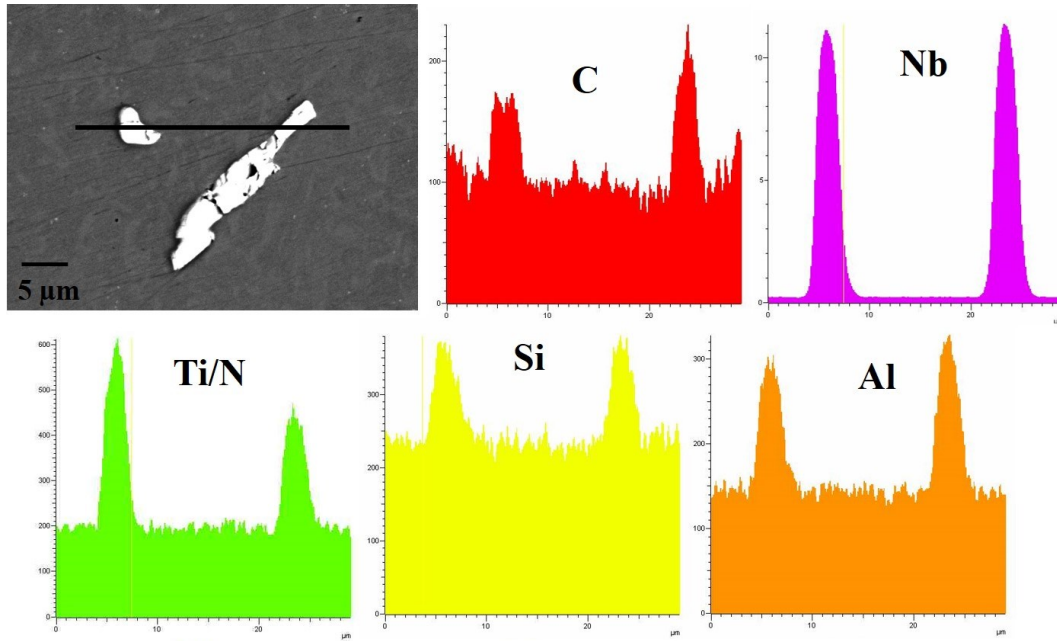


Figure 6.5: SEM EDX line scan across coarse niobium-rich particles in Figure 6.4d.

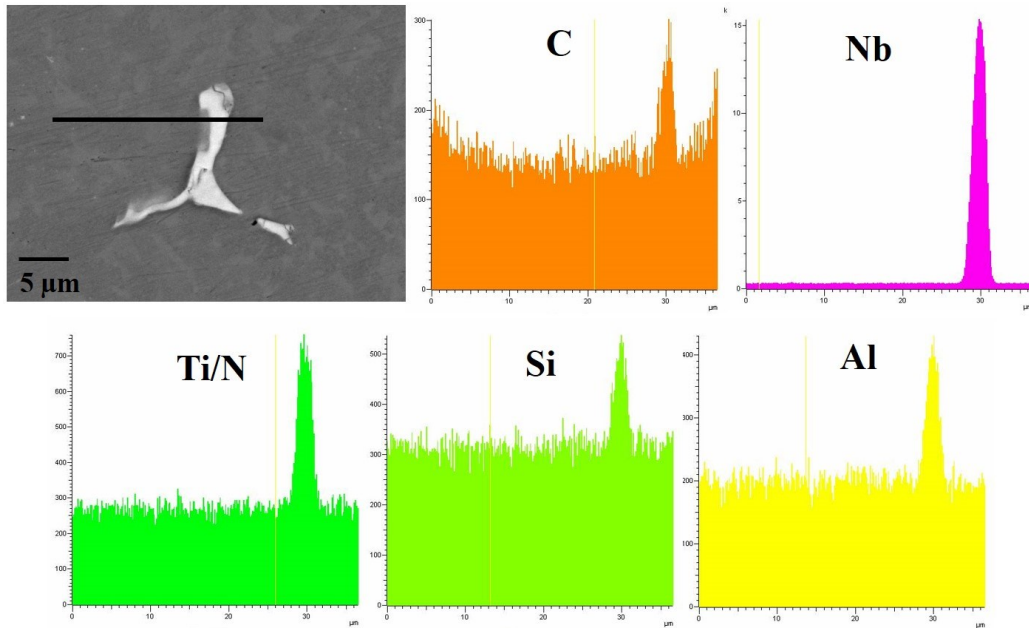
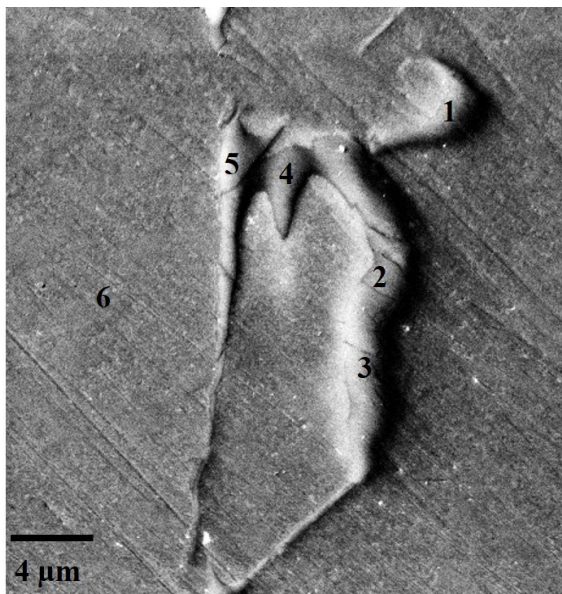


Figure 6.6: SEM EDX line scan across coarse niobium-rich particle in Figure 6.4b.

Auger electron spectroscopy (AES) was done on coarse niobium-rich particles from Steel B (Figure 6.7). The points shown in Figure 6.7 were chosen for analysis and include one point from the matrix (point 6). The compositions are tabulated in Figure 6.7 as well. The niobium-rich particles contain significant amounts of carbon and nitrogen and are, therefore, niobium carbonitrides ( $\text{Nb}(\text{C}_x\text{N}_{1-x})$ ) and not niobium carbides ( $\text{NbC}$ ). Oxygen is present across the surface and likely due to surface oxidation. Auger spectra for points 5 and 6 are shown in Figure 6.8 and 6.9, respectively. Comparison of these spectra, shows that the coarse particle are rich in niobium, carbon and nitrogen and the matrix is rich in iron.



Points	Composition (at%)				
	C	N	O	Fe	Nb
1	20.3	21.3	5.9	6	46.5
2	20.3	23.1	7.7	0	48.9
3	20.3	22.6	7.7	0	49.4
4	19.3	20.1	5.9	0	54.7
5	24.1	18.3	8.9	0	48.7
6	0	0	7.1	92.9	0

Figure 6.7: SEM SE image of Steel B showing niobium-rich particles as well as the iron-rich matrix. Composition analysis of the points shown was done through AES.

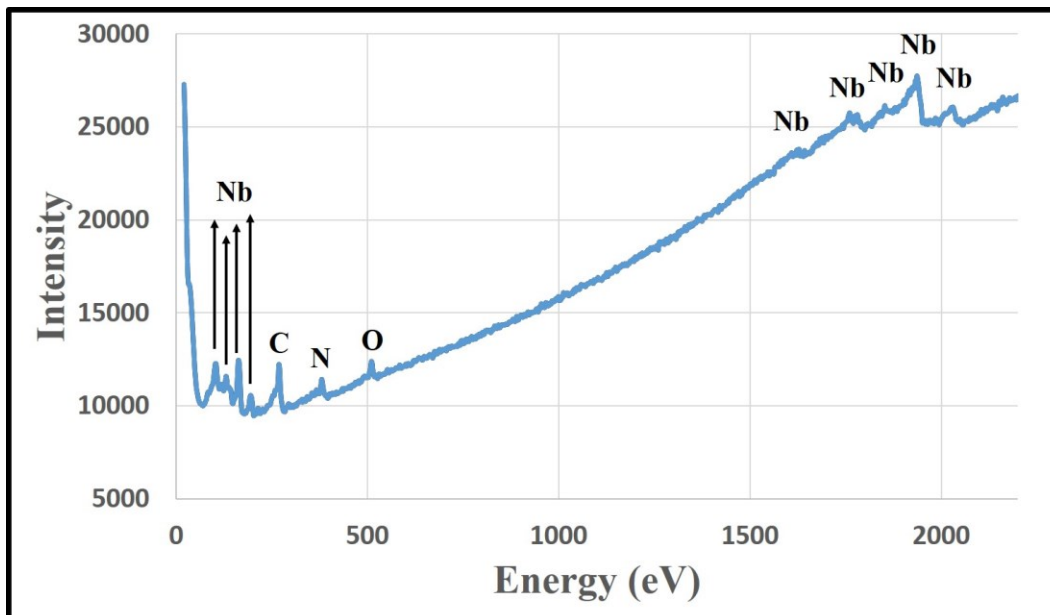


Figure 6.8: Auger spectrum for point 5 shown in Figure 6.7.

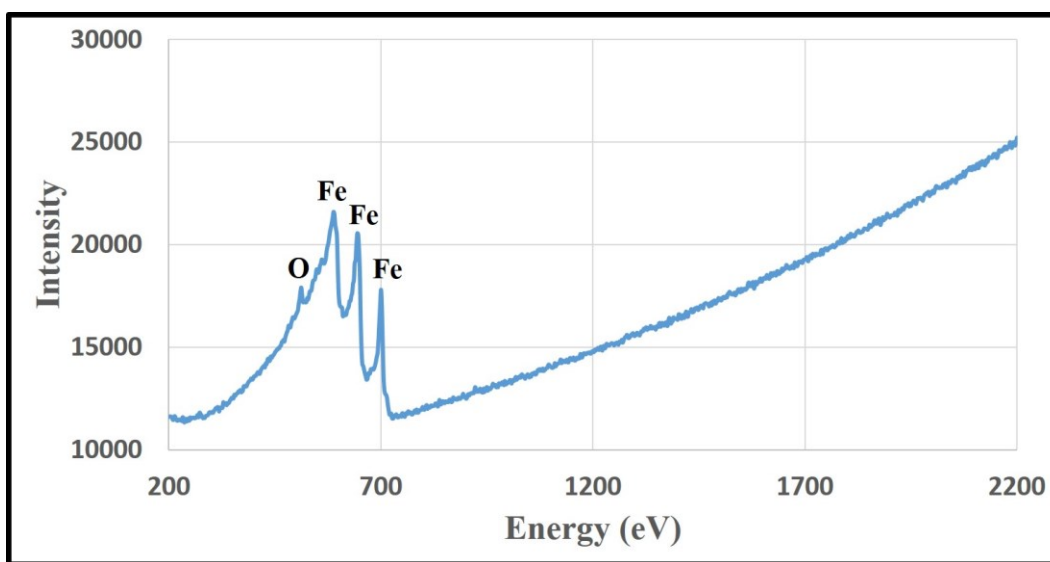


Figure 6.9: Auger spectrum for point 6 shown in Figure 6.7.

Elemental mapping was also done using AES for carbon, iron, nitrogen and niobium; the elemental distributions are shown in Figure 6.10. Carbon and nitrogen are clearly concentrated where niobium is present.

The combination of electron microscopy, XRD and SEM results clearly shows that the coarse niobium-rich particles are niobium-titanium carbonitrides and not the niobium-rich solid solution phase. However, precipitation of such particles is only possible at elevated temperatures in order to provide sufficient time to grow to sizes of 5-10  $\mu\text{m}$  (Che87). Thermodynamic calculations were done for Steel B to estimate the precipitation temperature for niobium-titanium carbonitrides.

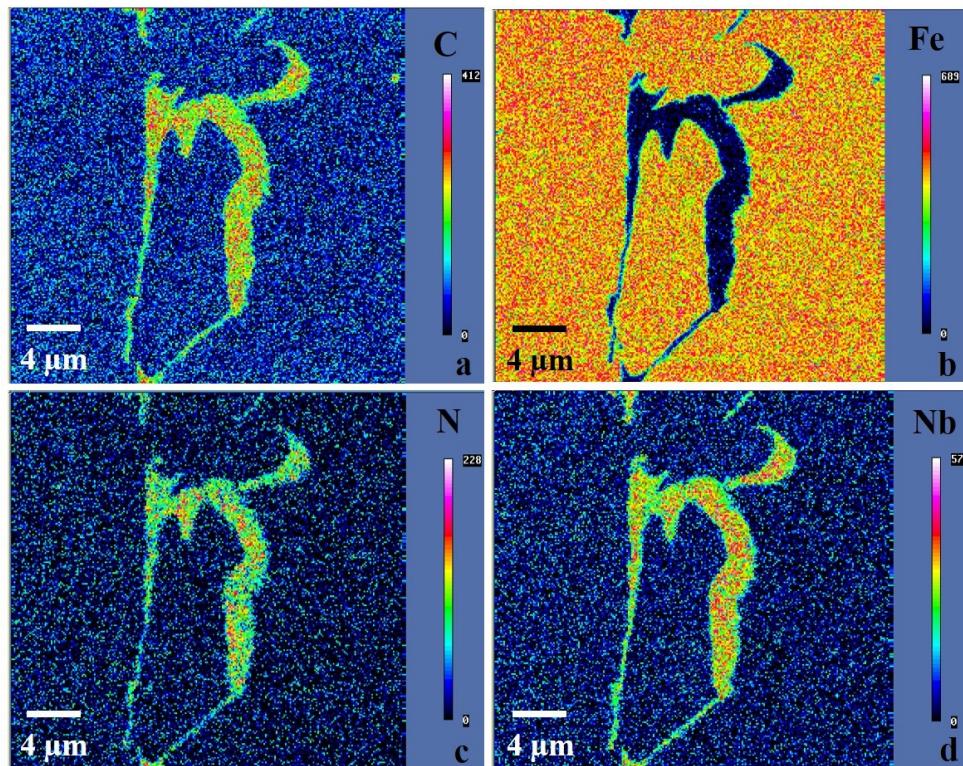


Figure 6.10: Auger mapping (carbon, nitrogen, iron and niobium) of the region shown in Figure 6.7.

### 6.3.3. Thermodynamic Calculations for Steel B

The chemistry of Steel B is provided in Table 6.1. For the thermodynamic calculations the specific chemistry of the steel was used. To simplify the calculations only carbon, niobium, titanium, nitrogen and iron were considered. Thermocalc software Version 5.0.4.75 and the database for steel and iron alloys (TCFE6) were used for thermodynamic calculations. Thermocalc software uses available thermodynamic information and performs a wide range of calculations, including those of interest in this work, *i.e.*, constituent phase diagrams and Scheil solidification calculations to study segregation issues.

Thermocalc software was used to construct the iron-niobium phase diagram based on a fixed amount of titanium, carbon and nitrogen (Steel B). Figure 6.11 shows the variation in NbC precipitation temperature with increasing niobium content. The two vertical lines show the range of niobium composition for steel B.

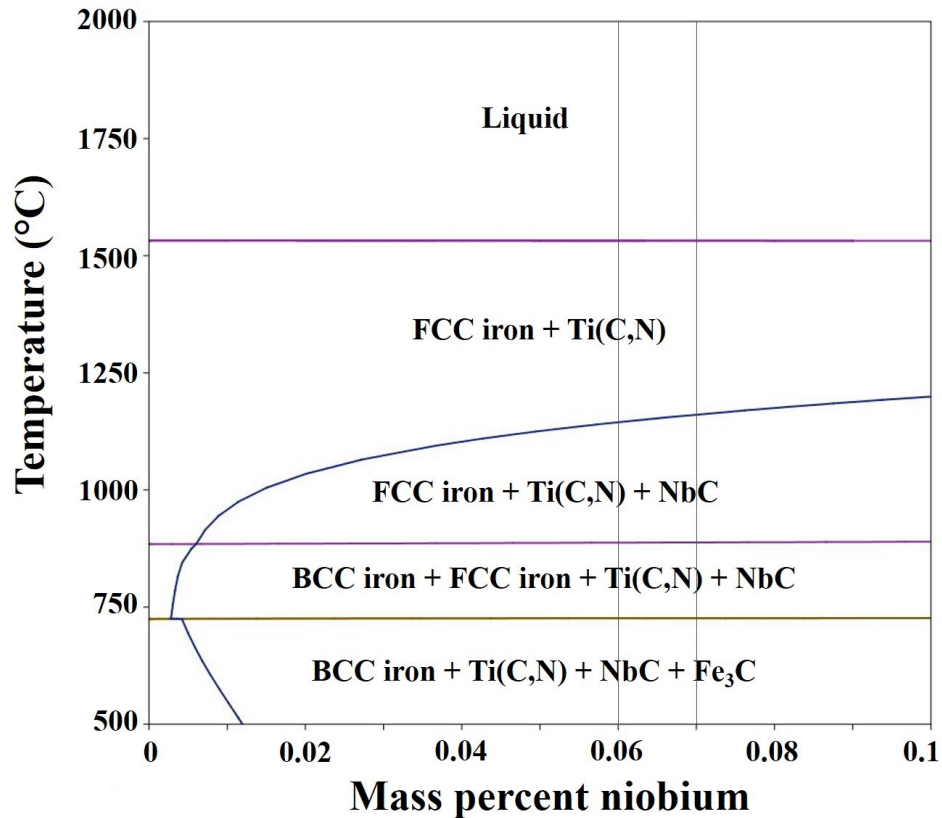


Figure 6.11: Iron-niobium phase diagram with a fixed amount of titanium, carbon and nitrogen (Steel B). The NbC formation curve, as a function of niobium content, is shown. The vertical lines represent the niobium composition range for Steel B.

The precipitation temperature for NbC is below 1473 K (1200°C) for the Steel B niobium composition. However, based on the morphology and size of Nb(C<sub>x</sub>N<sub>1-x</sub>), it is possible that the precipitation of Nb(C,N) occurred at higher temperatures. The size of particles precipitated at low temperatures is considerably small as compared to such coarse particles found in this study. According to Chen et al. (Che87) coarse NbC-rich (Ti,Nb)C,N particles (up to 10 μm) and of similar morphology precipitate in the interdendritic liquid. For the purpose of understanding possible precipitation at high temperature, and possible precipitation in the liquid steel (as a result

of segregation), a Scheil solidification model was considered. This model has already been discussed in Section 5.4 of the thesis. The model assumes no mixing in the solid state and complete mixing in the liquid state [Por92].

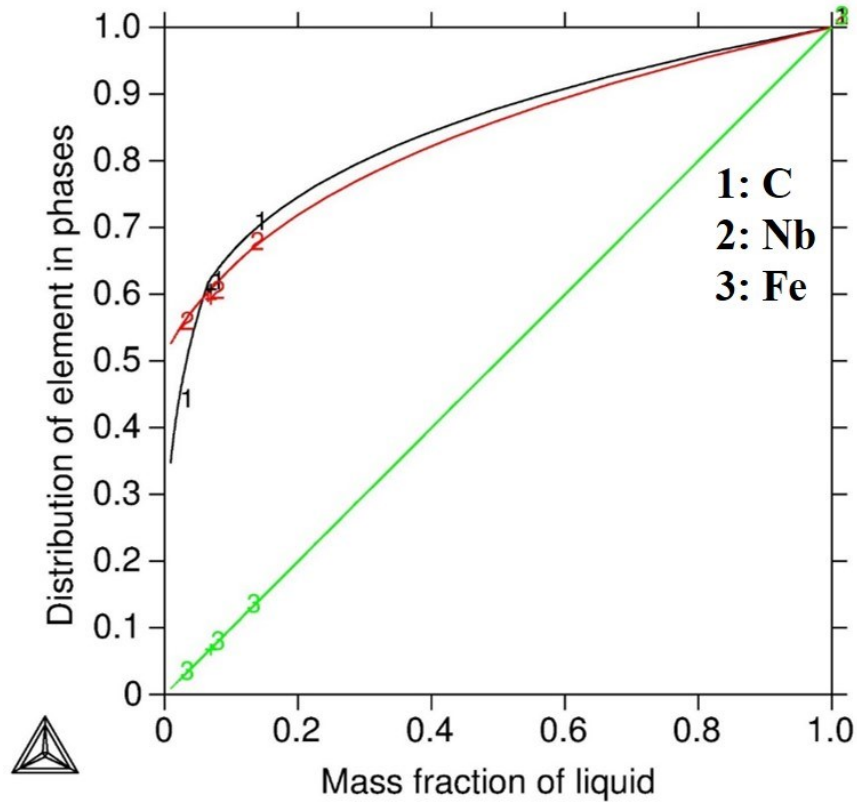


Figure 6.12: Distribution of carbon, niobium and iron in the liquid steel according to the Scheil solidification model.

Figure 6.12 shows the variation in the amounts of iron, niobium and carbon in the liquid during solidification, according to the Scheil solidification model. The x-axis shows the mass fraction of liquid remaining during solidification (*i.e.*, moving right to left depicts solidification with a decreasing amount of liquid and an increasing amount of solid). The y-axis shows the amount of element(s) (in the remaining fraction) in the liquid. There is segregation of niobium and carbon in

the liquid steel. For instance, when 50% liquid is left (mass fraction = 0.5), the fraction of niobium and carbon in that liquid is around 80% (fraction is 0.8). As a result of segregation, the liquid becomes enriched in carbon and niobium. The extent of niobium enrichment in the steel during solidification is shown with the help of Figure 6.13 and Table 6.2 (following the Scheil solidification model). Note that for simplicity only three elements are considered, *i.e.*, iron, niobium and carbon.

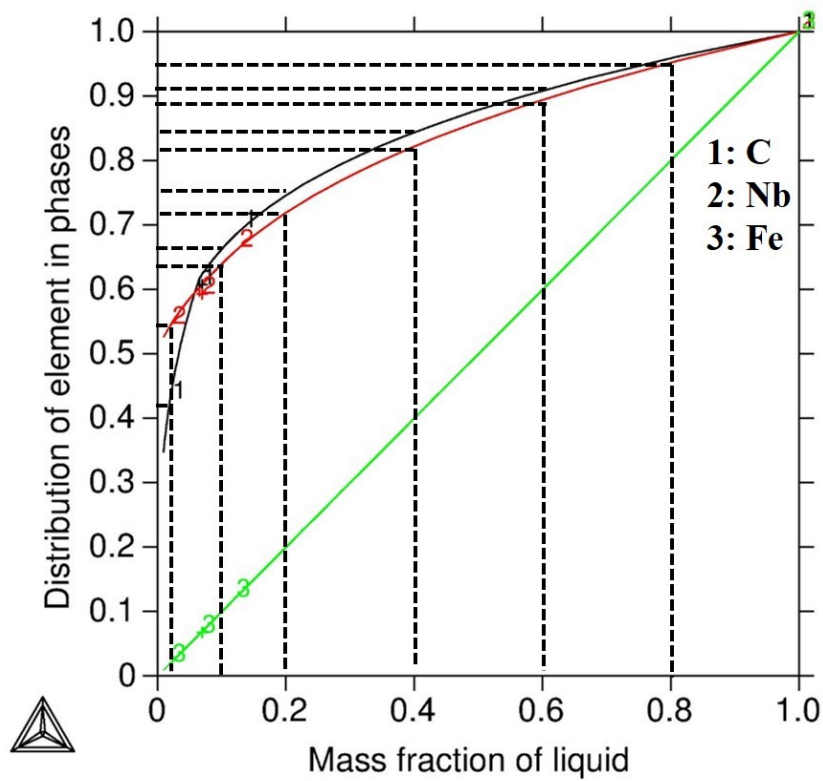


Figure 6.13: Dotted lines used for the calculation of carbon, niobium and iron contents in the liquid steel.

As an example, assume that the amount of carbon and niobium in the steel are 0.058 and 0.068 wt.%, respectively. When the mass fraction of the liquid is 0.8, *i.e.*, 20% of the liquid steel has solidified, the amount (in terms of mass fraction) of carbon left in that liquid is 0.96, which means

that 96% of the carbon present in the steel is in the liquid and the rest is in the solid. A mass fraction of 0.96 corresponds to 0.96 times 0.058 wt.% (nominal composition) or 0.0557 wt.% carbon. This amount is with reference to 100% liquid. The fraction of liquid is 0.8, so that the amount of carbon left in the liquid is  $0.0557/0.8 = 0.070$  wt.%. When 20% of the liquid steel has solidified, the remaining liquid has 0.070 wt.% carbon which is greater than the nominal carbon concentration of 0.058 wt.%. This is segregation of carbon. With 10% of the liquid remaining the amount of carbon increases to 0.39 wt.%. As solidification proceeds, the degree of segregation increases as shown in Table 6.2. Similar effects occur for niobium and these results are summarized in Table 6.2 as well.

Table 6.2: Calculation of amount of carbon and niobium in liquid determined from Figure 6.13.

	<b>Nominal Steel Composition (X) (wt.%)</b>	<b>Mass fraction of liquid (A)</b>	<b>Mass fraction of element in liquid (B)</b>	<b>Amount of element in liquid (X)(B) (wt.%)</b>	<b>Composition of Liquid ((X)(B)/(A)) (wt.%)</b>
Carbon	0.058	0.8	0.96	0.056	0.07
		0.6	0.91	0.053	0.088
		0.4	0.85	0.049	0.12
		0.2	0.76	0.044	0.22
		0.1	0.67	0.039	0.39
		0.01	0.42	0.024	2.4
Niobium	0.068	0.8	0.95	0.065	0.081
		0.6	0.89	0.061	0.1
		0.4	0.82	0.056	0.14
		0.2	0.72	0.049	0.25
		0.1	0.64	0.044	0.44
		0.01	0.55	0.037	3.7

By the time only 1% of the liquid (0.01 mass fraction) remains, the amount of carbon in the liquid has accumulated to nearly 2.4 wt.% (from an initial value of 0.058 wt.%). Similarly the amount of niobium, as a result of segregation, also increases in the liquid to the extent that the final 1% liquid (0.01 mass fraction) has nearly 3.7 wt.% niobium in it. These amounts of niobium and carbon may be enough to cause NbC precipitation in the liquid steel. Unfortunately, solubility data is not available for NbC in the liquid steel. All solubility data are either for precipitation of NbC in FCC iron or BCC iron.

## 6.4. Conclusions

Two set of experiments were conducted: 1) Niobium was added to steel samples (Steel A) and the samples were then checked for the presence of undissolved niobium-rich solid solution phase. 2) Steel samples with pre-existing coarse niobium-rich particles (Steel B) were characterised to identify the nature of the coarse particles, followed by thermodynamic evaluation of the system.

Steel A: Steel samples that were remelted and then had ferroniobium added (1 wt.% niobium) did not, after solidification, show any evidence of the niobium-rich solid solution phase that was present in the as-received ferroniobium alloy. Microstructural characterization of the solidified steel showed the presence of niobium-rich particles. They were identified as NbC with small amounts of titanium and iron.

Steel B: Steel samples with pre-existing coarse niobium-rich particles were provided by Evraz Inc. Characterization revealed that the coarse particles were niobium-titanium carbonitrides. The Scheil solidification model, based on the chemistry of Steel B, showed that segregation is possible for niobium and carbon during solidification of the steel. The segregation can result in a  $\sim 41$  times and  $\sim 54$  times increase in the amount of carbon and niobium, respectively, relative to the original steel composition in the final 1% of the liquid to solidify.

There is sufficient evidence to claim that the coarse niobium-rich particles in the steel are, in fact, NbC and/or Nb(C<sub>x</sub>N<sub>1-x</sub>) (with some titanium substituting for niobium) and not the niobium-rich, solid solution phase. This indicates that niobium-rich solid solution from ferroniobium is likely dissolving during steelmaking. Additional support is provided by the fact that the niobium-rich solid solution phase was not detected in steels with ferroniobium additions (1 wt.% niobium was added in the form of ferroniobium). However, as the size and weight fraction of niobium-rich solid

solution added to steel is very small, it is possible that some niobium-rich solid solution was not detected in the steel. It is, therefore, important to eliminate this possibility by designing a ferroalloy where the high melting temperature niobium-rich solid solution phase does not exist. This is the subject of the following chapter.

## 6.5. References

Abr06(1): S. Abraham, R. Klein, R. Bodnar and O. Dremailova. Formation of coarse particles in steel as related to ferroalloy dissolution thermodynamics. Part 1: ferroalloy melting, dissolution and microstructures. Material Science and Technology (MS & T), Cincinnati, Ohio, October 2006.

Abr06(2): S. Abraham, R. Klein, R. Bodnar and O. Dremailova. Formation of coarse particles in steel as related to ferroalloy dissolution thermodynamics. Part II: crystallographic study of ferroalloys and coarse particles. Material Science and Technology (MS & T), Cincinnati, Ohio, October 2006.

Che87: Z. Chen, M. H. Loretto and R. C. Cochrane. Nature of large precipitates in titanium containing HSLA Steels. Materials Science and Technology, 1987, 3, 836-844.

Cra00: A. J. Craven, K. He, L. A. J. Garvie and T. N. Baker. Complex heterogeneous precipitation in titanium-niobium microalloyed Al-killed HSLA steels-II. Non-Titanium based precipitates. Acta Materialia, 2000, 48, 3869-3878.

Gla97: T. Gladman. The Physical Metallurgy of Microalloyed Steels. The University Press Cambridge, UK, 1997.

Har71: E. M. Harold (ed.). The Making, Shaping and Treating of Steel. United States Steel, 1971.

Men99: R. Mendoza, J. Huante, M. Alanis, C. Gonzalez-Rivera and J. A. Juarez-Islas. Slab cracking after continuous casting of API 5L X-70 grade steel for pipeline sour gas application. Iron and Steelmaking, 1999, 26, 3, 205-209.

Por92: D. A. Porter and K. E. Easterling. Phase Transformation in Metals and Alloys. Chapman and Hall. London, 1992.

Pot01: R. M. Poths, R. L. Higginson and E. J. Palmiere. Complex precipitation behaviour in a microalloyed plate steel. *Scripta Materialia*, 2001, 44, 147-151.

Tia07: Q. Tian, Y. Chen, J. Chen, G. Xu and Y. Zheng. Characterization of Nb-rich phase precipitation near internal cracks in continuously cast slabs. Minerals, Metals and Materials Society (TMS), Warrendale, PA, 15086-7528, USA: 2007.

Yua09: S. Q. Yuan and G. L. Liang. Dissolving behaviour of second phase particles in Nb-Ti microalloyed steel. *Materials Letters*, 2009, 63, 2324-2326.

Zho96: C. Zhou and R. Priestner. The evolution of precipitates in Nb-Ti microalloyed steels during solidification and post-solidification cooling. *ISIJ International*, 1996, 36, 11, 1397-1405.

Zhu07: X. Zhuo, X. Wang, W. Wang and H. G. Lee. Nature of large (Ti, Nb)(C, N) particles precipitated during the solidification of Ti, Nb HSLA steel. *Journal of University of Science and Technology Beijing: Mineral Metallurgy Materials (Eng Ed)*, 2007, 14, 2, 112-117.

Zhu08: X. Zhuo, D. Woo, X. Wang and H. Lee. Formation and thermal stability of large precipitates and oxides in titanium and niobium microalloyed steel. *Journal of Iron and Steel Research International*, 2008, 15, 3, 70-77.

## Chapter 7: Ternary Alloys (Niobium-Aluminum-Iron)

### 7.1. Introduction

Microalloyed steels exhibit high yield strengths and toughness due to the addition of small amounts of alloying elements [Gla97]. These alloying elements are added in form of their respective ferroalloys during the steelmaking process; e.g., ferroniobium, ferrotitanium and ferrovandium [Har71]. Ferroniobium consists of two phases: a niobium-rich solid solution (with a melting temperature of  $\sim 2673$  K ( $\sim 2400^\circ\text{C}$ ) and an intermetallic,  $\text{Fe}_7\text{Nb}_6$  (with a melting temperature  $< 1873$  K ( $< 1600^\circ\text{C}$ )) [Sha13(1), Sha13(2)]. Due to its high melting temperature, the niobium-rich solid solution phase can remain undissolved or may require prolonged times for dissolution [Eng92]. It has been reported that undissolved phases in ferroniobium leads to the formation of coarse niobium-rich particles in the steel that have a deleterious effect on its mechanical properties [Abr06(1), Abr06(2)]. However, the work presented in Chapter 6 shows that might not be the case. There is a strong possibility that niobium-rich solid solution phase dissolves and coarse niobium-rich particles are carbide and/or carbonitrides formed as a result of precipitation. Still, the elimination of the niobium-rich solid solution phase from the as-received ferroniobium alloy will be helpful in minimizing the dissolution time of ferroniobium alloys in steel. One way to eliminate the niobium-rich solid solution phase from ferroniobium is by chemically modifying the as-received ferroniobium alloy. In the current chapter, the effects of adding pure aluminum to the as-received ferroniobium alloy are investigated. Aluminum is a low melting temperature metal and is usually used in steel for killing purposes. The new alloys formed (by aluminum addition) are

investigated using SEM, TEM and DSC techniques. At a certain threshold composition of aluminum, the high melting temperature niobium-rich solid solution phase is eliminated.

## 7.2. Experimental Methods

Commercial grade ferroniobium alloy was provided by Evraz Inc. NA along with its chemical composition. The composition was verified by Cambridge Scientific and both results have already been compared and discussed in Chapters 4 and 5. In this part of the study, the composition reported by Cambridge Scientific has been taken into consideration, *i.e.*, 64.1 wt.% niobium, 32.8 wt.% iron and 3.1 wt.% impurities.

New ferroniobium alloys were made both by induction melting and by arc melting. For induction melting, the as-received ferroniobium was melted with different amounts of aluminum (purity = 99.9 wt.%) under positive argon pressure. The amount of aluminum added varied from 5 to 20 wt.% (with an interval of 5 wt.%). The samples were heated from 2023 K to 2123 K (1750°C to 1850°C) for different times (40 to 75 minutes) and were then cooled at a cooling rate of approximately 15 to 20 K/min. The arc melted samples were prepared using pure iron (purity = 99.95 wt.%), niobium (purity = 99.95 wt.%) and aluminum (purity = 99.999 wt.%). For homogeneity purposes, each sample was melted three times under positive argon gas pressure. The compositions of the arc and induction melted samples were nearly the same. The detail experimental procedure for fabrication of induction melted and arc melted alloys are discussed in Chapter 3, *i.e.*, Sections 3.7 and 3.8.

SEM samples were prepared by using conventional metallographic techniques. A VEGA-3 (Tescan) SEM with a scintillation type BSE detector, operated at 20 kV, was used for imaging

purposes. For compositional analysis through EDX analysis, a Hitachi S-2700 SEM equipped with a GW electronics system solid state BSE detector and a PGT PRISM intrinsic germanium (IG) EDX detector was used. SEM sample preparation and operating conditions are described in Section 3.3 of the thesis.

TEM samples were prepared using a Hitachi NB5000 dual beam FIB-SEM. A JEOL JEM-2010 TEM was used for both DF and BF imaging along with SAD. The TEM was operated at 200 kV. EDX spectra were also obtained via a Noran ZMAX30 silicon-lithium EDX detector. The details are discussed in Section 3.4.

Melting/solidification and phase transformation temperatures were studied using a Setaram Labsys Evo 1600 DSC; details are provided in Section 3.6.

### **7.3. Results and Discussion**

Detailed characterization of the as-received ferroniobium alloy has been done and has been reported in Chapters 4 and 5. XRD, SEM, DSC and TEM were used to identify the phases present and to establish the microstructural evolution of the as-received ferroniobium alloy [Sha13(1), Sha13(2)]. The as-received ferroniobium alloy is composed of two phases, a niobium-rich solid solution and an intermetallic  $\text{Fe}_7\text{Nb}_6$ . The primary phase is the  $\text{Fe}_7\text{Nb}_6$  intermetallic, formed from the liquid phase as a result of a proeutectic reaction. The eutectic reaction results in formation of a eutectic mixture of the niobium-rich solid solution phase and  $\text{Fe}_7\text{Nb}_6$ . A slight variation in the composition exists between the proeutectic intermetallic and the intermetallic formed during the eutectic reaction. The eutectic intermetallic is more niobium-rich as compared with the pro-

eutectic intermetallic. A BSE image of the representative microstructure of the as-received ferroniobium alloy is shown in Figure 7.1.

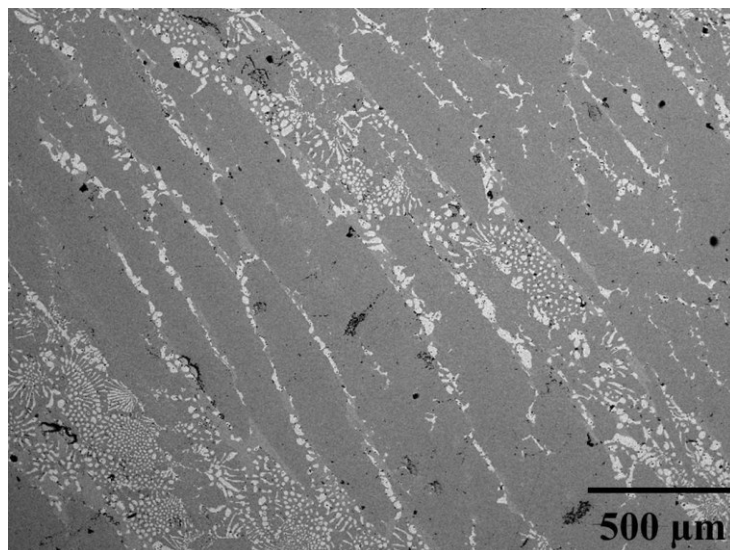


Figure 7.1: Representative microstructure of as-received ferroniobium alloy. The white regions are the niobium-rich solid solution phase and the darker regions are Fe<sub>7</sub>Nb<sub>6</sub> intermetallic.

### 7.3.1. Ternary Alloys (Induction Melting)

Preliminary microstructural characterization of induction melted ternary ferroalloys (5 to 20 wt.% aluminum) was done using SEM. These alloys were prepared using the induction melting furnace by adding different amounts of aluminum to the as-received ferroniobium alloy. The compositions of the aluminum added ferroalloys are shown in Table 7.1. Low and high magnification BSE images for ferroniobium alloys with 5 and 10 wt.% aluminum added are shown in Figure 7.2.

Table 7.1: Target composition of various aluminum added ferroniobium samples prepared by induction melting

<b>Alloys</b>	<b>Elements</b>	<b>Wt.%</b>
5 wt.% Al added ferroniobium	Nb	60.9
	Fe	31.2
	Al	5.0
	Impurities	2.9
10 wt.% Al added ferroniobium	Nb	57.7
	Fe	29.5
	Al	10.0
	Impurities	2.8
15 wt.% Al added ferroniobium	Nb	54.5
	Fe	27.9
	Al	15.0
	Impurities	2.6
20 wt.% Al added ferroniobium	Nb	51.3
	Fe	26.2
	Al	20.0
	Impurities	2.5

The ferroniobium alloy with 5 wt.% aluminum is shown in Figures 7.2a and 7.2c. Four different contrast regions are labeled as 1-4 in Figure 7.2c. According to EDX analysis, region 1 appears to be a niobium-rich solid solution with 98-99 wt.% niobium and the balance is iron (~ 97.5 at.% niobium and 2.5 at.% iron)). Region 2 has 73-74 wt.% niobium, 22-23 wt.% iron and 3-4 wt.%

aluminum (~ 59.7 at.% niobium, 30.5 at.% iron and 9.8 at.% aluminum). Region 2 appears to be a ternary intermetallic alloy, since niobium cannot dissolve as much iron as the solid solution [Bej 93(1), Vob11]. Region 3 has 65-67 wt.% niobium, 27-30 wt.% iron and 4-6 wt.% aluminum (~ 49.9 at.% niobium, 35.8 at.% iron and 14.3 at.% aluminum). Region 3 makes up most of the microstructure and is hereafter referred to as the matrix. According to binary phase diagrams of iron-niobium shown in figure 5.5 and 5.6: the range of niobium content in  $\text{Fe}_7\text{Nb}_6$  phase varies from 46 to 51 at.% and 48 to 54 at.% respectively. The niobium content of region 3 lies exactly in this composition range. Based on composition information only, region 3 appears to be  $\text{Fe}_7\text{Nb}_6$  with aluminum atoms partially substituting for iron atoms. Region 4 has 54-56 wt.% niobium, 38-39 wt.% iron and 6-7 wt.% aluminum (~ 38.9 at.% niobium, 45.3 at.% iron and 15.8 at.% aluminum). According to the iron-niobium binary phase diagrams shown in Figures 5.5 and 5.6, the amount of niobium in  $\text{Fe}_2\text{Nb}$  phase varies from 25 to 38 at.% and 32 to 39 at.%, respectively. On this basis, it can be estimated that region 4 is potentially  $\text{Fe}_2\text{Nb}$  with iron partially replaced by aluminum atoms. For future reference moving forward, region 3 will be regarded as the  $\text{Fe}_7\text{Nb}_6$  intermetallic phase (with aluminum atoms partially substituting for iron atoms) and region 4 will be regarded as the  $\text{Fe}_2\text{Nb}$  intermetallic phase (with aluminum atoms partially substituting for iron atoms).

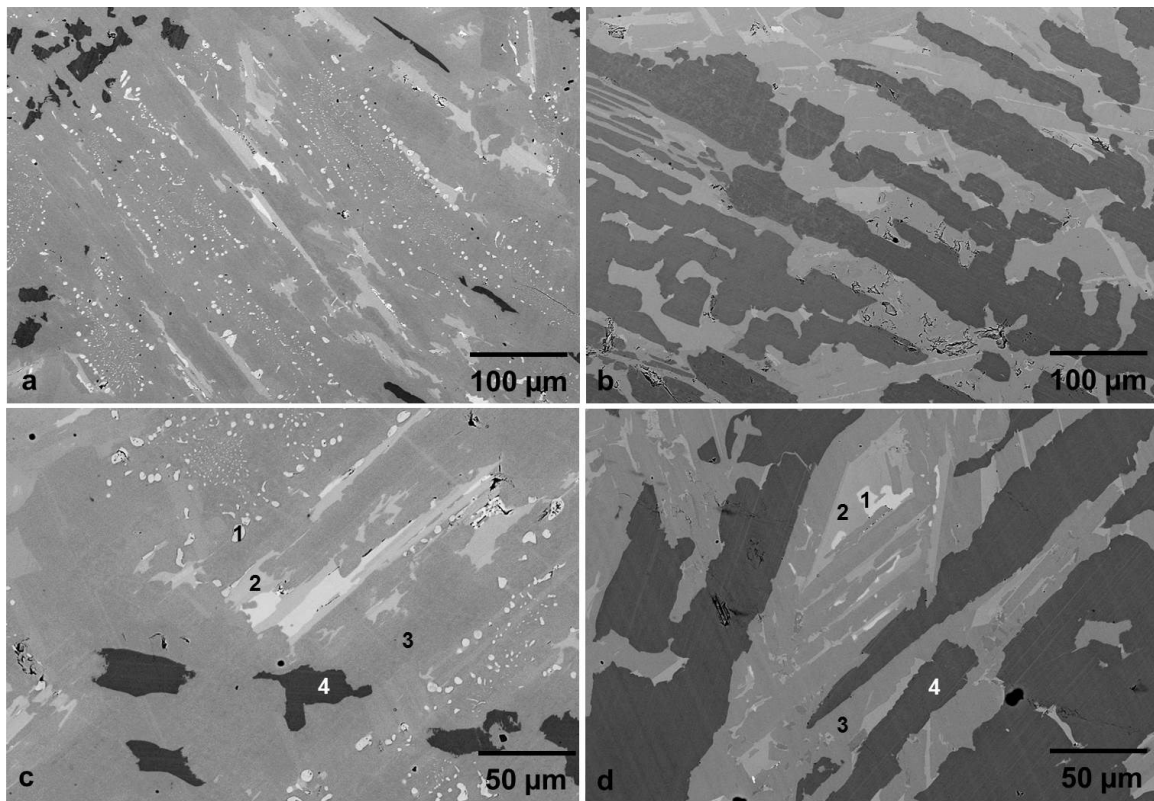


Figure 7.2: a) and b) Low magnification BSE images of ferroniobium ternary alloys with 5 wt.% and 10 wt.% aluminum additions, respectively, fabricated by induction melting. c) and d) Higher magnification BSE images of a) and b), respectively, showing regions labeled 1-4.

The ferroniobium sample with 10 wt.% aluminum added also has four different contrast regions as shown in Figure 7.2b and 7.2d. The highest niobium content is in region 1, which has 83-86 wt.% niobium, 7-10 wt.% iron and 6-7 wt.% aluminum. A region with this composition was absent in the 5 wt.% aluminum added ternary sample. The amount of iron exceeds the solubility limit for iron in niobium, which is less than 5 wt.% [Vob11]. Still, the possibility of region 1 being a niobium-rich solid solution phase cannot be ruled out. The system could be metastable and may contain impurities. In addition, there are errors associated with composition analysis through EDX

spectroscopy. To identify the phase, a TEM FIB sample was prepared of region 1 and electron diffraction analysis was done.

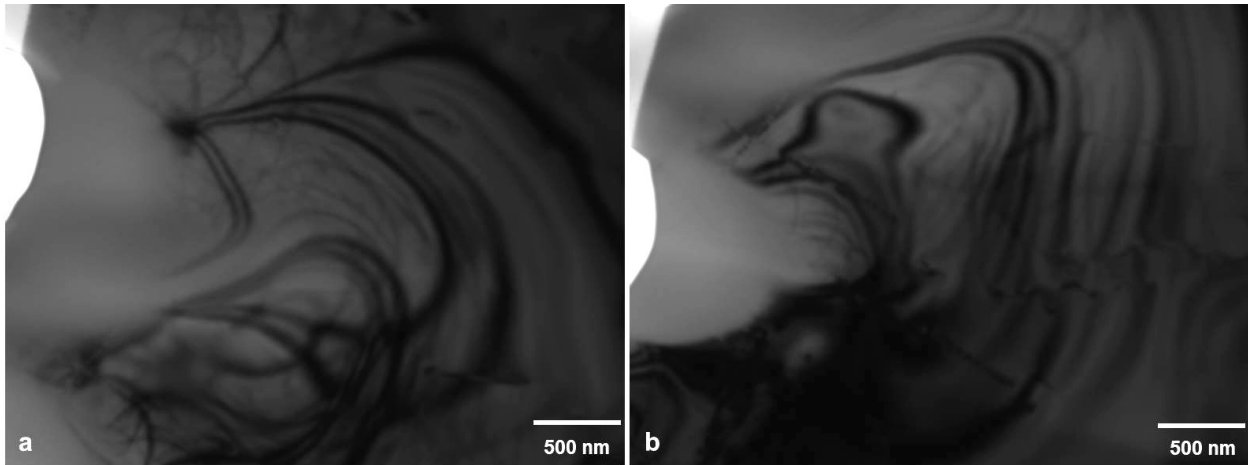


Figure 7.3: a) and b) TEM bright field (BF) images of region 1 from Figure 6.2d (83-86 wt.% niobium).

TEM bright field (BF) images of region 1, for the 10 wt.% aluminum added sample, are shown in Figure 7.3. EDX analysis was done to verify the composition of the phase/region. Composition analysis of the phase done through TEM EDX analysis is in good agreement with the composition analysis done by SEM EDX analysis. Several SAD patterns were obtained from the TEM sample. Three representative SAD patterns are shown in Figure 7.4. The SAD pattern in Figure 7.4c could be indexed to  $Nb_3Al$ , assuming that iron atoms replace some of the aluminum atoms. The calculated d-spacings for (110), (111) and (001) are 0.708nm, 0.411 nm and 0.508 nm respectively (Figure 7.4c). However, the other two patterns (Figure 7.4a and 7.4b) could not be indexed to  $Nb_3Al$  or any other niobium-iron intermetallics, niobium-aluminum intermetallics or niobium-iron-aluminum intermetallics; they could not be indexed to the niobium-rich solid solution phase either. Based on the composition analysis (both SEM EDX and TEM EDX analysis), region 1

appears to be a niobium-rich ternary intermetallic. It may be metastable and, such, is not available in the database.

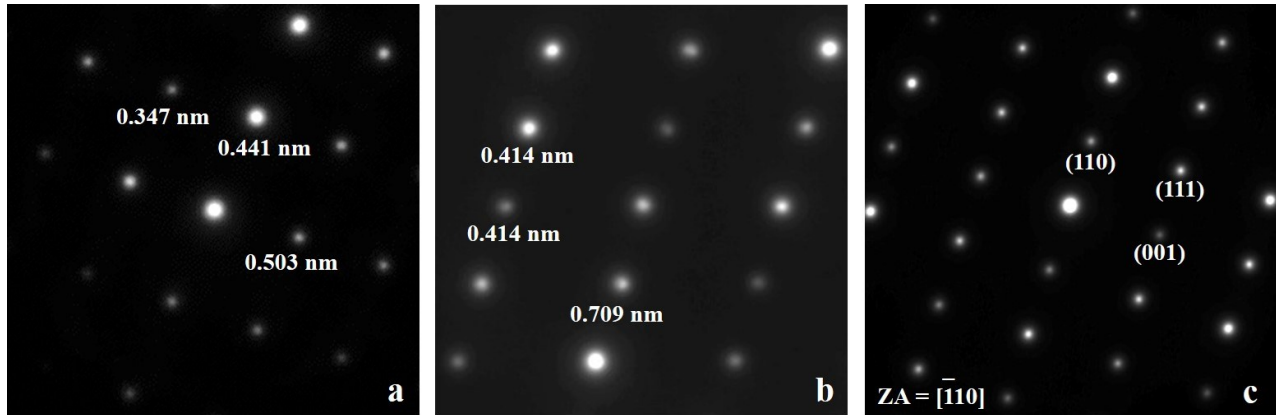


Figure 7.4: a), b) and c) SAD patterns taken from the region shown in Figure 6.3. The pattern in (c) can be indexed to  $\text{Nb}_3\text{Al}$ ; the zone axis is shown.

Regions 2-4 of ferroniobium with 10 wt.% aluminum added are comparable to regions 2-4 of ferroniobium with 5 wt.% aluminum added. The main difference is the higher amount of aluminum in regions 2-4 (in the 10 wt.% aluminum sample) due to the higher overall aluminum content. The other significant difference is the volume fraction of region 3 ( $(\text{Fe,Al})_7\text{Nb}_6$ ) and region 4 ( $(\text{Fe,Al})_2\text{Nb}$ ). In the 5 wt.% aluminum ternary alloy,  $(\text{Fe,Al})_7\text{Nb}_6$  is more abundant (volume fraction of 0.848 with a standard deviation of 0.04) than  $(\text{Fe,Al})_2\text{Nb}$  (volume fraction of 0.035 with a standard deviation of 0.014). However, in the 10 wt.% aluminum ternary alloy a substantial decrease in the volume fraction of  $(\text{Fe,Al})_7\text{Nb}_6$  (volume fraction of 0.54 with a standard deviation of 0.074) is seen with a corresponding increased volume fraction for  $(\text{Fe,Al})_2\text{Nb}$  (volume fraction of 0.42 with a standard deviation of 0.074).

Figures 7.5a and 7.5c show SEM BSE images (high and low magnification) of the 15 wt.% aluminum added ferroniobium alloy. This microstructure has three different contrast regions. On the basis of composition and for comparison with the 5 and 10 wt.% aluminum added ferroniobium samples, these regions are labeled region 1, region 3 and region 4. There is no region 2. Region 1 is similar to region 1 in the 10 wt.% aluminum added sample. The difference is the higher amount of aluminum in region 1 of the 15 wt.% aluminum added ternary alloy compared with the 10 wt.% aluminum added sample. There is no comparable region to region 2 in the 10 wt.% aluminum ternary sample. Regions 3 and 4 ((Fe,Al)<sub>7</sub>Nb<sub>6</sub> and (Fe,Al)<sub>2</sub>Nb respectively) of the 10 wt.% aluminum added ternary sample correlate with regions 3 and 4 ((Fe,Al)<sub>7</sub>Nb<sub>6</sub> and (Fe,Al)<sub>2</sub>Nb respectively) of the 15 wt.% aluminum added ternary alloy.

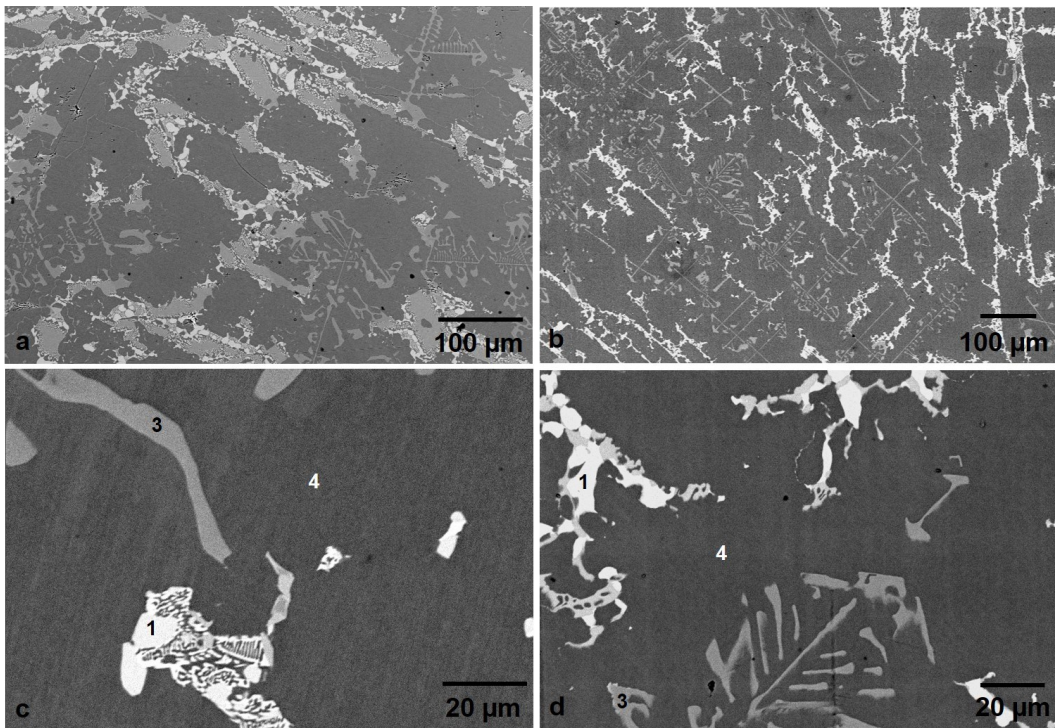


Figure 7.5: a) and b) Low magnification BSE images of ferroniobium ternary alloys with 15 wt.% and 20 wt.% aluminum, respectively, made by induction melting. c) and d) Higher magnification BSE images of a) and b), respectively, showing three regions labeled 1, 3 and 4.

SEM BSE images at low and high magnification for the 20 wt.% aluminum added ferroniobium alloy are shown in Figures 7.5b and 7.5d, respectively. The 20 wt.% aluminum added ferroniobium alloy has a similar microstructure and morphology as the 15 wt.% aluminum added ferroniobium alloy. The difference once again is the higher amount of aluminum in all three regions due to the overall higher aluminum content.

Table 7.2 shows the chemistry of all regions identified in ferroniobium alloys with different aluminum additions. Regions 3 and 4 ( $(\text{Fe,Al})_7\text{Nb}_6$  and  $(\text{Fe,Al})_2\text{Nb}$  respectively) are consistently present in all compositions with slight chemistry variations due to the different aluminum contents. In Table 7.2 there are two columns for region 1. The reason is that region 1 is designated as the region (or phase) with the maximum niobium content. In the sample with 5 wt.% aluminum the niobium-rich solid solution phase (with niobium content of 98-99 wt.%) is present, while for the other chemistries the solid solution phase is missing; instead it is replaced by a phase containing 83-86 wt.% niobium.

Table 7.2: Chemistry (wt.%) of various regions of ferroniobium samples with different amounts of aluminum (compositions determined through SEM-EDX analysis)

<b>Aluminum Content</b>	<b>Elements</b>	<b>Region 1</b>	<b>Region 1</b>	<b>Region 2</b>	<b>Region 3</b>	<b>Region 4</b>
5 wt.%	Nb	98-99		73-74	65-67	54-56
	Fe	1-2		22-23	27-30	38-39
	Al			3-4	4-6	6-7
10 wt.%	Nb		83-86	72-75	68-69	56-58
	Fe		7-10	18-20	22-24	30-35
	Al		6-7	6-8	8-9	10-12
15 wt.%	Nb		85-86		68-69	56-57
	Fe		5-6		20-21	29-31
	Al		8-9		10-11	13-14
20 wt.%	Nb		83-84		69-71	51-55
	Fe		4-6		16-18	26-29
	Al		11-12		13-14	18-20

To summarize, as the amount of aluminum in the as-received ferroniobium alloy is increased (from 5 to 20 wt.%), the volume fraction of the (Fe,Al)<sub>2</sub>Nb phase increases (region 4) and replaces the

(Fe,Al)<sub>7</sub>Nb<sub>6</sub> phase (region 3). The target of eliminating the niobium-rich solid solution phase is achieved as the amount of aluminum is increased from 5 wt.% to 10 wt.%. The region with the maximum amount of niobium (region 1) contains 83-86 wt.% niobium (10 wt.% aluminum sample). The nature of this region is not yet known. However, TEM analysis ruled out the niobium-rich solid solution. The nature and volume fraction of the different phases presented in Table 7.2 are shown in Table 7.3.

Table 7.3: Nature and volume fraction of different phases identified in Table 7.2

Aluminum Content	Volume Fraction (Standard Deviation)				
	Region 1	Region 1	Region 2	Region 3	Region 4
5 wt.%	0.036 (0.02)		0.089 (0.041)	0.840 (0.041)	0.035 (0.014)
10 wt.%		0.008 (0.01)	0.031 (0.0097)	0.540 (0.087)	0.42 (0.085)
15 wt.%		0.091 (0.021)		0.230 (0.032)	0.676 (0.026)
20 wt.%		0.081 (0.012)		0.109 (0.024)	0.807 (0.024)
Phases Identified	Niobium-rich solid solution	Unknown	unknown	(Fe,Al) <sub>7</sub> Nb <sub>6</sub>	(Fe,Al) <sub>2</sub> Nb

### 7.3.2. Ternary Alloys (Arc Melting)

The ferroniobium alloy with 10 wt.% aluminum, prepared by induction melting, did not contain any of the niobium-rich solid solution phase. In order to study the effect of aluminum additions on the liquidus temperature of the ferroniobium alloys, ternary alloys composed of pure niobium, aluminum and iron were prepared. The alloys were made with nearly the same composition as the induction melted ternary alloys. The composition of as-received ferroniobium alloy was 64.1 wt.% niobium and 32.8 wt.% iron with the remaining amount impurities. The adjusted composition, considering the ferroniobium alloy to be a binary alloy and neglecting impurities, was 66.15 wt.% niobium and 33.85 wt.% iron (54 at.% niobium and 46 at.% iron). An arc melted sample of the same composition was made, *i.e.*, without any aluminum addition. This fabricated binary alloy had a similar microstructure to the as-received ferroniobium alloy. The difference, however, is a finer microstructure for the arc melted sample due to its faster cooling rate. The same ratio of niobium and iron was maintained in all the alloys prepared through arc melting. The composition of fabricated 5 wt.% aluminum ternary alloys was 5 wt.% aluminum, 62.8 wt.% niobium and 32.2 wt.% iron (47 at.% niobium, 40 at.% iron and 13 at.% aluminum). The composition of 10 wt.% aluminum ternary alloy was 10 wt.% aluminum, 59.5 wt.% niobium and 30.5 wt.% iron (41.2 at.% niobium, 35 at.% iron and 23.8 at.% aluminum). Similarly the composition of 15 wt.% aluminum ternary alloy was 15 wt.% aluminum, 56.2 wt.% niobium and 28.8 wt.% iron (36.1 at.% niobium, 30.7 at.% iron and 33.2 at.% aluminum).

Figure 7.6a and 7.6b show the microstructure of 5 wt.% aluminum added arc melted sample at lower and higher magnifications, respectively. The higher magnification image shows two different contrast regions. EDX analysis shows that the bright contrast regions are niobium-rich relative to the matrix. Because of the small particle size, there is overlap with the surrounding

matrix. Based on comparison with the 5 wt.% induction melted samples, the particles are likely the niobium-rich solid solution phase. The darker contrast region has a composition of 67-69 wt.% niobium (51-54 at.%), 26-28 wt.% iron (33-36 at.%) and 4-5 wt.% aluminum (11-14 at.%). Based on the chemistry, this phase appears to be the  $(\text{Fe,Al})_7\text{Nb}_6$  intermetallic.

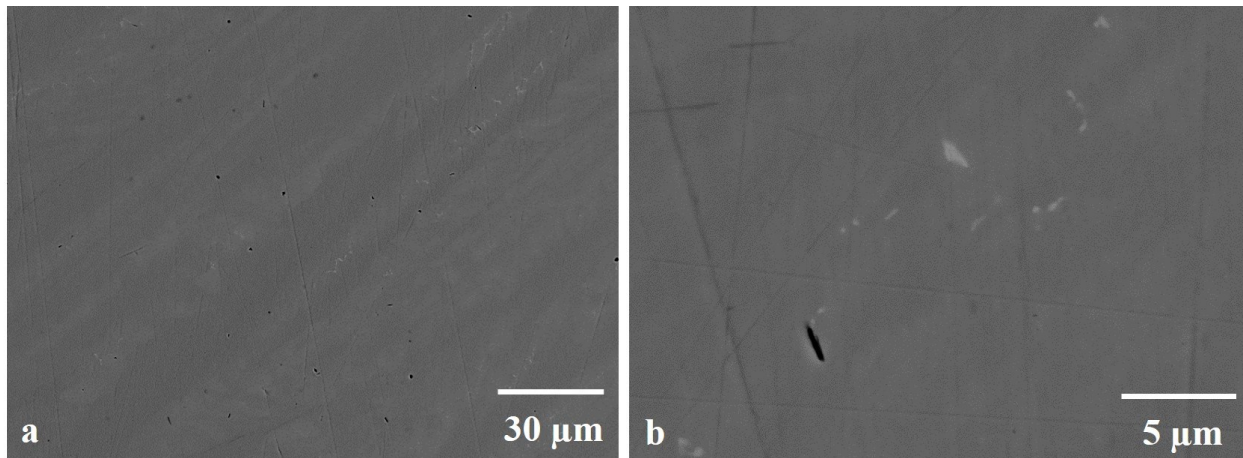


Figure 7.6: a) and b) Low and high magnification BSE images of iron-niobium-aluminum ternary alloys (5wt.% aluminum) prepared by arc melting.

Figures 7.7a and 7.7c show the microstructure (lower and higher magnifications, respectively) of a 10 wt.% aluminum ternary alloy. Figure 7.7c shows three different contrast regions. For consistency and to compare the results with the induction melted samples, the regions are labeled as region 1, region 3 and region 4. The compositions of these three regions are as follows: Region 1 contains 79-82 wt.% niobium, 12-15 wt.% iron and 6-7 wt.% aluminum; region 3 contains 66-67 wt.% niobium, 25-27 wt.% iron and 7-8 wt.% aluminum; region 4 contains 54-55 wt.% niobium, 33-35 wt.% iron and 10-11 wt.% aluminum. These regions have nearly the same composition as the three regions (region 1, 3 and 4) in the 10 wt.% aluminum added ferroniobium alloy prepared by induction melting. Some disparity exists due to the presence of impurities in the

induction melted samples. On the basis of composition, region 3 and region 4 are the  $\text{Fe}_7\text{Nb}_6$  intermetallic phase (with aluminum atoms partially substituting for iron atoms) and the  $\text{Fe}_2\text{Nb}$  intermetallic phase (with aluminum atoms partially substituting for iron atoms), respectively.

Figures 7.7b and 7.7d show the microstructure (lower and higher magnifications, respectively) of the 15 wt.% aluminum ternary alloy. Figure 7.7d shows three different contrast regions as well; again for consistency and comparison the regions are labeled as region 1, 3 and 4. Region 3 contains 65-67 wt.% niobium, 20-22 wt.% iron and 12-13 wt.% aluminum ( $(\text{Fe},\text{Al})_7\text{Nb}_6$  intermetallic). Region 4 contains 53-56 wt.% niobium, 28-31 wt.% iron and 15-17 wt.% aluminum ( $(\text{Fe},\text{Al})_2\text{Nb}$  intermetallic). Region 1 was too fine for EDX analysis, *i.e.*, the interaction volume was larger than the region. Therefore, its composition was not determined. However, based on the contrast and comparison with the induction melted ternary alloy, region 1 of the arc melted ternary alloy most likely has a similar composition as the region 1 of induction melted alloy. There are some slight differences between the compositions of  $(\text{Fe},\text{Al})_7\text{Nb}_6$  and  $(\text{Fe},\text{Al})_2\text{Nb}$  intermetallics (region 3 and region 4) formed by induction and arc melting. The reason being the impure nature of the induction melted samples.

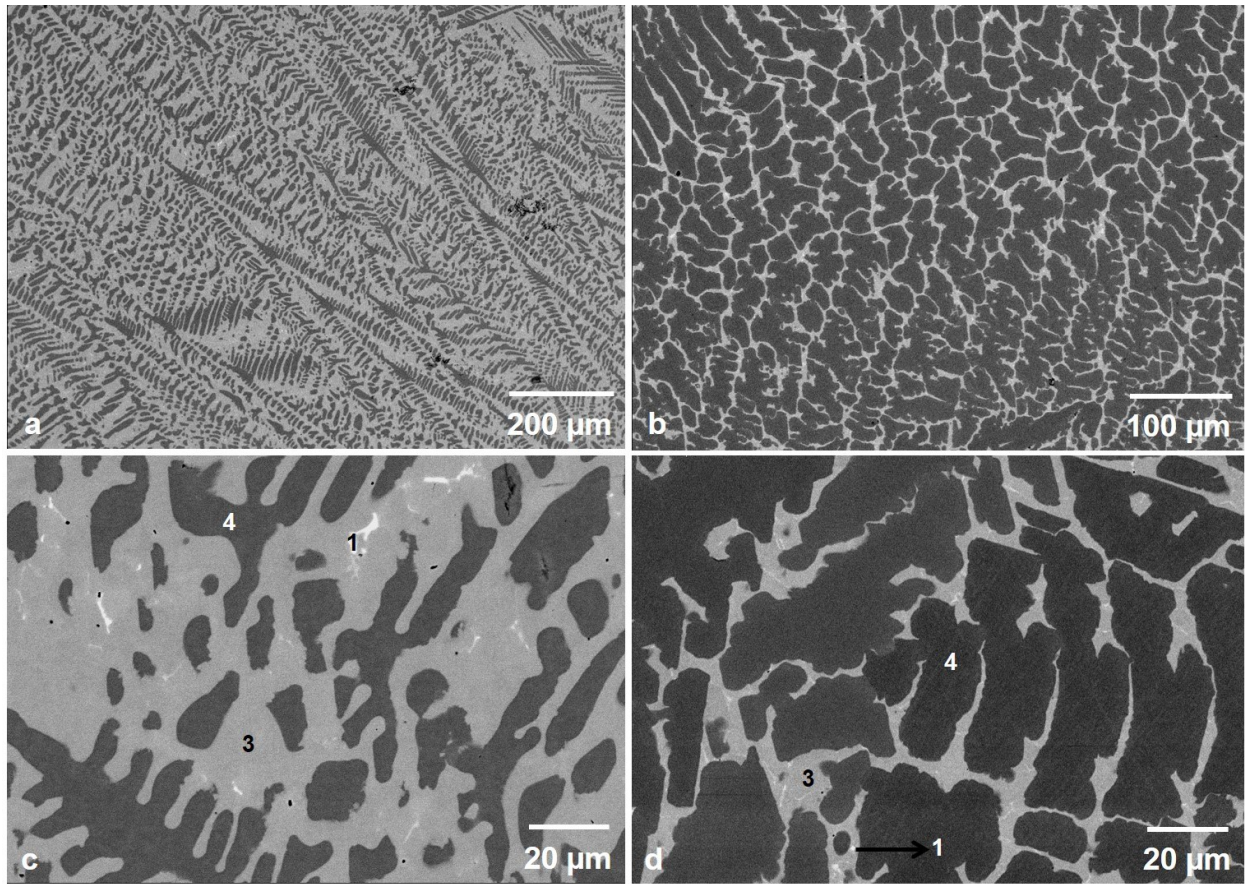


Figure 7.7: a) and b) Low magnification BSE images of iron-niobium-aluminum ternary alloys (10 wt.% and 15 wt.% aluminum, respectively) made by arc melting. c) and d) Higher magnification BSE images of a) and b), respectively, showing three regions labeled 1, 3 and 4.

Comparison of the two arc melted samples, *i.e.*, with 10 and 15 wt.% aluminum, shows that regions 3 and 4 are comparable for both alloys. By increasing the amount of aluminum from 10 to 15 wt.%, the amount of aluminum in these regions also correspondingly increases. The increase in aluminum in  $(\text{Fe,Al})_7\text{Nb}_6$  intermetallic is mainly at the expense of iron. Also, in moving from 10 to 15 wt.% aluminum, the majority phase/region (matrix) changes from  $(\text{Fe,Al})_7\text{Nb}_6$  (region 3) to  $(\text{Fe,Al})_2\text{Nb}$  (region 4).

### 7.3.3. Effect of Aluminum Additions on the Liquidus Temperature

DSC studies were done on the different ternary niobium-iron-aluminum alloys, prepared by arc melting, to study the effect of aluminum additions to ferroniobium. The arc melted samples were used in order to establish a melting/solidification temperature for the new alloys. The samples were heated in the DSC to a temperature of 1873 K (1600°C) in the presence of an inert argon atmosphere. For homogenization purposes, the samples were kept at 1873 K for a period of 15 minutes. Three different cooling rates (5, 10 and 20 K/min) were used to cool the samples to room temperature. The solidification start temperatures (onset) for all the compositions studied (0 to 10 wt.% Al), with the three different cooling rates, are shown in Table 7.4 and Figure 7.8. The data is extrapolated linearly to 0 K/min in order to establish the solidification temperature at equilibrium. The liquidus temperature, *i.e.*, 1813 K (1540°C) for the 0 wt.% aluminum alloy (binary niobium-iron alloy), achieved by DSC is in accordance with the liquidus temperature of the same alloy by Bejarano et al, *i.e.*, ~ 1811 K (~ 1538°C) [Bej93(1)].

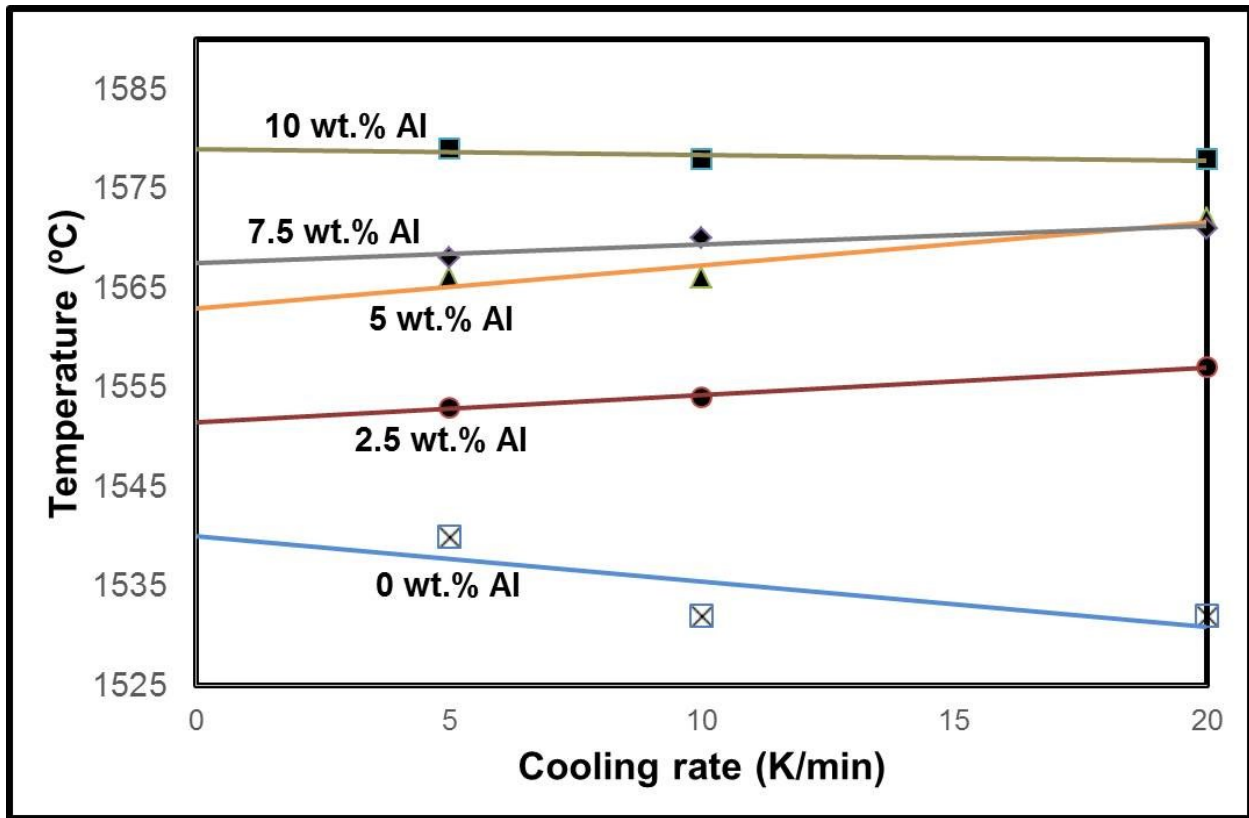


Figure 7.8: Solidification start temperature for different cooling rates for niobium-iron-aluminum ternary alloys, with 0 to 10 wt.% aluminum. The data is extrapolated to 0 K/min.

Table 7.4: Solidification start temperature for niobium-iron-aluminum alloys with different aluminum compositions and different cooling rates

<b>Composition (wt.% Al)</b>	<b>Cooling Rate (K/min)</b>	<b>Solidification Temperature (start) (K (°C))</b>	<b>Solidification Temperature at 0 K/min (K (°C))</b>
0	5	1813 (1540)	1813 (1540)
	10	1805 (1532)	
	20	1805 (1532)	
2.5	5	1826 (1553)	1824.5 (1551.5)
	10	1827 (1554)	
	20	1830 (1557)	
5	5	1839 (1566)	1836 (1563)
	10	1839 (1566)	
	20	1845 (1572)	
7.5	5	1841 (1568)	1840.5 (1567.5)
	10	1843 (1570)	
	20	1844 (1571)	
10	5	1852 (1579)	1852 (1579)
	10	1851 (1578)	
	20	1851 (1578)	

The equilibrium solidification temperature increases as the amount of aluminum in the alloy increases (Figure 7.9). As shown earlier, the niobium-rich solid solution phase was eliminated in the 10 wt.% aluminum alloy. However, the overall liquidus temperature of the alloy is increased by 39 K, when compared with the alloy containing 0 wt.% aluminum. The steelmaking temperature during ferroniobium addition is around 1873 K (1600°C). Therefore, at this temperature melting of the ternary alloy, with 10 wt.% aluminum, would be expected.

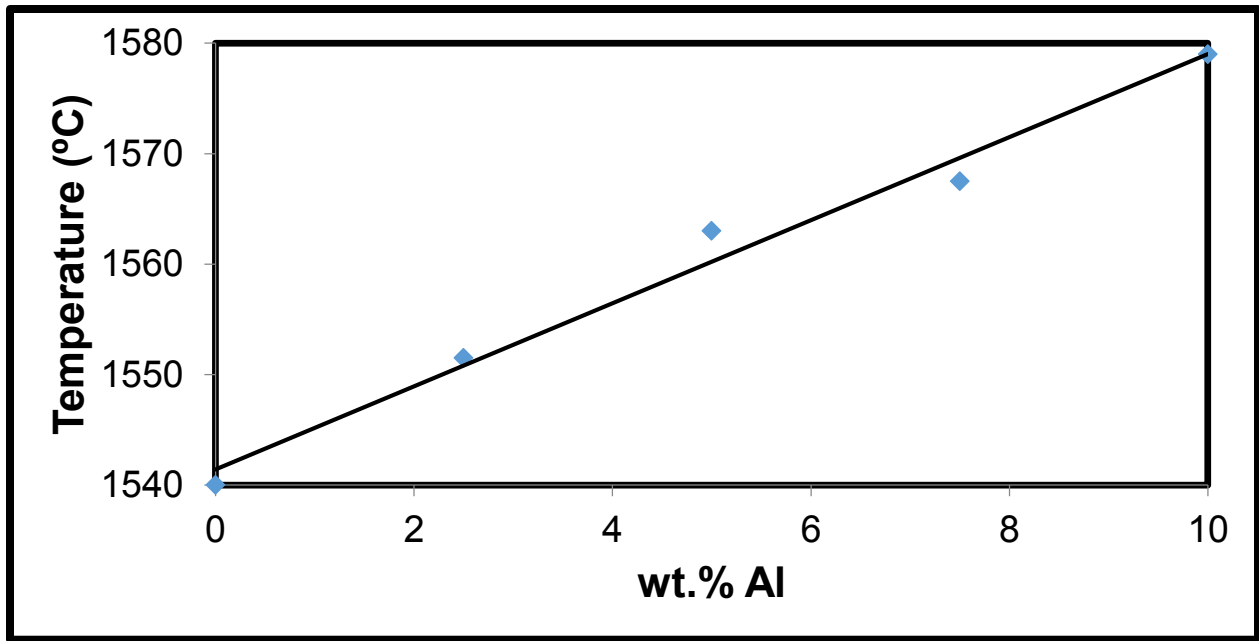


Figure 7.9: Effect of aluminum addition on the liquidus temperature of niobium-iron-aluminum ternary alloys.

In order to understand the effect of aluminum additions on the liquidus temperature, the isothermal niobium-iron-aluminum ternary phase diagram is considered at the compositions shown in Figure 7.10. It should be noted that all the compositions in the phase diagram are in atomic percent. The arrow indicates the addition of aluminum to the binary niobium-iron system under study. The yellow, blue and green circles represent 5 wt.%, 10 wt.% and 15 wt.% aluminum ternary alloys, respectively.

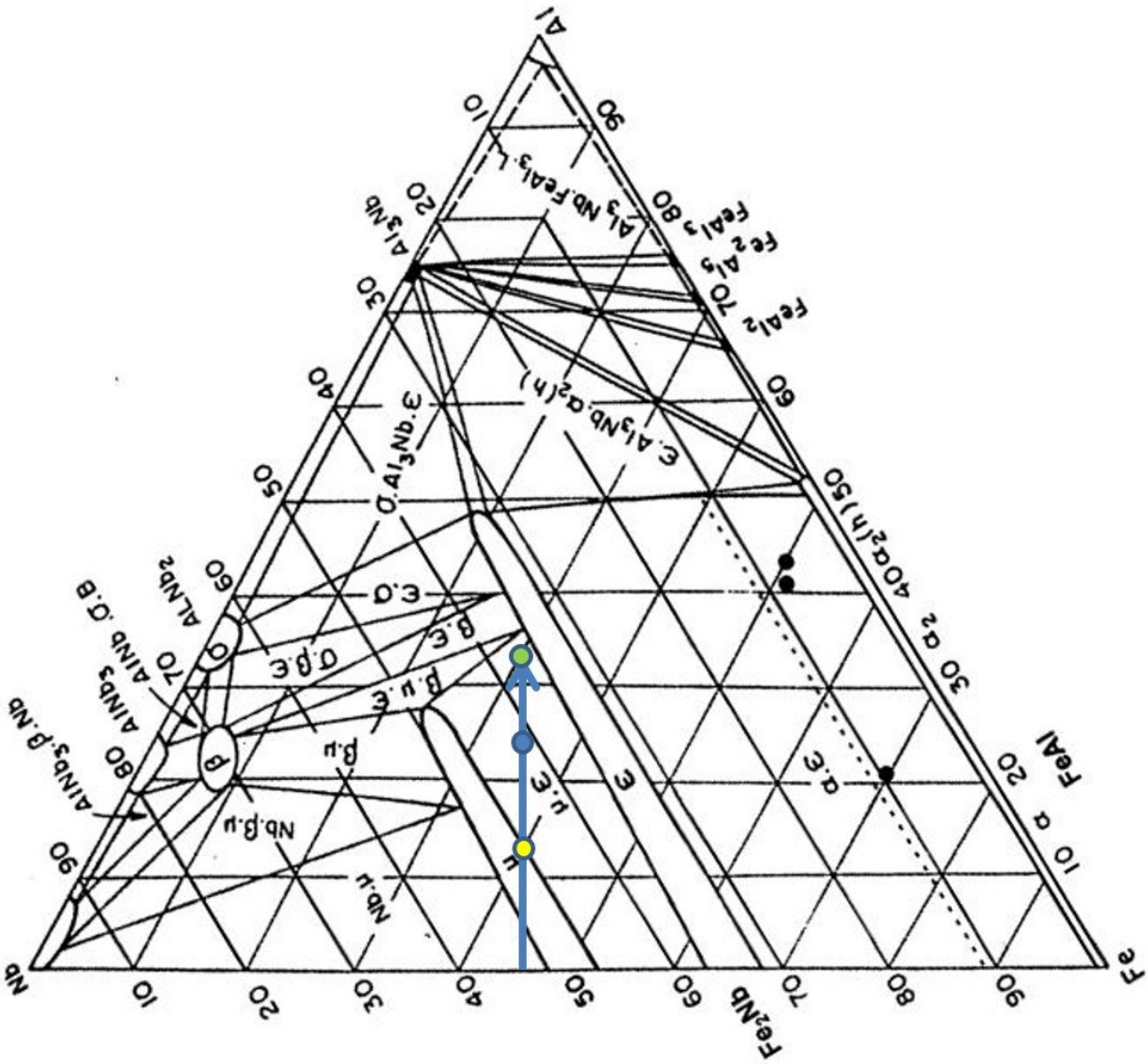


Figure 7.10: Isothermal section of the niobium-iron-aluminum phase diagram at 1273 K (1000°C) [Bej93(2)].

According to the phase diagram, the binary niobium-iron alloy, at equilibrium, consists of the niobium-rich solid solution phase and the  $\mu$ -phase ( $\text{Fe}_7\text{Nb}_6$ ), with  $\text{Fe}_7\text{Nb}_6$  being the majority phase. As the amount of aluminum is increased, the system moves into the single  $\mu$ -phase region. Between a composition range of 4 to 13 at.% aluminum, there is only one phase - the mu phase.

However, the experimental 5 wt.% aluminum ternary alloy (47 at.% niobium, 40 at.% iron and 13 at.% aluminum) has two phases, *i.e.*, the niobium-rich solid solution phase and  $(\text{Fe,Al})_7\text{Nb}_6$  ( $\mu$ -phase). The reason for the discrepancy could be that for the isothermal ternary phase diagram, equilibrium conditions were achieved by keeping the samples at elevated temperature for a significant period of time. However, for the arc melted samples in this work, no isothermal treatment was done. Instead samples were cooled from the liquid. Moreover, the isothermal diagram is at a temperature of 1273 K (1000°C), however the results under discussion are for the alloy at room temperature. The phase boundaries and even the number and type of phases will likely be different at room temperature compared with 1273 K (1000°C).

With further addition of aluminum, the system moves to a two phase region consisting of  $\text{Fe}_2\text{Nb}$  and  $\text{Fe}_7\text{Nb}_6$  intermetallics. Both intermetallics can dissolve significant amounts of aluminum. The 10 wt.% aluminum alloy (41.2 at.% niobium, 35 at.% iron and 23.8 at.% aluminum) is indicated by a blue circle on the arrow in Figure 7.10. According to the isothermal section this alloy should be free of the niobium-rich solid solution phase, which correlates with the experimental results in this work. However, there is an additional phase/region (region 1) for the samples in this work; region 1 could be the beta phase shown in the isothermal section. There is a triangular region in the phase diagram made up of three phases, *i.e.*,  $(\text{Fe,Al})_2\text{Nb}$  ( $\epsilon$ ),  $(\text{Fe,Al})_7\text{Nb}_6$  ( $\mu$ ) and beta ( $\beta$ ). The alloy compositions in this study are not positioned in the three phase region of the phase diagram. However, the phase diagram is an isothermal section at 1273 K (1000°C) and the phase boundary positions likely vary with temperature, so it is possible that the three phase triangle ( $\epsilon + \mu + \beta$ ) could be expanded at room temperature to include the alloy composition from this work. The composition of region 1 is 79-82 wt.% niobium, 12-15 wt.% iron and 6-7 wt.% aluminum. According to isothermal section, the beta phase could have an approximate composition of 9 at.%

iron, 71 at.% niobium and 20 at.% aluminum (86.4 wt.% niobium, 6.6 wt.% iron and 7 wt.% aluminum), which is close to the composition of region 1. Therefore, region 1 may be the beta phase; however, this could not be confirmed as no diffraction data is available in the literature.

As discussed earlier in this chapter, the arc melted ternary alloy with 10 wt.% aluminum had three different contrast regions (Figures 7.7a and 7.7c). Region 1 may be the beta phase or could be a metastable intermetallic ternary compound. Region 3 contained 66-67 wt.% niobium, 25-27 wt.% iron and 7-8 wt.% aluminum. Region 4 contained 54-55 wt.% niobium, 33-35 wt.% iron and 10-11 wt.% aluminum. Region 3 appears to be the  $\mu$ -phase ( $\text{Fe}_7\text{Nb}_6$ ), where aluminum atoms have replaced some of the iron atoms, and region 4 is likely the  $\varepsilon$ -phase ( $(\text{Fe,Al})_2\text{Nb}$ ).

Several authors have studied the iron-niobium binary system [Bej93(1), Bej93(2), Oka93, Pau86, Sri94, Vob11] and several versions are available (see Chapter 5). Two different phase diagrams for the iron-niobium system were shown in Figures 5.5 and 5.6. Figure 5.6 was used to explain the transformations peaks in the ferroniobium DSC study. This phase diagram (Figure 5.6) best represents the work presented here. The liquidus temperature for the arc melted 0 wt.% aluminum ternary alloy (binary iron-niobium system) calculated by DSC (1813 K (1540°C)) matches with the liquidus temperature of the iron-niobium system shown in the Figure 5.6 (1811 K (1538°C)). Note that the modified binary phase diagram shown in Figure 5.8 (Chapter 5), with a liquidus temperature of 1836 K (1563°C), does not correspond to the results in this chapter, as Figure 5.8 accounts for impurities in the ferroniobium alloy. According to the phase diagram shown in Figure 5.6, there is an increase in the liquidus temperature as the system changes from a mixture of the niobium-rich solid solution and  $\mu$  ( $\text{Fe}_7\text{Nb}_6$ ) to a mixture of  $\text{Fe}_2\text{Nb}$  ( $\varepsilon$ ) and  $\mu$  ( $\text{Fe}_7\text{Nb}_6$ ). The results in this work are consistent with the above. The ternary system, *i.e.*, arc melted alloys of iron,

aluminum and niobium, also experiences an increase in the liquidus temperature with increasing aluminum.

#### 7.4. Conclusions

- 1) Ferroniobium alloys with at least 10 wt.% aluminum added do not contain the niobium-rich solid solution phase.
- 2) Two main phases are present in arc melted ternary niobium-iron-aluminum alloys (10 wt.% aluminum). These are  $\text{Fe}_7\text{Nb}_6$  ( $\mu$ ) and  $\text{Fe}_2\text{Nb}$  ( $\epsilon$ ) intermetallic compounds with significant amounts of aluminum replacing some of the iron atoms. The third phase has higher niobium amounts (82-83 wt.%). Electron diffraction analysis indicates that it is not the niobium-rich solid solution phase.
- 3) There are four phases present in the induction melted ferroniobium alloys with 10 wt.% aluminum added. Two phases are same as those found in the arc melted alloys with the same overall composition. These are  $\text{Fe}_2\text{Nb}$  ( $\mu$ ) and  $\text{Fe}_7\text{Nb}_6$  ( $\epsilon$ ) with aluminum dissolved and replacing some of the iron. The third phase is common to both the arc melted and induction melted samples (79-86 wt.% niobium). There is an additional phase in the induction melted samples, which contains 72-74 wt.% niobium. It appears to be a metastable intermetallic ternary compound.
- 4) There are slight differences in the induction melted and arc melted samples due to significant differences in their cooling rates and the presence of impurities in the induction melted alloys (from the as-received ferroniobium alloy).

5) The DSC study indicates an increase in the liquidus temperature as the amount of aluminum is increased in arc melted ternary alloys. Therefore, the ternary alloys will have a higher liquidus temperature compared with the as-received ferroniobium alloy. However, the difference is 39 K (at 10 wt.% aluminum), which is below the steelmaking temperature.

## 7.5. References

- Abr06(1): S. Abraham, R. Klein, R. Bodnar and O. Dremailova. Formation of coarse particles in steel as related to ferroalloy dissolution thermodynamics. Part 1: ferroalloy melting, dissolution and microstructures. Material Science and Technology (MS & T), Cincinnati, Ohio, October 2006.
- Abr06(2): S. Abraham, R. Klein, R. Bodnar and O. Dremailova. Formation of coarse particles in steel as related to ferroalloy dissolution thermodynamics. Part II: crystallographic study of ferroalloys and coarse particles. Material Science and Technology (MS & T), Cincinnati, Ohio, October 2006.
- Bej93(1): J. M. Z. Bejarano, S. Gama, C. A. Ribeiro and G. Effenberg. The iron-niobium phase diagram. Zeitschrift für Metallkunde, 1993, 84, 3, 160–164.
- Bej93(2): J. M. Z. Bejarano. Investigation of the ternary diagram iron-aluminum-niobium. Ph.D. thesis, Department of Materials Engineering, Universidade Estadual de Campinas, Brazil, 1993.
- Eng92: T. A. Engh. Principles of Metal Refining. Oxford University Press, New York, US, 1992.
- Gla97: T. Gladman. The Physical Metallurgy of Microalloyed Steels. The University Press Cambridge, UK, 1997.
- Har71: E. M. Harold (ed.). The Making, Shaping and Treating of Steel. United States Steel, 1971.
- Oka93: H. Okamoto. Fe-Nb (Iron-Niobium). Journal of Phase Equilibria, 1993, 14, 5, 650–652.
- Pau86: E. Paul and L. J. Swartzendruber. The Fe-Nb (iron-niobium) system. Bulletin of Alloy Phase Diagrams, 1986, 7, 3, 248–254.
- Sha13(1): S. J. Shah, H. Henein and D. G. Ivey. Microstructural characterization of ferrotitanium and ferroniobium. Materials Characterization, 2013, 78, 96-107.

Sha13(2): S. J. A. Shah, H. Henein and D. G. Ivey. Microstructural evolution and characterization of a ferroniobium alloy. *Emerging Materials Research*, 2013, 2, EMR2, 79-89.

Sri94: S. Srikanth and A. Petric. A thermodynamic evaluation of the Fe-Nb system, *Zeitschrift für Metallkunde* 1994, 85, 3, 164–170.

Vob11: S. Vob, M. Palm, F. Stein and D. Raabe. Phase equilibria in the Fe-Nb system. *Journal of Phase Equilibria and Diffusion*, 2011, 32, 97–104.

## Chapter 8: Overall Conclusions and Future Recommendations

### 8.1. Conclusions

- Commercial grade ferrotitanium has nearly 10 wt.% impurities and five different phases, namely  $\beta$ -titanium solid solution (40-45%), a titanium-iron-aluminum ternary phase (40-45%),  $\alpha$ -titanium solid solution ( $\sim 10\%$ ), titanium carbonitride ( $\text{Ti}(\text{C}_x\text{N}_{1-x})$  - 1-2%) and FeTi (trace amounts). The titanium-rich solid solution (melting temperature is 1833 K (1560°C) to 1923 K (1650°C)) and titanium carbonitride (melting temperature is  $\sim 3273$  K ( $\sim 3000^\circ\text{C}$ )) have melting temperatures higher than the steelmaking temperature.
- Commercial grade ferroniobium studied in this work has nearly 3 wt.% impurities and has two phases, namely the  $\mu$  phase ( $\text{Fe}_7\text{Nb}_6$ ) ( $\sim 90\%$ ) and the niobium solid solution phase ( $\sim 10\%$ ). The melting temperature of niobium-rich solid solution phase ( $\sim 2673$  K (2400°C)) is significantly higher than the steelmaking temperature.
- The study of phase evolution mechanism in the commercial grade ferroniobium alloy shows that the  $\mu$  phase ( $\text{Fe}_7\text{Nb}_6$ ) is formed as a result of proeutectic, eutectic and eutectoid reactions. The Scheil solidification model predicts that as-received ferroniobium is formed at a cooling rate of  $\sim 10$  K/min with a eutectic depression of 20 K.
- Niobium (in form of ferroniobium) added to niobium free steel (steel A) did not produce any undissolved niobium-rich solid solution phase. The coarse niobium-rich particles in these steels were identified as NbC with small amounts of titanium and iron. A niobium containing steel (steel B) had coarse niobium-rich particles which were identified as

niobium-titanium carbonitrides. The Scheil solidification model was used to justify their presence as a result of segregation.

- Ternary alloys, with  $\geq 10$  wt.% aluminum additions, fabricated through induction melting and arc melting did not have the niobium-rich solid solution phase. Masters alloys (made by arc melting) showed an increase of 39 K in the melting temperature for the 10 wt.% aluminum ternary alloy.

## 8.2. Future Recommendations

- Regardless of a slight increase in the liquidus temperature of the proposed ternary alloy made in this research, it is recommended for evaluation in commercial steelmaking practice. The reason being that it eliminates the possibility of introducing the niobium-rich solid solution phase (melting temperature  $\sim 2400^{\circ}\text{C}$ ) while the liquidus temperature of the new alloy is lower than typical steelmaking temperatures. The new ternary alloy formed by melting as-received ferroniobium with 10 wt.% aluminum should be made in bulk quantities and added during steelmaking (trial runs) to observe any improvement in dissolution of ferroniobium. The amount of aluminum and or/ferroaluminum added to the steel should be adjusted in order to accommodate for the extra aluminum added in form of the new ternary alloy.
- The fact that niobium (in ferroniobium) is dissolving and segregating during solidification process urges us to modify the casting technique. The use of ultrasonic devices might be helpful in breaking the dendrites during solidification and avoiding segregation.
- Unlike ferroniobium, ferrotitanium has pre-existing coarse carbonitride particles in it. Characterization of steel samples with coarse titanium-rich particles should be carried out

in order to investigate the relationship (if any) between such particles and the carbonitrides in as-received ferrotitanium.

- Characterization of as-received ferrotitanium showed the presence of high melting temperature titanium carbonitrides. However, due to time restraints, further study to evaluate whether titanium carbonitride dissolves or remains undissolved during steelmaking was not done. Future work should include a study of titanium carbonitride dissolution, similar in approach to the work done on the niobium-rich solid solution phase in ferroniobium, including any possible remedies if dissolution is incomplete.

## **Bibliography**

Abr04: M. D. Abramoff, P. J. Magalhaes and S. J. Ram. Image processing with ImageJ. *Biophotonics International*, 2004, 11, 7, 36-42.

Abr06(1): S. Abraham, R. Klein, R. Bodnar and O. Dremailova. Formation of coarse particles in steel as related to ferroalloy dissolution thermodynamics. Part 1: ferroalloy melting, dissolution and microstructures. *Material Science and Technology (MS & T)*, Cincinnati, Ohio, October 2006.

Abr06(2): S. Abraham, R. Klein, R. Bodnar and O. Dremailova. Formation of coarse particles in steel as related to ferroalloy dissolution thermodynamics. Part II: crystallographic study of ferroalloys and coarse particles. *Material Science and Technology (MS & T)*, Cincinnati, Ohio, October 2006.

Arg82: S. A. Argyropoulos, R. I. L. Guthrie. Dissolution kinetics of ferroalloys in steel making. 65<sup>th</sup> steel making conference proceedings: Pittsburgh, March 28-31, 1982.

Arg84: S. A. Argyropoulos. The effect of microexothermicity and macroexothermicity on the dissolution of ferroalloys in liquid steel. *Electric Furnace Conference Proceedings, the Iron and Steel Society/AIME*, 1984.

Bej91: J. M. Z. Bejarano, S. Gama, C. A. Ribeiro, G. Effenberg and C. Santos. On the existence of the Fe<sub>2</sub>Nb<sub>3</sub> phase in the Fe-Nb system *Zeitschrift für Metallkunde*, 1991, 82, 615–620.

Bej93(1): J. M. Z. Bejarano, S. Gama, C. A. Ribeiro and G. Effenberg. The iron-niobium phase diagram. *Zeitschrift für Metallkunde*, 1993, 84, 3, 160–164.

Bej93(2): J. M. Z. Bejarano. Investigation of the ternary diagram iron-aluminum-niobium. Ph.D. thesis, Department of Materials Engineering, Universidade Estadual de Campinas, Brazil, 1993.

Cal07: William D. Callister Jr. Materials Science and Engineering, An Introduction. John Wiley and Sons Inc., 2007.

Car00: P. A. Carvalho, H. S. D. Haarsma, B. J. Kool, P. M. Bronsveld, J. Th. De Hosson and M. De Hosson. HRTEM study of  $\text{Co}_7\text{W}_6$  and its typical defect structure, *Acta Materialia*. 2000, 48, 2703-2712.

Car01: P. A. Carvalho and JTh. De Hosson. Stacking faults in the  $\text{Co}_7\text{W}_6$  isomorph of the  $\mu$  phase. *Scripta Materialia*, 2001, 45, 333-340.

Che87: Z. Chen, M. H. Loretto and R. C. Cochrane. Nature of large precipitates in titanium containing HSLA Steels. *Materials Science and Technology*, 1987, 3, 836-844.

Cos92: G. J. R. Costa. Niobium ferroalloy and niobium additive for steels, cast irons and other metallic alloys. Patent WO/1992/022675.

Cra00: A. J. Craven, K. He, L. A. J. Garvie and T. N. Baker. Complex heterogeneous precipitation in titanium-niobium microalloyed Al-killed HSLA steels-II. Non-Titanium based precipitates. *Acta Materialia*, 2000, 48, 3869-3878.

Dav01: J. R. Davis (Editor). *Alloying: Understanding the Basics*. ASM International, 2001.

Deh68: R. T. Dehoff and F. N. Rhines. *Quantitative Microscopy*. McGraw-Hill Book Company, New York, 1968.

Del92: J. Delamare, D. Lemarchand and P. Vigier. Transmission electron microscopy study of the  $\mu$  phase in the Fe-Nd-Al system. *Journal of Magnetism and Magnetic Materials*, 1992, 104, 7, 1092-1093.

Den91: A. R. Denton and N. W. Ashcroft. Vegard's Law. *Physical Review A: Atomic, Molecular and Optical Physics*, 1991, 3, 6, 3161-3164.

Dum98: L. F. S. Dumitrescu, M. Hillert and N. Saunders. Comparison of Fe-Ti assessments. *Journal of Phase Equilibria*, 1998, 19, 5, 441-448.

Eng92: T. A. Engh. *Principles of Metal Refining*. Oxford University Press, 1992.

Fer10: E. B. Ferreira, M. L. Lima and E. D. Zanotto. DSC method for determining the liquidus temperature of glass-forming systems. *Journal of American Ceramic Society*, 2010, 93, 11, 3757-3763.

Gas13: Michael M. Gasik (Editor). *Handbook of Ferroalloys: Theory and Technology*. Oxford: Elsevier Science, 2013.

Gei73: G. H. Geiger and D. R. Poirer. *Transport Phenomena in Metallurgy*. Addison-Wesley, 1973.

Ger06: V. Y. Gertsman and O. Dremailova. Transmission electron microscopy identification of a new Ti-Al-Fe intermetallic compound. *Journal of Material Science*, 2006, 41, 14, 4490-4504.

Gla97: T. Gladman. *The Physical Metallurgy of Microalloyed Steels*. The Institute of Materials, London, 1997.

Gol57: H. J. Goldschmidt. New intermediate phases in the iron-niobium system. *Research*, 1957, 10, 289-291.

Gou84: L. Gourtsoyannis, R. I. L. Guthrie and G. A. Ratz. The dissolution of ferromolybdenum, ferroniobium and rare earth (Lanthanide) silicide in cast iron and steel melts. *Electric Furnace Conference Proceedings, the Iron and Steel Society/AIME*, 1984.

Har71: E. M. Harold (ed.) The Making, Shaping and Treating of Steel. United States Steel, 1971.

Hon12: B. Hong, W. Jiang, L. Duarte, C. Leinenbach, L. Li-bin, L. Hua-shan and J Zhan-peng. Thermodynamic re-assessment of Fe-Ti binary system. Transactions of Non-Ferrous Metals Society of China, 2012, 22, 2204-2211.

Ich89: E. Ichise and K. Horikawa. Thermodynamic study of Fe-Ta and Fe-Nb alloys by means of the Knudsen Cell Mass Spectrometry. ISIJ International, 1989, 29, 10, 843-851.

Jon81: S. Jonsson. Assessment of the Fe-Ti System. Metallurgical and Materials Transactions B, 1981, 29B, 361-370.

Kri68: P. I. Kripyakevitch, E. I. Gladyshevskii and R. V. Skolozdra. Soviet Physics, Crystallography, 12 (1968) 525.

Kub55: O. Kubaschewski and W. A. Dench. The heats of formation in the systems titanium-aluminum and titanium-iron. Acta Metallurgica, 1955, 3, 339-346.

Kub82: O. Kubaschewski. Iron Binary Phase Diagrams. Springer-Verlag, Berlin, 1982.

Kum98: K. C. H. Kumar, I. Ansara and P. Wollants. Sublattice modelling of the  $\mu$  phase. Calphad, 1998, 22, 3, 323-334.

Loz07: E. Yu. Lozovaya, V. I. Zhuchkov and O. Yu. Sheshukov. Determination of melting time of an Fe-Al ferroalloy in an Iron-Carbon Melt. Russian Metallurgy (Metally), 2007, 7, 601-602.

Lu84: F. X. Lu and K. H. Jack. The occurrence of high speed steel carbide type  $\eta$  phases in the Fe-Nb system. Journal of Less Common Metals, 1985, 14, 123-127.

Man07: H. Mandar, T. Uustare, J. Aarik, A. Tarre and A. Rosental. Characterization of asymmetric rhombohedral twins in epitaxial – Cr<sub>2</sub>O<sub>3</sub>, thin films by X-ray and electron diffraction. *Thin Solid Films*, 2007, 515, 11, 4570-4579.

Mck82: M. J. Mckelvy, A. R. R. Smith and L. Eyring. High resolution electron microscope analysis of {100} twinning in  $\beta$  – rhombohedral boron. *Journal of Solid State Chemistry*, 1982, 44, 3, 374-381.

Men99: R. Mendoza, J. Huante, M. Alanis, C. Gonzalez-Rivera and J. A. Juarez-Islas. Slab cracking after continuous casting of API 5L X-70 grade steel for pipeline sour gas application. *Iron and Steelmaking*, 1999, 26, 3, 205-209.

Mor06: D. G. Morris, M. A. Munoz-Morris, L. M. Requejo and C. Baudin. Strengthening at high temperatures by precipitates in Fe-Nb-Al alloys. *Intermetallics*, 2006, 14, 1204-1207.

Mot99: M. A. Mota, A. A. Coelho, J. M. Z. Bejarano, S. Gama and R. Caram. Directional growth and characterization of Fe-Al-Nb eutectic alloys. *Journal of Crystal Growth*, 1999, 198/199, 850-855.

Mur81: J. L. Murray. The Fe-Ti (Iron-Titanium) system. *Bulletin of Alloy Phase Diagrams*, 1981, 2, 3, 320-334.

Mur87: J. L. Murray (Editor). *Phase Diagrams of Binary Titanium Alloys*. ASM International, Metals Park, OH, 1987.

Ohn00 I. Ohnuma, Y. Fujita, H. Mitsui, K. Ishikawa, R. Kainuma and K. Ishida. Phase equilibria in the Ti-Al binary system. *Acta Materialia*, 2000, 48, 3113-3123.

Oka93: H. Okamoto. Fe-Nb (Iron-Niobium). *Journal of Phase Equilibria*, 1993, 14, 5, 650-652.

- Oka95: H. Okamoto. Comment on Fe-Nb (Iron-Niobium). *Journal of Phase Equilibria*, 1995, 16, 4, 369-370.
- Oka96: H. Okamoto. Fe-Ti (iron-titanium). *Journal of Phase Equilibria*, 1996, 17, 4, 369.
- Oka02: H. Okamoto. Fe-Nb (Iron-Niobium) supplementary literature review. *Journal of Phase Equilibria*, 2002, 23, 1, 112.
- Pal09: M. Palm. Phase equilibria in the Fe corner of the Fe-Al-Nb system between 800 to 1150°C. *Journal of Alloys and Compounds*, 2009, 475, 173-177.
- Pan10: M. M. Pande, M. Guo, X. Guo, D. Geysen, S. Devisscher, B. Blanpain et al. Impurities in commercial ferroalloys and its influence on steel cleanliness. In the proceedings of the Twelfth International Ferroalloys Congress Sustainable Future. Helsinki, Finland, 2010.
- Pau86: E. Paul and L. J. Swartzendruber. The Fe-Nb (Iron-Niobium) System. *Bulletin of Alloy Phase Diagrams*, 1986, 7, 3, 248-254.
- Por92: D. A. Porter and K. E. Easterling. *Phase Transformations in Metals and Alloys*. Chapman and Hall, London, 1992.
- Pot01: R. M. Poths, R. L. Higginson and E. J. Palmiere. Complex precipitation behaviour in a microalloyed plate steel. *Scripta Materialia*, 2001, 44, 147-151.
- Pou85: J. L. Pouchou and F. Pichoir. "PAP" ( $\Phi$ - $\rho$ -Z) procedure for improved quantitative microanalysis. In: Armstrong JT, Editor. *Microbeam Analysis*. California: San Francisco Press, 1985.
- Rag87: V. Raghavan. The Al-Fe-Nb (Aluminum-Iron-Niobium) system, phase diagrams of ternary iron alloys. Part 1, ASM International, Materials Park, OH, 1987.

Ram66(1): A. Raman. The  $\mu$  phase. Zeitschrift für Metallkunde, 1966, 57, 301-305.

Ram66(2): A. Raman. X-ray investigations of some T-T<sup>5</sup>-Al systems. Zeitschrift für Metallkunde. 1966, 57, 7, 535-540 (In German)

Ram67: A. Raman. Structural study of niobium-iron alloys. Proceedings of the Indian Academy of Sciences-Section A, 1967, 65, 4, 256-264.

Rap94: M. T. Raposo, J. D. Ardisson, A. I. S. Pesiano and R. A. Mansur. Characterization of phases in the Fe-Nb system. Hyperfine Interactions, 1994, 83, 235-238.

Rob84: W. Roberts. Recent innovations in alloy design and processing of microalloyed steels. Conference Proceedings of International Conference on Technology and Applications of HSLA Steels, Philadelphia, 3-6 October, 1983, American Society of Metals 1984.

Ros52: W. Rostoker. Observation on the occurrence of Ti<sub>2</sub>X phases. Journal of Metals, 1952, 2, 209-210.

Sch96: C. G. Schon and J. A. S. Tenorio. The chemistry of iron-niobium intermetallics. Intermetallics, 1996, 4, 211-216.

Sha13(1): S. J. Shah, H. Henein and D. G. Ivey. Microstructural characterization of ferrotitanium and ferroniobium. Materials Characterization, 2013, 78, 96-107.

Sha13(2): S. J. A. Shah, H. Henein and D. G. Ivey. Microstructural evolution and characterization of a ferroniobium alloy. Emerging Materials Research, 2013, 2, EMR2, 79-89.

Sou01: C. A. de F. Sousa. The evolution of FeNb manufacturing. In Niobium, Science and Technology; Minerals, Metals and Materials Society: Orlando, FL, United states, 2001.

Sri94: S. Srikanth and A. Petric. A thermodynamic evaluation of the Fe-Nb system. *Zeitschrift für Metallkunde*, 1994, 85, 3, 164–170.

Ste79: L. Stenberg and S. Andersson. Electron microscope studies on a quenched Fe-Mo alloy, *Journal of Solid State Chemistry*, 1979, 28, 269-277.

Thy52: R. J. Van Thyne, H. D. Kessler and M. Hansen. The systems titanium-chromium and titanium-iron. *Transactions of the ASM*, 1952, 44, 974-989.

Tia07: Q. Tian, Y. Chen, J. Chen, G. Xu and Y. Zheng. Characterization of Nb-rich phase precipitation near internal cracks in continuously cast slabs. *Minerals, Metals and Materials Society (TMS)*, Warrendale, PA, 15086-7528, USA: 2007.

Vel07: N. Vellios and P. Tsakirooulos. The role of Fe and Ti additions in the microstructure of Nb-18Si-5Sn silicide-based alloys. *Intermetallics*, 2007, 15, 1529-1537.

Vob11: S. Vob, M. Palm, F. Stein and D. Raabe. Phase equilibria in the Fe-Nb system. *Journal of Phase Equilibria and Diffusion*, 2011, 32, 97–104.

Wan91: H. Wang, R. Lueck and B. Predel. Calorimetric determination of the enthalpy of mixing of liquid iron-titanium alloys. *Zeitschrift für Metallkunde*, 1991, 82, 8, 659–665.

Wet69: K. Wetzig. Investigations of intermetallic compounds in the binary systems Nb-Fe and Ta-Co by means of an emission electron microscope. *Physica Status Solidi (b)*, 1969, 34, 2, K79-K81.

Wil96: D. B. Williams and C. B. Carter, *Transmission Electron Microscopy: A Textbook for Materials Science*, Plenum Press, 1996.

Yua09: S. Q. Yuan and G. L. Liang. Dissolving behaviour of second phase particles in Nb-Ti microalloyed steel. *Materials Letters*, 2009, 63, 2324-2326.

Zho96: C. Zhou and R. Priestner. The evolution of precipitates in Nb-Ti microalloyed steels during solidification and post-solidification cooling. *ISIJ International*, 1996, 36, 11, 1397-1405.

Zhu90: J. Zhu and H. Q. Ye. On the microstructure and its diffraction anomaly of the  $\mu$  phase in superalloys, *Scripta Metallurgica et Materialia*, 1990, 24, 1861-1866.

Zhu07: X. Zhuo, X. Wang, W. Wang and H. G. Lee. Nature of large (Ti, Nb)(C, N) particles precipitated during the solidification of Ti, Nb HSLA steel. *Journal of University of Science and Technology Beijing: Mineral Metallurgy Materials (Eng Ed)*, 2007, 14, 2, 112-117.

Zhu08: X. Zhuo, D. Woo, X. Wang and H. Lee. Formation and thermal stability of large precipitates and oxides in titanium and niobium microalloyed steel. *Journal of Iron and Steel Research International*, 2008, 15, 3, 70-77.